Nanoscale Phonon Transport across Semiconductor Interfaces

Tommaso Albrigi

ICMAB
INSTITUT DE CIÈNCIA DE MATERIALS DE BARCELONA
EXCELENCIA SEVERO OCHOA
CSIC
CONSEJO SUPERIOR DE INVESTIGACIONES CIENTÍFICAS

UAB
Universitat Autònoma
de Barcelona

Nanoscale Phonon Transport across Semiconductor Interfaces

Candidate:
Tommaso Albrigi
.
Supervisor: Riccardo Rurali
Tutor: Javier Rodríguez Viejo

PhD programme in Physics
.
Academic Year 2024/2025
.
Barcelona

Foreword

In an era where electronic devices are not only shrinking in size but also evolving in complexity, the efficient management of heat has emerged as a pivotal challenge. This thesis was born from an enduring fascination with the nanoscale—a domain where quantum mechanics and classical physics converge to reveal behaviors that defy conventional wisdom. It is within the intricate scenario of semiconductor interfaces that the true nature of thermal transport is unveiled, and where the phonon—the quantum of lattice vibration—plays a decisive role in dictating device performance and longevity.

The motivation behind this work is both scientific and practical. As technology marches forward, the relentless drive for faster, more efficient, and more compact devices necessitates a deep understanding of heat flow at the atomic level. Traditional models of thermal conduction, such as Fourier's law, begin to falter when applied to nanoscale structures where atomic imperfections, interfacial phenomena, and quantum effects become dominant. This research endeavors to bridge that gap by probing the underlying mechanisms of phonon transport and thermal boundary resistance in semiconductor heterojunctions. Throughout my academic journey, I have been inspired by the work of pioneers in both experimental and theoretical physics, whose groundbreaking contributions have laid the foundation for modern thermal management strategies. My investigations are an attempt to extend this legacy by applying state-of-the-art simulation techniques—ranging from nonequilibrium molecular dynamics to first-principles calculations—to unravel the complex interplay between structure, temperature, and heat conduction. The challenges encountered in modeling such systems are often considerable, yet they offer a rewarding glimpse into the future of materials science, where every atomic interaction can have profound technological implications.

This thesis is also a personal journey of growth and discovery. I have been fortunate to work alongside mentors and colleagues who have not only shared their knowledge but have also inspired a passion for inquiry and innovation. Their unwavering support and critical insights have been invaluable in navigating the multifaceted challenges that arise when one ventures into new scientific domains. Beyond the technical achievements, this work is a testament to the collaborative spirit of modern research. It reflects the collective effort of a vibrant scientific community striving to push the boundaries of what is known about nanoscale phenomena. By exploring the delicate balance between coherent and diffusive phonon transport, and by examining the roles of interface morphology and temperature-dependent effects, this thesis aims to provide a comprehensive framework for designing semiconductor interfaces that can revolutionize thermal management in electronic devices. Looking ahead, the insights gained from this research offer exciting prospects for future innovations. As we further refine simulation techniques and integrate emerging methodologies such as machine learning, the potential to predict and tailor thermal properties at the atomic scale will only grow. It is my hope that the perspectives and methodologies presented herein will inspire not only academic inquiry but also practical applications that contribute to the evolution of next-generation technologies. In the grand tapestry of scientific progress, this thesis represents a modest yet hopefully meaningful step toward mastering the art of heat management in the age of nanotechnology.

Contents

Chapter 1

Introduction

Semiconductor technology constitutes the cornerstone of past and present-day electronics, and is likely to remain crucial for many decades to come, as leading semiconductor manufacturing companies are investing heavily in trials aimed at achieving optimal control of the elementary degrees of freedom in condensed matter systems. In the ever-evolving landscape of modern electronics, the significance of thermal transport across semiconductor interfaces is paramount. As electronic devices continue to shrink in size and increase in complexity, efficient heat management becomes critical for ensuring optimal performance and longevity. Semiconductor interfaces play a pivotal role in this thermal dynamics, influencing the efficiency of heat dissipation and overall device reliability. Understanding and controlling thermal transport at these interfaces is essential for addressing challenges related to overheating, a prevalent issue in high-performance electronic systems. This aspect gains particular relevance in the context of emerging technologies and materials, where innovative semiconductor interfaces can unlock enhanced thermal conductivity, contributing to advancements in power electronics, thermal management strategies, and the development of novel materials with unprecedented properties.

Electric charge and heat flow represent the two physical quantities to manipulate, and since the advent of classical electrodynamics and continuum mechanics, they have been successfully described by partial differential equations involving few degrees of freedom and effective mean field theories. However, thanks to the continuous improvements in the fabrication of smaller and smaller devices, we are now approaching the scale at which continuous models fail completely. Therefore, it is essential to take discreteness into account, and at some deeper level of understanding, also the quantum nature of the particles involved, to achieve a working description of microscopic matter. This situation paves the way for using new means of investigating the materials already involved, and those more likely to be involved, in modern technological advancements. Notably, the opportunity offered by computer simulations, combined with the unprecedented computational power we are now provided with, makes atomistic modeling a mandatory tool for scientific research in this field, which has already proved to be a valuable ally, far exceeding the most optimistic expectations. In particular, the chief energy carriers inside semiconductor materials are the atomic lattice vibrations. Quantum Mechanics quantizes this vibration, and the quantum of vibration is the Phonon. Phonons can display both wave-like and particle-like behavior, making it possible to observe coherent and diffusive transport regimes, as well as the transition between the two. When defects, like impurities, or interfaces between different materials are present in the atomic lattice, phonons can experience reflection, refraction, and scattering, and these transport processes can be tuned by controlling the distribution of defects. Within this context, III-V (A) semiconductor materials have drawn the attention of the scientific community in recent times, as they emerged as viable candidates for novel, high-performance devices, improved thermal management and heat dissipation in power electronics, and new opportunities to access previously unattainable material classes, namely supermaterials.

Indeed, we have witnessed a remarkable enhancement in the quality of the nanostructures that can be assembled today. Atomically flat heterojunctions are now achievable, and their most intriguing extension, namely superlattice nanowires - that is, nearly one-dimensional ordered stacks of atomic-scale slabs of different materials - has acquired special importance due to the unique possibilities that they open, like engineering the Raman spectrum, observing phonon coherence, and tuning the thermal conductivity to a considerable extent. For this reason, the computational study of transport processes within these materials, their constituent elements, and their electro-optical properties, has become a well-established trend within the scientific community, as it provides insights for further research, reliable sets of data for the industry, and support for laboratory experiments. Lattice-matched materials, such as Gallium Arsenide (GaAs) and Germanium (Ge), provide an ideal platform for constructing single-interface semiconductor heterojunctions. Their close lattice match ensures minimal defects and favorable electronic and phonon properties at the interface. GaAs and Ge, specifically, exhibit compatibility in both crystal structure and thermal characteristics. This alignment makes GaAs/Ge heterojunctions a compelling focus for computational characterization, offering valuable insights into their fundamental behavior and potential applications in advanced electronic devices.

Chapter 2 commences with a broad exploration of thermal transport across semiconductor interfaces, emphasizing the core concept of Thermal Boundary Resistance, referencing the relevant scientific literature, and then focuses on the GaAs/Ge heterojunction, providing an in-depth study of this system, which also introduces Nonequilibrium Molecular Dynamics and the LAMMPS code used in conducting calculations. Chapter 3 starts by outlining the logical connection between single interface heterojunctions and multiple interface systems, namely superlattice nanowires, as single interfaces can be thought of as superlattices' building blocks, and stresses the significance of superlattice nanowires and their role in crafting materials with tailored thermal and electro-optical properties. Then, the chapter extensively explores the thermal transport properties of the Silicon/Germanium superlattice nanowire, which serves as a pivotal example, employing both Nonequilibrium Molecular Dynamics simulations and insights from Density Functional Theory simulations, specifically utilizing the almaBTE code. The last chapter briefly touches on thermal transport properties of the GaAs - Gallium Phosphide (GaP) superlattice via Nonequilibrium Molecular Dynamics first, and then shifts gears, providing an overview of Density Functional Theory and introducing the ABINIT code. The machinery of Density Functional Theory is then harnessed to scrutinize the electro-optical properties and Raman spectrum of the GaAs/GaP superlattice, extending to the Indium Arsenide twinning superlattice, where a stacking defect is induced through mirrored slabs. These chapters collectively contribute to an in-depth understanding of thermal transport across semiconductor interfaces and the nuanced physics governing their behavior, broadening the scope of our understanding by inferring trends in thermal transport behaviors across various semiconductor interfaces.

Chapter 2

Single-Interface Thermal Transport

Thermal transport refers to the movement of heat through materials, which is crucial for understanding various physical processes and engineering applications. It classically encompasses mechanisms such as heat conduction, convection, and radiation, but when we move down to the nanoscale, the intricacies of nature provide us with a rather richer scenario, where multiple transport regimes proliferate, offering great theoretical and experimental research opportunities, and paving the way for unprecedented technological advancements. Understanding thermal transport at such a scale is indeed essential for designing efficient heat management systems, optimizing energy conversion processes, and developing advanced materials with tailored thermal properties. In modern electronics, thermal management is of paramount importance due to the increasing power densities and miniaturization of devices. Efficient thermal transport is crucial for preventing overheating, which can degrade device performance, reduce lifespan, and even lead to catastrophic failures. Effective heat dissipation techniques, such as thermal interface materials, heat sinks, and cooling systems, are critical for ensuring the reliability and longevity of electronic devices. Over the years, extensive research has been conducted to understand and manipulate thermal transport phenomena [1].

This research has led to significant advancements in areas such as materials science, nanotechnology, and thermal engineering. Current efforts focus on developing novel materials with enhanced thermal conductivity, exploring advanced thermal management techniques, and elucidating fundamental mechanisms of heat transport at the nanoscale. The field continues to evolve rapidly, driven by the demand for efficient thermal management solutions in various industries, including electronics, energy, and aerospace.

2.1 Thermal Conductivity

The theoretical foundations of such an evolving field trace back to the late XVIII century, and the major achievement of that time has been the discovery of Fourier's Law [2]. Fourier's law is the fundamental principle governing heat conduction at large scales, stating that the rate of heat transfer through a material is directly proportional to the temperature drop and the cross-sectional area, and inversely proportional to the distance over which the temperature gradient occurs. Mathematically, it is expressed as:

$$\mathbf{Q} = -\kappa \nabla T \tag{2.1}$$

where $\mathbf{Q}$ is the heat flux, κ is the thermal conductivity, and ∇T is the temperature gradient inside the material. The equation itself essentially defines the thermal conductivity of a given physical system at large scales. Thermal conductivity is thus a material property that quantifies its ability to transport heat. It depends on various intrinsic factors such as the material's atomic structure, crystal lattice vibrations, and the presence of defects or impurities. Generally, materials with stronger interatomic bonds and higher atomic masses exhibit higher thermal conductivities. Altogether, it is influenced by external factors like temperature, pressure, strain, and so on. Delving in this broad range of intricate dependencies, inevitably yields to facing the discrete nature of microscopic matter and discovering multiple heat transport regimes as well.

2.1.1 The linear regime

Fourier's equation implies a linear temperature profile over regions of length l, when a constant heat flux is present inside a given material, provided that the thermal conductivity does not change much as temperature decreases along the direction of the heat flux; that is when:

$$l \times |\nabla T| \frac{d \ln \kappa}{dT} \ll 1 \tag{2.2}$$

In many practical applications, this condition makes the measurement of the thermal conductivity feasible, as the temperature gradient at any point coincides with the overall temperature drop divided by the total length, which can be directly observed.

2.2 Phonons and Phononics

Lattice vibrations and electrons are the primary energy carriers in solids. While electron transport represents the major contribution to thermal conductivity for metals, due to the movement of free electrons, lattice vibrations dominate heat transport in dielectric and semiconductor materials. Quantum Mechanics (QM) makes the energy spectrum of such vibrations discrete, and the quantum of excitation is called Phonon.

2.2.1 Quasiparticles

It is noteworthy to mention that, while addressing to electrons as particles is fully legitimate, strictly speaking phonons are quantized excitations that exhibit many particle-like properties, but can't be endowed with any wavefunction in its own right, can't be associated to any conserved probability current, and the total number of phonons is not conserved during time. For these reasons, phonons, as well as many other particle-like excitations, are more properly referred to as "quasiparticles", which is a key concept in condensed matter physics.

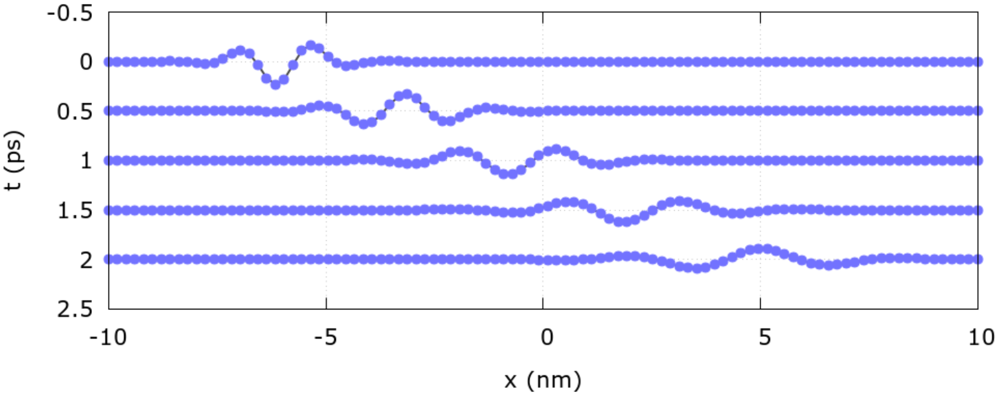

Figure 2.1: Schematic representation of a phonon travelling in a one-dimensional atomic chain. The different curves (top-down) correspond to the configuration of the whole chain over increasing times. For this localized perturbation of the lattice, particle-like properties as position, extension, and velocity are well-defined.

2.2.2 The Phononic Spectrum

Recent advancements in phononics have led to significant breakthroughs in the control of sound and heat through the development of innovative materials and devices [3]. Tailor-made multi-material crystals, with their periodic structures, create phononic bandgaps that block certain frequencies of mechanical waves, enabling applications in soundproofing, medical imaging, and thermal management. Acoustic diodes, which allow unidirectional sound transmission, are constructed using such crystals and nonlinear materials, providing solutions for ultrasound and noise control. Acoustic cloaking devices, again made from metamaterials, guide sound waves around objects, making them undetectable and offering potential in stealth and architectural acoustics. Optomechanical crystals, which simultaneously localize phonons and photons, enhance acousto-optical interactions, paving the way for advancements in quantum computing and telecommunications. Thermal diodes control heat flow directionally, leveraging materials with asymmetric thermal conductance to manage heat in electronic devices and buildings. Thermal metamaterials and cloaking techniques adapt principles from optical and acoustic metamaterials to manipulate heat conduction, creating thermal shields and concentrators. Nanostructured materials, such as quantum-

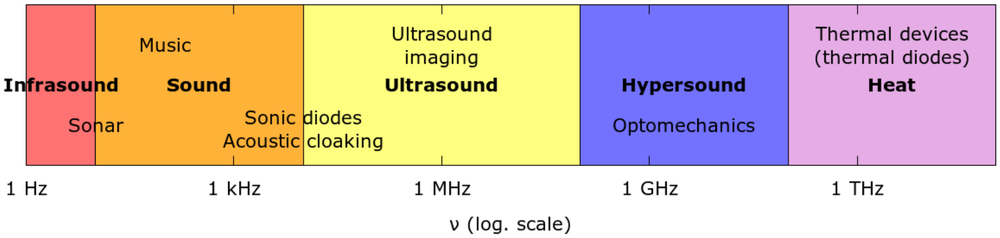

Figure 2.2: Technological interest and some applications across the phononic spectrum, spanning 12 orders of magnitude. The broad range of frequencies involved requires several different modeling techniques and experimental probes, specific to each research sector. This thesis covers just a tiny fraction of what is contained inside the blue and purple windows.

dot superlattices and semiconductor nanowires, have improved thermoelectric efficiency by reducing thermal conductivity through phonon scattering. Thermocrystals, periodic structures designed to control heat flow, concentrate thermal energy in specific frequency ranges, enabling coherent heat management similar to sound wave control. These innovations in phononics promise to revolutionize various fields, offering new solutions for thermal management, noise reduction, energy conversion, and even protection against seismic waves.

2.3 Coherent Phonon Transport

Parallel to this scenario, semiconductor materials constitute the bedrock of modern electronics, where interfaces—which can be considered foundational since the advent of electronics coincides with the development of the first working electric diode—are ubiquitous. These interfaces scatter phonons, thereby providing a twofold motivation for the investigation of phonon transport mechanisms across them. Firstly, understanding their working principles and the physics underlying them is essential for better characterizing the devices and physical systems in use. Secondly, it enables new means to engineer phonon transport and manipulate heat transfer, opening up novel possibilities and addressing the technological quest for an ever-efficient thermal management capability.

2.3.1 Mean Free Path and Thermal Wavelength

Two key quantities for phonons are the mean free path (MFP) and "thermal wavelength". The mean free path defines the average distance the phonons travel between two scattering events. When the size of the physical system, or that of its geometrical features, approach such a scale, the diffusive regime no longer holds, and deviations from Fourier's law become inevitable. In addition, QM provides such elementary energy carrier with a temperature-dependent, average wavelength too, in turn defining, for any given temperature, the scale at which its wave-like nature becomes non-negligible.

2.3.2 Bose-Einstein Statistics

A non-interacting phonon gas strictly obeys Bose-Einstein statistics. This is a direct consequence of QM. This statistics governs the phonon population of single-particle states in non-interacting theories. Unlike fermions, phonons are bosons, which means multiple phonons can occupy the same single-particle state, and the total number of phonons in a given single-particle state with energy ϵ is provided by the Bose-Einstein distribution function. The Bose-Einstein distribution for phonons is given by:

$$n(\epsilon) = \frac{1}{e^{\epsilon/k_B T} - 1} \tag{2.3}$$

where $n(\epsilon)$ is the average number of phonons occupying a specified single-particle state with energy ϵ, k_B is the Boltzmann constant, and T is the absolute temperature. This distribution plays a crucial role in determining the thermal properties of solids, such as specific heat and thermal conductivity. At high temperatures (compared to the Debye temperature), the heat capacity approaches the Dulong-Petit limit, whereas at low temperatures, it follows the T^3 Debye law due to the Bose-Einstein statistics.

Maxwell-Boltzmann limit

In the high-temperature limit the phonon occupation numbers grow considerably, and the Bose-Einstein statistics can be approximated by the Maxwell-Boltzmann statistics. This is best illustrated by taking into account the partition function of the quantum theory of the harmonic oscillator, characterized by the frequency ω, and show that under specific conditions it reduces to that of the classical theory. The partition function in the quantum case is given by:

$$Z_Q(T) = \frac{1}{2\sinh\left(\hbar\omega/2k_BT\right)} = \frac{1}{2\sinh\left(E_0/k_BT\right)} \tag{2.4}$$

where we labeled the ground state energy $\hbar\omega/2$ by E_0, while the classical partition function is:

$$Z_{cl}(T) = \frac{2\pi k_BT}{\omega} \tag{2.5}$$

Since the first quantity is dimensionless, we need to multiply it by $2\pi\hbar$ for comparing it with the classical case. An inspection at Equation 2.4, joint to the identity $\sinh(x) \approx x$, for $x \ll 1$, reveals that:

$$\lim_{\frac{E_0}{k_BT}\to 0} 2\pi\hbar\ Z_Q(T) = \lim_{T\to+\infty} 2\pi\hbar\ Z_Q(T) \approx \frac{2\pi k_BT}{\omega} \tag{2.6}$$

which is exactly the expression of the partition function in the classical limit. Interestingly enough, the classical limit of the partition function is conceptually independent from the high-temperature one, as the first one is obtained by multiplying Z_Q by $2\pi\hbar$ and taking the limit $\hbar \to 0$, whereas the second one is obtained still multiplying Z_Q by the same factor, but then we take the $T \to \infty$ limit instead. Nonetheless, these two limits coincide, elucidating how the classical world emerges from the quantum one when temperature induces a statistical averaging over a huge number of quantum states. In conclusion, we have proved that whenever the thermal energy k_BT is much greater than the ground-state energy, meaning that temperature is "high", phonons behave similarly to classical particles, where the probability of occupation of a state is much lower, and the statistics governing their behavior simplifies significantly. This approximation is particularly useful in calculations related to thermal properties at high temperatures.

2.3.3 Technological interest

Since the typical phonon MFP in semiconductor materials at room temperature falls in the 100 nanometer range, and the thermal wavelength is about two order of magnitude smaller, control over interference effects became available only in relatively recent times, thanks to the near-to-atomic level quality of the nanostructures that can now be assembled, and that were completely unachievable before [4]. This is particularly true for interfaces, as atomically flat interfaces have been obtained using molecular beam epitaxy and chemical vapor deposition techniques, and the almost perfect lack of defects scattering phonons resulted in great enhancement in the number of phonons successfully travelling across the interface, in contrast with the cases where surface roughness or chemical mixing were present. Moreover, the present experimental methods allow stacking multiple interfaces together in a highly ordered fashion, both in extended and quasi one-dimensional systems, giving rise to bulk superlattices–previously known as “phononic crystals”, and radial and axial superlattice nanowires, which led to the first experimental observation of coherent phonon transport in History [5]. For the reasons outlined above, the subject of this thesis is nanoscale phonon transport across semiconductor interfaces.

2.4 Thermal Boundary Resistance

When two materials with different temperatures come into contact, heat flows from the hotter material to the cooler one. This seemingly simple process is far more complex than it first appears. The concept of interfacial thermal resistance (ITR) or thermal boundary resistance (TBR), which characterizes the difficulty of heat transfer across the interface of two materials, has intrigued scientists since the 19th century.

2.4.1 Global overlook

The initial discussions can be traced back to Fourier in 1822, who introduced the idea of “external conducibility” to describe heat transfer across surfaces. This term laid the groundwork for what we now understand as interfacial thermal conductance (ITC). Following Fourier, Poisson in 1835 furthered the theory by formulating the continuity of heat flux at an interface [6]. However, significant advancements in understanding TBR came much later. Smoluchowski in 1898 conducted the first experimental and theoretical studies on heat transfer between solid and gas interfaces, which aligned with Maxwell's earlier theories [7]. A significant turning point came in the mid-20th century when Kapitza observed a temperature drop at the boundary between liquid helium and a solid, which he later theorized in 1941 [8]. This discovery, known as Kapitza resistance, spurred extensive research into TBR across various interfaces. In 1969, Pollack's review focused mainly on solid-liquid interfaces at cryogenic temperatures [9], while Swartz and Pohl in 1989 extended the discussion to solid-solid interfaces, highlighting the limitations of existing theories like the acoustic mismatch model (AMM) and the diffuse mismatch model (DMM) at temperatures above 30 K [10]. The study of TBR incorporates both theoretical models and experimental techniques to understand and measure the resistance.

2.4.2 Definition and Theoretical Models

Here, we brief the key theoretical models and experimental methods developed over the years, primarily referencing to the 2022's review from Chen et al [11]. Consider an experiment where two materials, A and B, are put into contact and the outer sides of the junction are kept at constant temperatures T_A and T_B by two thermostats, with $T_A > T_B$. If we let the system evolve, heat will start flowing inside the material from the hot thermostat to the cold one and, after sufficiently long time, the heat flux across it will stabilize at some constant value $\bar{Q}$, and the whole junction will reach a steady state. When such a state is reached, the temperature is well defined everywhere inside the system, and the temperature profile can thus be measured. Assuming Equation 2.2 holds, we can be schematically depict the resulting situation as in Figure 2.3. One might have assumed that heat would flow smoothly across the interface, but in reality, the resistance at the boundary can be substantial, and a remarkably sharp temperature drop, causing a discontinuity in the temperature profile, appears between materials A and B. The experiment reveals that even though both materials are in intimate contact, the interface acts as a bottleneck for heat transfer. This possibly unexpected outcome arises from the differing atomic structures and bonding strengths at the boundary, which create an effective thermal barrier.

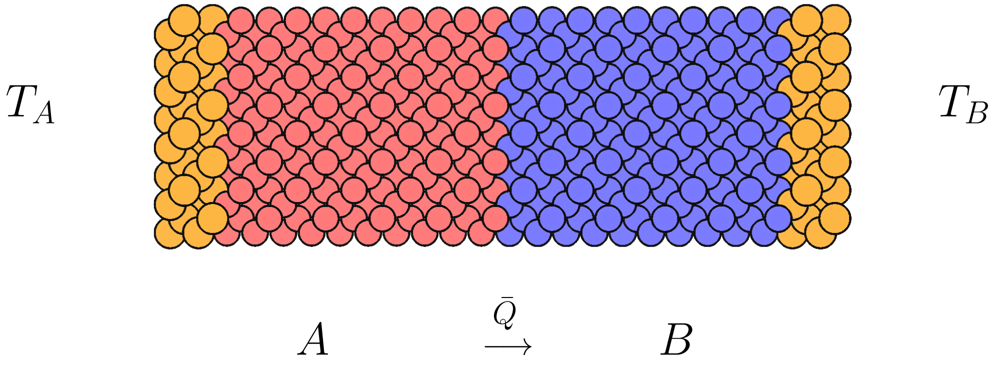

(a) thermal junction

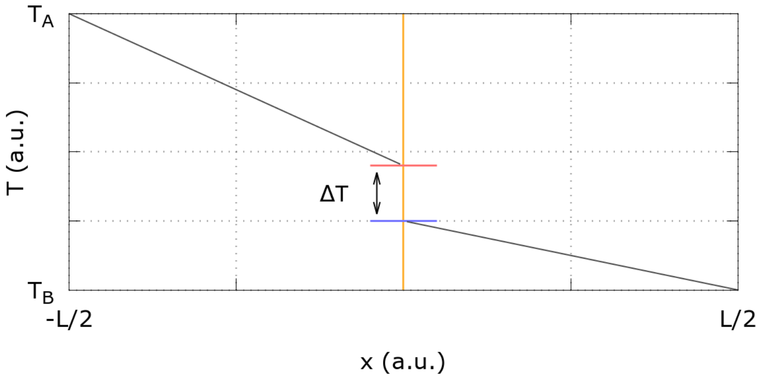

(b) temperature profile

Figure 2.3: (a) Thermal junction obtained from materials A, red and B, blue. The yellow atoms represent the thermostatted regions. The black arrow indicates the direction of the heat flux. (b) Ideal steady-state temperature profile inside the junction, with highlighted temperature drop and interface position.

The simplest way to quantify such an effect, in close analogy with Fourier's law, is to take the ratio between the total heat flux $\bar{Q}$ and the resulting temperature drop only, since no thermal gradient is defined at the interface. This relationship can be formulated as:

$$\bar{Q} = h_I \Delta T \quad \text{and} \quad R_I = \frac{1}{h_I} \tag{2.7}$$

where h_I is the ITC and R_I is the TBR. This resistance often turns out to be much higher than anticipated, especially for nanoscale systems, highlighting how microscopic interactions at the boundary can significantly impact the overall thermal conductance of a given device. It is typically expressed in units of $\mathrm{W/m^2K}$ and is thus derived from the fundamental relationship where the heat flux across an interface is proportional to the temperature drop at the interface and inversely proportional to the interfacial resistance.

Acoustic and Diffusive Mismatch Model

The simplest theoretical setup capable of predicting this effect is the AMM, proposed by Khalatnikov in 1952, which suggests that the heat transfer at an interface depends on the acoustic impedances of the materials [12]. In this model, both materials on either side of the interface are treated as continuous elastic media. The phonons are regarded as elastic waves that obey continuum acoustic principles. When such an elastic wave encounters an interface, it can either be totally or only partly reflected back into the original material, and transmitted into the second material accordingly. The angles of incidence and transmission are determined by Snell's law, given by:

$$\sin\theta_A / c_{A\varepsilon} = \sin\theta_B / c_{B\varepsilon}, \tag{2.8}$$

where θ_A and θ_B are the angles of incidence and transmission, respectively, and $c_{A\varepsilon}$ and $c_{B\varepsilon}$ are the sound velocities in the respective materials for a given polarization ε (usually longitudinal or transverse). The transmission coefficient for an elastic wave across a plane interface that is derived from continuum theory, is defined as the ratio between transmitted and incident energy flux, and is given by:

$$\zeta_{A\to B} = \frac{4 Z_A Z_B \cos\theta_A \cos\theta_B}{(Z_A \cos\theta_B + Z_B \cos\theta_A)^2}, \tag{2.9}$$

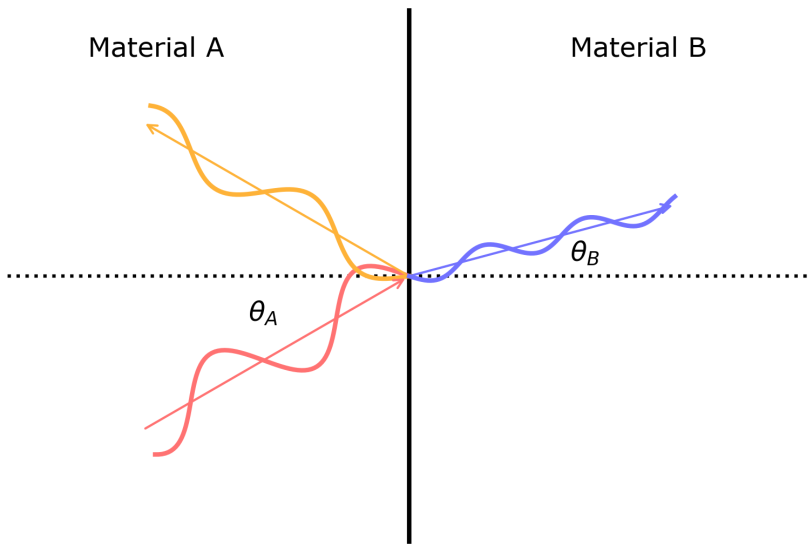

Figure 2.4: Schematics of an elastic wave experiencing reflection and refraction as it encounters the interface separating materials A and B along its path. The arrows represent the direction of propagation of the corresponding waves. The incident, reflected and transmitted wave are depicted in red, yellow and blue respectively. The dashed line represents the normal to the interface at the incidence point. θ_A and θ_B are the incidence and transmission angles.

where $Z = \rho c_\varepsilon$ is the acoustic impedance of the material and ρ being the material density. Two more fundamental concepts, largely independent from the specific model we are describing, are the phonon frequency and phonon wave-vector. The phonon frequency, often denoted as ω, represents the oscillation rate of the lattice vibrations. It is directly related to the energy of the phonon by the relationship $\epsilon = \hbar\omega$, where $\hbar$ is the reduced Planck constant. The frequency spectrum of phonons in a solid is determined by the material's atomic mass, bond strength, and crystal structure. The phonon wave-vector, represented as $\mathbf{k}$, is a vector quantity that describes the wave properties of phonons, including their wavelength and direction of propagation within the crystal lattice. The magnitude of the wave-vector is related to the wavelength λ by the equation $\|\mathbf{k}\| = \frac{2\pi}{\lambda}$. The phonon wave-vector lies within the first Brillouin zone, which is a uniquely defined primitive cell in reciprocal space. The relationship between the phonon frequency and wave-vector is described by the phonon dispersion relation, $\omega = \omega(\mathbf{k})$, which can be polarization-dependent, and provides critical insights into the vibrational properties of the material and influences the thermal conductivity. The dispersion relation allows predict how phonons of different frequencies and wave-vectors contribute to thermal transport.

Formulae

The total heat flux Q perpendicular to the interface is indeed expressed as:

$$\begin{aligned} Q = &\frac{1}{V}\sum_{\mathbf{k}\varepsilon}^{A} \hbar\omega_{\mathbf{k}\varepsilon} v(\mathbf{k},\varepsilon) n(\omega_{\mathbf{k}\varepsilon}, T_a)\zeta_{A\to B}(\mathbf{k},\varepsilon) \\ &+ \frac{1}{V}\sum_{\mathbf{k}'\varepsilon'}^{B} \hbar\omega_{\mathbf{k}'\varepsilon'} v(\mathbf{k}',\varepsilon') n(\omega_{\mathbf{k}'\varepsilon'}, T_b)\zeta_{B\to A}(\mathbf{k}',\varepsilon'), \end{aligned} \tag{2.10}$$

where V is the total volume, $\hbar$ is the reduced Planck constant, $\omega_{\mathbf{k}\varepsilon}$ is the phonon frequency, v is the phonon group velocity along the normal to the interface $\mathbf{n}$, defined by

$$v = \mathbf{n} \cdot \frac{\partial \omega_{\mathbf{k}\varepsilon}}{\partial \mathbf{k}} \tag{2.11}$$

with $\cdot$ denoting the dot product. n is the phonon distribution function, provided by the Bose-Einstein statistics, and ζ is the phonon transmission coefficient. The superscripts A and B in the summation correspond to the contribution of the two material. The temperatures T_a and T_b are on the left and right sides of the interface, respectively. When $T_a = T_b = T$, the net heat flux becomes zero, providing a relation between the two contributions, which then can be used to obtain:

$$Q = \frac{1}{V}\sum_{\mathbf{k}\varepsilon}^{A} \hbar\omega_{\mathbf{k}\varepsilon} v(\mathbf{k},\varepsilon)\zeta_{A\to B}(\mathbf{k},\varepsilon)[n(\omega_{\mathbf{k}\varepsilon},T_a) - n(\omega_{\mathbf{k}\varepsilon},T_b)] \tag{2.12}$$

The ITC, $h_I(T)$, can then be derived as:

$$h_I(T) = \frac{1}{V}\sum_{\mathbf{k}\varepsilon} \hbar\omega_{\mathbf{k}\varepsilon} v(\mathbf{k},\varepsilon)\zeta_{A\to B}(\mathbf{k},\varepsilon)\frac{\partial n(\omega_{\mathbf{k}\varepsilon},T)}{\partial T} \tag{2.13}$$

At this point it is possible to carry on the calculation by replacing the summation of the wave vector in Equation 2.13 with the integral of frequency in the Debye model, which assumes $\omega = ck$, and integrating over all incident angles:

$$h_I = \frac{1}{(2\pi)^2}\sum_{\varepsilon} I_{A\varepsilon}\int_0^{\omega_D} \frac{\hbar\omega^3}{c_{A\varepsilon}^2}\frac{\partial n(\omega_\varepsilon,T)}{\partial T}d\omega \tag{2.14}$$

where $I_{A\varepsilon}$ represents the integral of $\zeta_{A\to B}(\theta_A,\varepsilon)$ over all the incident angles. In the low-temperature limit, the integral in Eq. (10) can be solved analytically, and the TBR turns out to satisfy:

$$R_{\mathrm{AMM}} = \text{constant} \times T^{-3} \tag{2.15}$$

This T^{-3} dependence originates from Debye's T^3 law of heat capacity at low temperatures. However, the AMM is not applicable at high temperatures due to the absence of phonon scattering. The DMM addresses this by assuming that phonons are scattered diffusely at the interface, losing memory of their initial direction and energy state. This model provides a more accurate description at higher temperatures, where the AMM fails. The transmission coefficient in the DMM does not depend on the wave vector or the mode index and is given by:

$$\zeta_{A\to B}(\mathbf{k},\varepsilon) = \zeta_{A\to B}(\omega), \tag{2.16}$$

with the reverse transmission probability given by:

$$\zeta_{B\to A}(\omega) = 1 - \zeta_{A\to B}(\omega). \tag{2.17}$$

with

$$\zeta_{A\to B}(\omega) = \frac{\sum_{\varepsilon} c_{B\varepsilon}^{-2}}{\sum_{i\varepsilon} c_{i\varepsilon}^{-2}}. \tag{2.18}$$

At low temperatures, the TBR in the DMM is still satisfying a T^{-3} dependence like the AMM, but the numerical constant is different. Recent studies have also improved the DMM by incorporating exact phonon dispersion, optical phonon modes, joint vibrational states, thermal flux effects, and inelastic scattering to better match experimental data and provide a more comprehensive understanding of interfacial thermal transport.

2.4.3 Experimental and Computational Methods

Experimental methods have also advanced significantly. The pump-probe thermoreflectance technique is an ultrafast laser-based method that measures the change in reflectance due to temperature variations, allowing for precise determination of ITC [13]. The electron-beam self-heating method uses an electron beam to locally heat a sample, directly measuring the TBR by observing the temperature profile across an interface [14]. The 3ω method involves applying an AC current to a heater and measuring the third harmonic of the voltage to determine the material's thermal properties, including the TBR [15]. Understanding TBR in solid-solid interfaces is crucial for applications in electronics and thermal engineering. The research in this area has significantly evolved over the past three decades, focusing on both macroscopic and nanoscale interfaces. Lattice mismatch, or disparities in lattice structures between two materials, can impede phonon transport. Studies, such as those by Hopkins et al. on Si/Ge systems, show that lattice mismatch leads to multiple reflections and interference effects, which are not accounted for in simpler models like AMM [16]. The strength of bonding at the interface, known as interfacial coupling strength, affects the transmission of phonons, with stronger coupling typically leading to better thermal conductance. Surface roughness and atomic-scale disorders at the interface can scatter phonons too, further reducing the thermal conductance [17]. Advancements in theoretical models and experimental techniques have deepened our understanding of TBR.

Computational methods like molecular dynamics simulations, lattice dynamics, and the Green's function approach provide detailed insights into phonon interactions at the atomic level, making the choice of the particular approach depend on the specific system of interest, or the physical phenomena under investigation [18]. The study of interfacial thermal resistance has come a long way since the early theoretical propositions by Fourier and Poisson. With the advent of sophisticated experimental techniques and computational models, our understanding of TBR across various interfaces has significantly improved. The continuous development in this field is crucial for enhancing the thermal management of electronic devices and other applications where efficient heat dissipation is essential.

2.5 GaAs and Ge

Among the various semiconductor materials available in the industry of semiconductor technology, Gallium Arsenide (GaAs) and Germanium (Ge) are both vital. GaAs is known for its high electron mobility, making it suitable for high-frequency applications and optoelectronic devices, such as light-emitting diodes (LEDs) and solar cells. Ge, on the other hand, is notable for its application in high-efficiency solar cells and as a substrate for high-speed integrated circuits. These materials are lattice-matched, allowing for the formation of clean and defect-free GaAs/Ge heterojunctions. Additionally, the GaAs/Ge interface is essential in the synthesis of hexagonal Ge through the crystal structure transfer method, where hexagonal GaAs nanowires work as templates for the radial growth of hexagonal SiGe and Ge shells [19–23]. Given the importance of these interfaces, a comprehensive physical characterization focusing on transport processes is critical. In this chapter, we conduct an atomistic investigation using nonequilibrium molecular dynamics (NEMD) to study phonon transport across the GaAs/Ge interface. In particular, we evaluate how temperature and atomic-scale interface morphologies, including chemical intermixing and roughness, impact thermal conduction and explore their implications for thermal rectification [24]. To probe into these dependencies, we performed approximately 100 simulations, balancing a thorough exploration of parameter space with computational efficiency [25–27].

2.6 Molecular Dynamics

Molecular Dynamics (MD) is a computational technique used to simulate the movement of atoms and molecules over time. It's widely employed in various fields such as chemistry, physics, materials science, and biology to study the behavior of molecular systems at the atomic level. In MD simulations, the system is modeled as a collection of interacting particles, typically atoms or molecules. The behavior of each particle is governed by Newton's equations of motion:

$$m_i \frac{d^2\mathbf{r}_i}{dt^2} = \mathbf{F}_i \tag{2.19}$$

where m_i is the mass of particle i, $\mathbf{r}_i$ is its position vector, and $\mathbf{F}_i$ is the net force acting on it. To perform MD simulations, one needs a force field that describes the interactions between particles. A common form of the force field is the pairwise potential energy function:

$$U(\mathbf{r}_1, \mathbf{r}_2, ..., \mathbf{r}_N) = \frac{1}{2} \sum_{i \neq j}^{N} V(r_{ij}) \tag{2.20}$$

where $V(r_{ij})$ is the pairwise potential energy between particles i and j separated by a distance r_{ij}. The force acting on each particle is then derived from the potential energy function by taking the negative gradient of the potential energy with respect to the particle's position:

$$\mathbf{F}_i = -\nabla U(\mathbf{r}_1, \mathbf{r}_2, ..., \mathbf{r}_N) \tag{2.21}$$

However, in many cases, interaction potentials need to go beyond the pairwise level to accurately represent the system's behavior.

2.6.1 The Tersoff Potential

Three-body interaction potentials, such as those of Tersoff type, are particularly important in systems where covalent bonding or other forms of three-body interactions play a significant role [28]. The Tersoff potential is designed to model the energetics of covalent systems indeed. It is an empirical potential formulated to treat complex systems and perform extended simulations. The potential has been particularly effective for silicon and carbon, it has been extended to multicomponent systems, and includes terms that account for bond interactions and environmental dependencies. The general form for this interatomic potential involves terms that represent two-body and three-body interactions. It includes pairwise terms $f_R(r_{ij})$ and $f_A(r_{ij})$, which represent repulsive and attractive interactions, respectively. The energy $V(r_{ij})$, or simply V_{ij}, as a function of the atomic coordinates, is taken to be

$$V_{ij} = f_C(r_{ij}) \left[f_R(r_{ij}) + b_{ij} f_A(r_{ij}) \right], \tag{2.22}$$

where

$$f_R(r_{ij}) = A_{ij} \exp(-\sigma_{ij} r_{ij}), \quad f_A(r_{ij}) = -B_{ij} \exp(-\mu_{ij} r_{ij}), \tag{2.23}$$

$$f_C(r_{ij}) = \begin{cases} 1 & \text{for } r_{ij} \leq R_{ij}, \\ \frac{1}{2} + \frac{1}{2} \cos\left(\pi \frac{r_{ij} - R_{ij}}{S_{ij} - R_{ij}} \right) & \text{for } R_{ij} < r_{ij} \leq S_{ij}, \\ 0 & \text{for } r_{ij} > S_{ij}. \end{cases} \tag{2.24}$$

$$b_{ij} = \left(\chi_{ij} \left(1 + \beta_i^n \sum_{k \neq i,j} f_C(r_{ik}) g(\theta_{ijk}) \right) \right)^{-1/2n} \tag{2.25}$$

$$g(\theta_{ijk}) = 1 + c^2/d^2 - c^2/\left[d^2 + (\cos\theta_{ijk} - h)^2 \right] \tag{2.26}$$

$$\sigma_{ij} = \frac{\sigma_i + \sigma_j}{2}, \quad \mu_{ij} = \frac{\mu_i + \mu_j}{2}, \quad A_{ij} = (A_i A_j)^{1/2}, \quad B_{ij} = (B_i B_j)^{1/2} \tag{2.27}$$

$$R_{ij} = (R_i R_j)^{1/2}, \quad S_{ij} = (S_i S_j)^{1/2} \tag{2.28}$$

The term b_{ij} depends on the bond angles and distances involving a third atom k. This term is crucial for capturing the angular dependence of bond energies in covalent systems. i, j, and k label the atoms of the system, and θ_{ijk} is the bond angle between bonds ij and ik. σ_i and μ_i, depend only on the type of atom. χ regulates the strength of the heteropolar bonds, allowing to include "chemistry", in the choice of the interpolation formula. The Tersoff potential is highly versatile for simulating multicomponent systems, particularly in cases where interactions between atoms of different chemical species are not well understood. By introducing a systematic approach to interpolate between potentials of different elements, and thanks to the incorporation of both two-body and three-body terms, it accurately represents bond energies and angles, making it a relevant tool for simulating a wide range of materials, including those with complex, multi-element compositions.

The most severe limitations arise because this potential captures acoustic phonon branches and elastic constants reasonably well, but it tends to systematically over-shift optical modes because of the lack of explicit long-range Coulomb interactions. Near the Brillouin zone boundaries it also often fails to reproduce the characteristic flattening of transverse acoustic and optical branches seen in ab-initio dispersions, leading to some inaccuracy in high-frequency phonon lifetimes and scattering rates. Reparameterizing the potential often improves one set of modes at the expense of others—highlighting an rather intrinsic trade-off in its short-range bond-order formalism and limiting its predictive accuracy for temperature-dependent and interfacial thermal transport studies.

Notwithstanding the empirical approach, the resulting flexibility allows exploring new materials and predicting their properties without requiring extensive empirical or machine learned data for every possible atomic interaction, especially for a qualitative description of the system under study. Building on such versatility, we applied it for modeling GaAs/Ge systems, even if direct empirical data for GaAs/Ge interactions is limited, thanks to the combination of parameter sets from other research papers that provide detailed potential parameters for GaAs and Ge individually. The use of these parameters within the Tersoff framework enabled the simulation of the heteropolar interactions between Ga, As, and Ge atoms, in turn allowing to probe into the properties of GaAs/Ge systems.

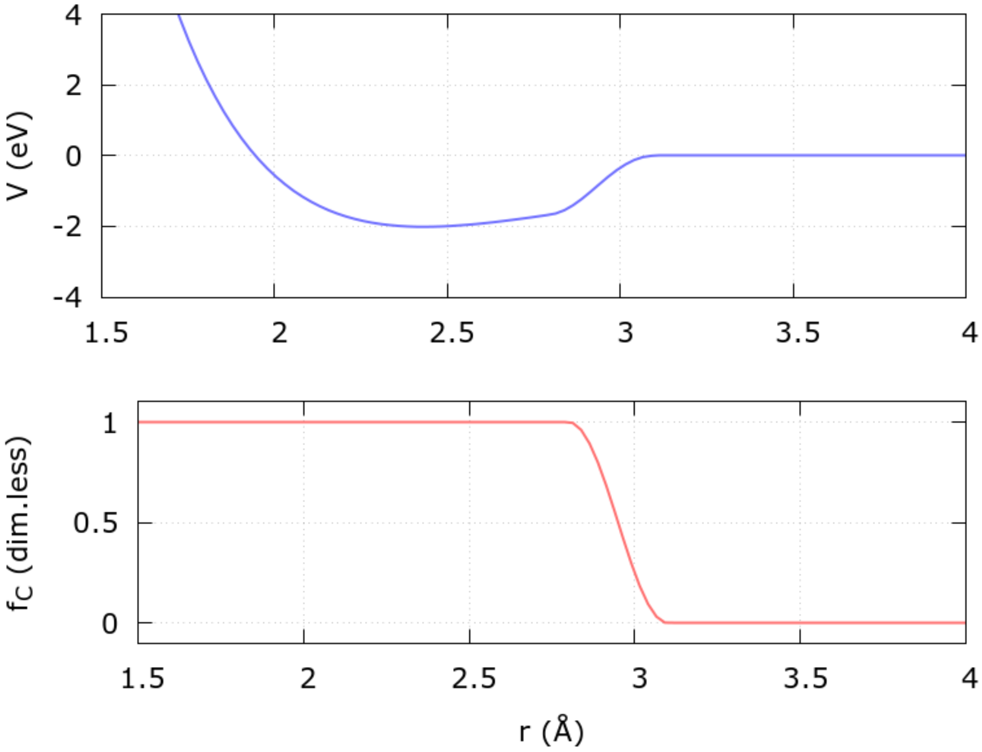

Figure 2.5: Original Tersoff potential and cutoff function for two Ge atoms, with no other atom influencing the bond. The reader should bear in their mind that, regardless of the absence of any third atom, strictly speaking this potential describes the interaction of two Ge atoms in bulk Ge. This effective interaction can be very different from the interaction between two Ge atoms in vacuum.

2.6.2 Nonequilibrium Molecular Dynamics

Nonequilibrium Molecular Dynamics (NEMD) is an extension of MD used to study systems that are not in thermodynamic equilibrium, such as systems undergoing heat or mass transfer. In NEMD simulations, one often needs to control the temperature of the system. This is typically achieved by coupling the system to a heat bath using a thermostat. A popular thermostatting technique is velocity rescaling, where the velocities of the particles are rescaled periodically to maintain the desired temperature. It works by comparing the instantaneous temperature of the system to the desired temperature and rescaling the velocities accordingly. Let T be the instantaneous temperature of the system and T_{desired} be the desired temperature. The rescaling factor α is calculated as:

$$\alpha = \sqrt{\frac{T_{\text{desired}}}{T}} \tag{2.29}$$

Then, each velocity vector $\mathbf{v}_i$ is scaled by α:

$$\mathbf{v}_i \to \alpha \mathbf{v}_i \tag{2.30}$$

This rescaling process is performed at regular intervals during the simulation to keep the system at the desired temperature. This technique is computationally efficient and straightforward to implement, making it a popular choice for NEMD simulations, when the region of interest of the physical system under study is far away from the regions where rescaling takes place. Other thermostats, like the Andersen or Berendsen provide slight modifications of such a technique, while others, like the Nosé-Hoover thermostat, modify the equations of motion to include a friction term, and are more suitable for probing into the physical properties of the regions where control over temperature takes place. When it's possible, velocity rescaling thermostatting techniques are preferred in NEMD simulations due to their simplicity and efficiency. They provide good temperature control and are easy to implement, making them suitable for a wide range of applications. Additionally, they introduce minimal perturbation to the system dynamics, allowing for more accurate simulations of nonequilibrium processes. In NEMD simulations, it's essential to equilibrate the system before collecting production data to ensure that the system reaches a stable state. Equilibration involves running the simulation for a sufficient time until the system properties no longer change significantly.

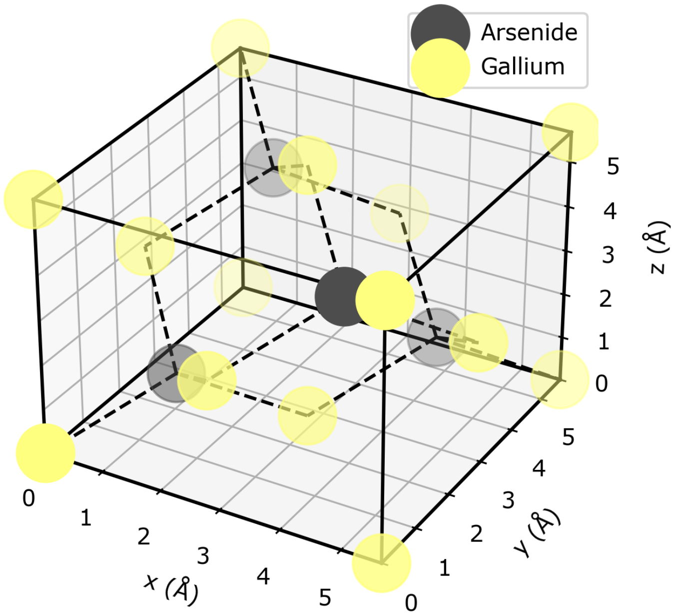

Figure 2.6: The GaAs zincblende conventional unit cell. Different chemical species are depicted using false colors as following: Gallium in yellow and Arsenic in grey. Dashed lines represent chemical bonds. Lower opacity helps visualizing the structure, and usually indicates greater distance from the observer.

2.7 The GaAs/Ge junction

To generate the GaAs/Ge junction, we stack M × M × N supercells of the zincblende (ZB) unit cell with a lattice constant of 0.5655 nm, designating GaAs in the lower half and Ge in the upper half. N defines the length of the computational cell along the transport direction, while M × M defines the cell's cross section. The zincblende crystal structure, also known as the sphalerite structure, is a face-centered cubic (FCC) lattice arrangement commonly found in semiconductors. This structure features a binary compound where two different types of atoms, such as Gallium and Arsenic occupy tetrahedral sites within the FCC lattice of the crystal. In the specific case of GaAs, the zincblende structure is characterized by Gallium and Arsenic atoms forming a tetrahedral coordination. Each Gallium atom is surrounded by four Arsenic atoms, and vice versa, creating a highly symmetric and stable configuration. This arrangement endows the material with unique electronic and optical properties, contributing to make GaAs a widely used semiconductor in various electronic and optoelectronic applications. The zincblende structure is notable for its high symmetry and efficient packing, which are key factors in the performance of devices constructed from materials with this lattice.A visual representation of the unit cell and of the thermal junction is given by Figures 2.6 and 2.7 respectively.

2.7.1 Tersoff potential for GaAs/Ge

We conduct NEMD simulations using the LAMMPS code [29]. We use a bond-order potential of the Tersoff type to describe atomic interactions, employing Nordlund's parameterization for GaAs and Tersoff's original parameterization for Ge, with mixed interactions obtained according to the specified prescriptions [30]. The numerical values of the parameters are provided in Table 5.1 Although a machine learning parameterized interatomic potential has been proposed by Wyant et al., no data on TBR are available for comparison [31].

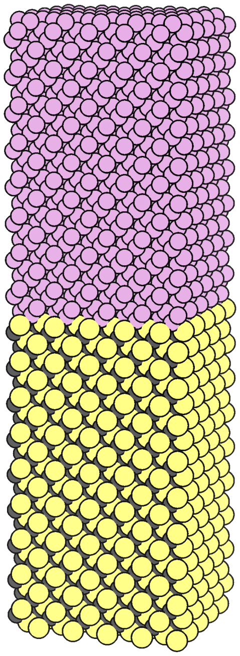

Figure 2.7: The 180 nm × 8 nm^2 GaAs/Ge junction with atomically flat interface–focus on the interface region. Ga and As atoms have been colored according to the palette of Figure 2.6, while Ge atoms have been depicted in purple.

2.7.2 Securing the steady-state

In molecular dynamics simulations, achieving a nonequilibrium steady state (NESS) is crucial for accurately studying thermal transport properties across heterojunctions. The NESS is characterized by a balance between energy injection and extraction, ensuring that the system's thermal and kinetic properties become time-independent. This state allows for the reliable computation of parameters such as heat flux and interface temperature drop, which in turn give the TBR. In our simulations, we employ structural relaxation followed by temperature biasing and thermostatting by velocity-rescaling to drive the system towards this steady state, ensuring the robustness and reliability of our results. First, we perform a structural relaxation of the heterojunction under constant volume conditions. The [001] axis is aligned with the z direction, designated as the transport direction, while periodic boundary conditions are applied in the xy plane. Subsequently, we initialize the atomic velocities by sampling from a Maxwell-Boltzmann distribution at 300 K. A temperature gradient $\Delta T = T_A - T_B = 100$ K, centered around 300 K, is imposed, where T_A and T_B are the temperatures at the hot and cold ends, respectively, enforced by velocity rescaling. The thermostatted regions each span approximately 1.12 nm [see Figure 2.3 for a depiction of the computational setup; materials A and B correspond to GaAs and Ge respectively]. The system evolves in time with a time step of 0.7 fs, and the simulations usually run for up to 7 ns.

The selection of a 0.7 fs timestep ensures numerical stability and energy conservation by resolving the fastest atomic vibrations well below one-tenth of their periods. Running the simulation for approximately 7 ns (10 million steps) provides ample sampling to establish steady-state transport and reduce statistical uncertainty in observables like fluxes and thermal conductivity. A cross-section of about 8 nm^2 balances computational efficiency against finite-size effects, and prevents spurious self-interactions under the periodic boundaries along the X and Y axes; while extending the junction to about 180 nm along the Z direction, where no periodic boundary condition is set, allows uninterrupted development of thermal gradients, and avoidance of non-physical effects near the thermostatted regions. Together, these choices enable convergence of nonequilibrium steady states, and suppress periodic artifacts—thereby yielding robust confidence in the simulated nanoscale transport phenomena.

Details on the numerical integration technique

To perform the numerical simulations, we chose the velocity form of the Störmer – Verlet algorithm (velocity–Verlet), which is the time integrator commonly used in NEMD to solve Newton's equations of motion and which is directly available in LAMMPS. At each timestep, velocities are advanced by a half-step using current forces, positions are then updated by a full step using those intermediate velocities, forces are recalculated on the new positions, and finally velocities are completed with a second half-step update. This symmetric splitting guarantees time-reversibility and symplectic conservation, minimizing energy drift over long simulations. The two-stage structure also lends itself to efficient, parallelized force evaluations, enabling stable integration even under strong nonequilibrium conditions such as the typical thermal gradients encountered in our simulations.

2.7.3 Post-processing

To analyze the data, we track the energy injected and extracted by the thermostats at the junction ends over time [Figure 2.8a]. When the ratio of energy injection to extraction stabilizes within numerical tolerance, we consider the system to have reached a nonequilibrium steady state. This is determined by examining the time-independence of the difference between injected and extracted energies [Figure 2.8b]. Typically, after an initial transient phase of about 1 ns, the system reaches steady state; we discard an additional 1 ns for stabilization and use the remaining 5 ns for averaging. Once the steady-state time window is identified, we use this period to compute the average heat flux and temperature profile, $T(z)$, to estimate the thermal boundary resistance (TBR). From the slopes of the injected and extracted energy curves, we determine the total power input at the hot end and output at the cold end. The difference between these values provides an estimate of residual energy, ensuring no drift from steady-state conditions. The heat flux is calculated as the injected (or extracted) power divided by the cross-sectional area.

The difference between the input and output heat fluxes, indicating the robustness of the achieved nonequilibrium steady state, is typically around 0.2%. The average temperature profile is obtained by time-averaging and spatially averaging the instantaneous atomic temperatures in the xy plane, expressed as $2E_k/(3k_B)$, where E_k and k_B are the kinetic energy and Boltzmann constant, respectively. Linear fits of the temperature profile on either

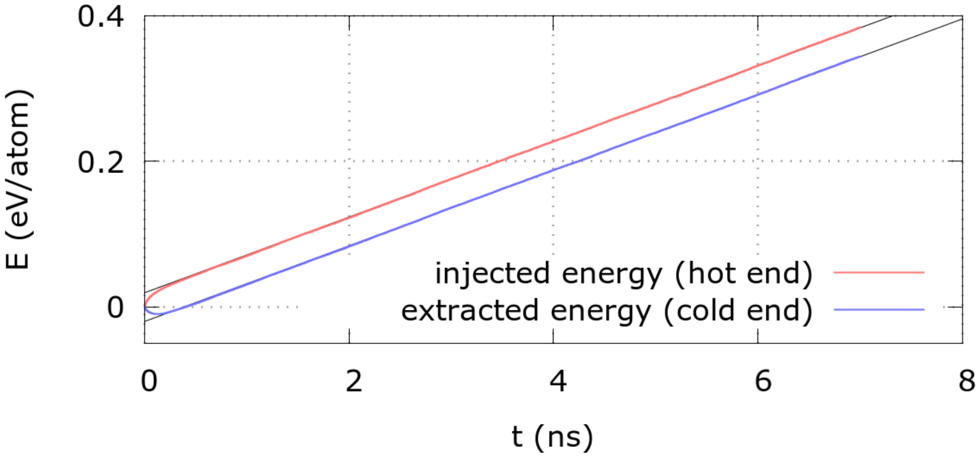

(a) injected and extracted energy

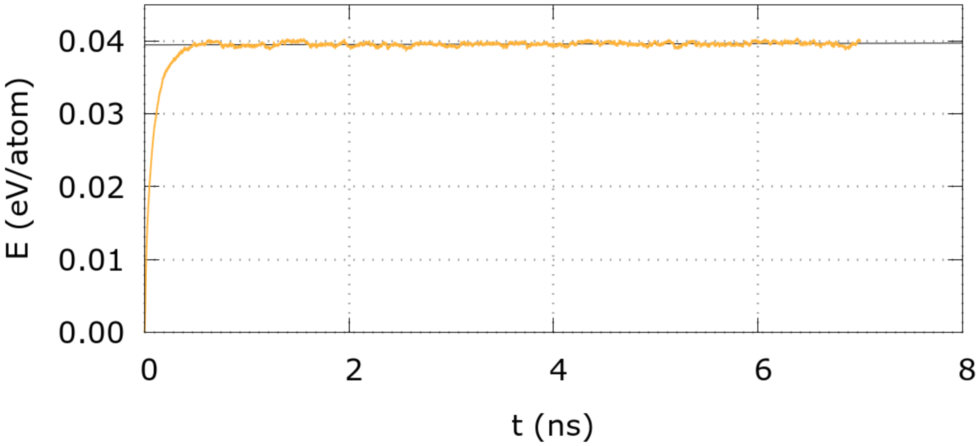

(b) residual energy

Figure 2.8: (a) Total energy injected and extracted by the two thermostats over time, represented by the red and blue curves, respectively. The ratio of the slope to the cross-sectional area indicates the heat flux through the hot and cold ends. (b) Difference between injected and extracted energies over time, showing the residual energy. A positive residual energy indicates that the system absorbed heat during the transient phase. The black solid lines represent the results of the linear fit.

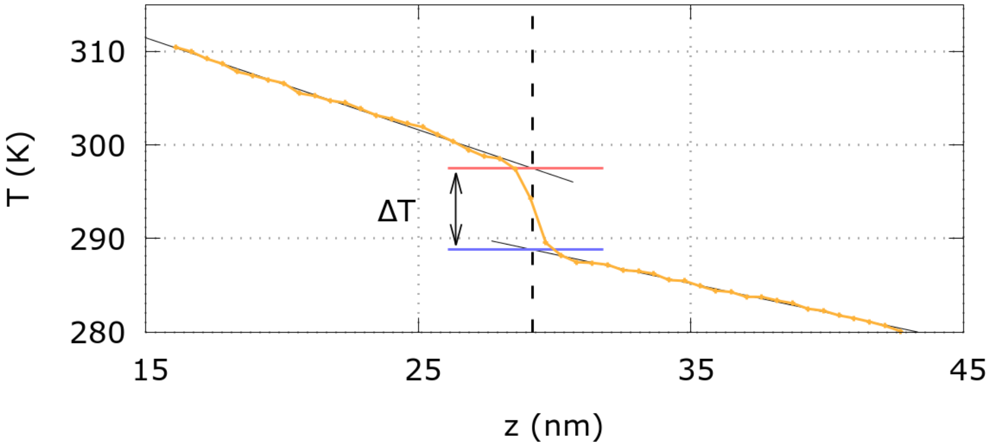

Figure 2.9: The steady-state temperature profile of the 60 nm × 8 nm^2 GaAs/Ge junction is shown, with a focus on the interface region. The fitting curves are in black, highlighting the temperature drop, and the interface position is marked with a dashed line. The black solid lines represent the results of the linear fit.

side of the interface are projected onto the interface position to extract the temperature drop, as shown in Figure 2.9. The temperature drop at the interface divided by the heat flux yields the TBR for the specific configuration. More sophisticated methods exist for determining TBR, such as those based on irreversible thermodynamics, but the heuristic approach used here is generally sufficient for understanding phonon transport across interfaces relevant to our study. For a given interface morphology and chosen potential determining atomic interactions, the TBR estimate depends on four simulation parameters: the cell cross section, the cell length, the hot end temperature (T_A), and the cold end temperature (T_B). The parameters measured include the interface temperature, heat flux, and temperature drop.

2.7.4 Finite-size effects

Here we bump into the very first and likely most obvious limitation of computational methods, and especially atomistic simulations. To carry on the study and actually perform the simulation, it is necessary to make a choice for the values of M and N. The natural question which may then arise is: what values are the most suitable? Of course, the answer depends on the specific purpose and extent of the analysis. If one was given infinite computational resources and a specific system of interest, the best choice would likely be a one-to-one mapping of every atom in the physical system to an atom in the corresponding simulation. In most practical applications, however, the number of atoms that can be taken into account is rather limited–about three order of magnitude lower, in comparison to the number of atoms of the real systems to be described. Periodic Boundary Conditions (PBC) and other symmetries can often be exploited to simplify the computation and extend the results, but this approach is rather unfeasible for systems which are out of equilibrium, where by definition some symmetry is broken by default. For this reason, it is customary to simulate smaller versions of the system, and look for convergence of the physical properties to some fixed values, when the scale of the simulation is progressively increased. Such values are then assumed to provide the correct description of the bulk, or infinite system. This point is crucial in atomistic simulations, because finite-size effects turn out to play a significant role in determining the phonon dynamics, and largely influence thermal transport properties, becoming sharply pronounced when material dimensions approach the phonon MFP [32]. In particular, we can identify several sources of deviation from the bulk-like case.

Boundary Scattering

As material dimensions shrink, boundary scattering increases, reducing the phonon mean free path. This disrupts phonon propagation and decreases thermal conductivity. The scattering rate also depends on surface roughness and boundary nature [33].

$$\frac{1}{\tau_{eff}} = \frac{1}{\tau_{\text{bulk}}} + \frac{1}{\tau_{\text{boundary}}} \tag{2.31}$$

where τ_{eff} is the effective phonon relaxation time, τ_{bulk} is the bulk phonon relaxation time, and τ_{boundary} is the boundary scattering relaxation time.

Phonon Confinement

In thin films, nanowires, and nanoscale systems in general, phonon modes are discrete due to confinement, altering dispersion relations, group velocities, and lifetimes. This directly modifies the phonon density of states, specific heat, and thermal transport properties [34]. For a monodimensional string of length L with both ends kept fixed, the set of characteristic frequencies–i.e. the phonon spectrum–is given by

$$\omega_n = \frac{n\pi c}{L} \tag{2.32}$$

where ω_n is the quantized phonon frequency, c is the sound velocity, L is the characteristic dimension of the material, and n is a non-negative integer not exceeding N.

Phonon-Phonon Interactions

Finite sizes influence phonon-phonon interactions too, especially higher-order processes. In nanostructures, enhanced four-phonon scattering can dominate over three-phonon processes, increasing thermal resistance [35].

$$\frac{1}{\tau_{\text{ph-ph}}} = \frac{1}{\tau_{3\text{ph}}} + \frac{1}{\tau_{4\text{ph}}} \tag{2.33}$$

where $\tau_{3\text{ph}}$ and $\tau_{4\text{ph}}$ are the three-phonon and four-phonon scattering relaxation times, respectively.

Reduction in Thermal Conductivity

Finite-size effects lead to reduced thermal conductivity due to increased boundary scattering and modified phonon dispersion. For instance, nanowires and thin films exhibit significantly lower thermal conductivity than bulk materials [36].

$$\kappa = \frac{1}{3} c \Lambda C \tag{2.34}$$

where κ is the thermal conductivity, C is the specific heat, c is the phonon velocity, and Λ is the phonon MFP.

Anisotropy and Non-equilibrium

In low-dimensional systems, thermal conductivity can become strongly anisotropic, arising from different phonon scattering rates and mean free paths in different directions or confinement dimensions. Different phonon polarizations and wavevectors have varying relaxation times, impacting energy distribution [37, 38].

Temperature Dependence

The thermal conductivity of nanoscale materials shows a stronger temperature dependence compared to bulk materials, due to enhanced phonon-phonon scattering at higher temperatures and increased boundary scattering at lower temperatures. A typical proportionality law is found to be

$$\kappa \propto T^{-n} \tag{2.35}$$

where n varies depending on the dominant scattering mechanism (e.g., $n \approx 1$ for three-phonon scattering, $n \approx 1.2$ for combined three- and four-phonon scattering) [39].

2.7.5 Simulation of the atomically flat junction

To tackle into this long list of intricate thermal transport features for the GaAs/Ge junction, we conducted a several series of simulations, each one of which deals with the dependence of the TBR on some specific internal (e.g. chemical composition, roughness) or external (e.g. average T, ∇T) parameter.

Cell geometry

Ideally speaking, we would like to compute the TBR for the bulk system. Since we can not simulate an infinite system, we need to consider increasingly larger cells until the computed values don't change much when the system size further increases. To track the dependency on the geometry of the junction, we simulated seven different values for the junction length, specifically from 60 to 300 nm, using three distinct cross-sectional areas: 8, 11.5, and 15.6 nm^2. This was performed under two specific thermal conditions: a fixed thermal bias $\Delta T = 100$ K and a fixed temperature gradient $\nabla T = 1.67$ K/nm, while maintaining an average temperature of 300 K. It is important to notice that while NEMD offers a straightforward and rather reliable way to probe into all of the effects mentioned above–because it is a non-perturbative approach in which the classical equations of motion are solved exactly–the different contributions are inevitably convoluted in determining the thermal properties of the junction. We plotted the results of the simulations in Figure 2.10. From our simulations, we found that the results for a cross-sectional area of 8 nm^2, corresponding to a 5×5 repetition of the standard unit cell, already displayed convergence. Furthermore, we discovered that extending the cell length to 180 nm was necessary to achieve reasonably convergent TBR values. These findings are in agreement across different thermal conditions, suggesting that TBR is more influenced by the interface temperature rather than the specific details of the thermal gradient or bias, aligning with observations from previous studies [25].

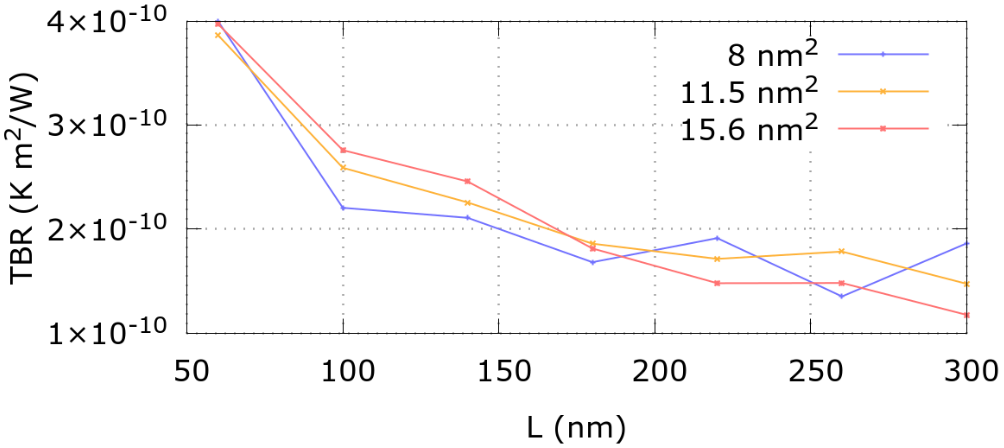

(a) constant ΔT

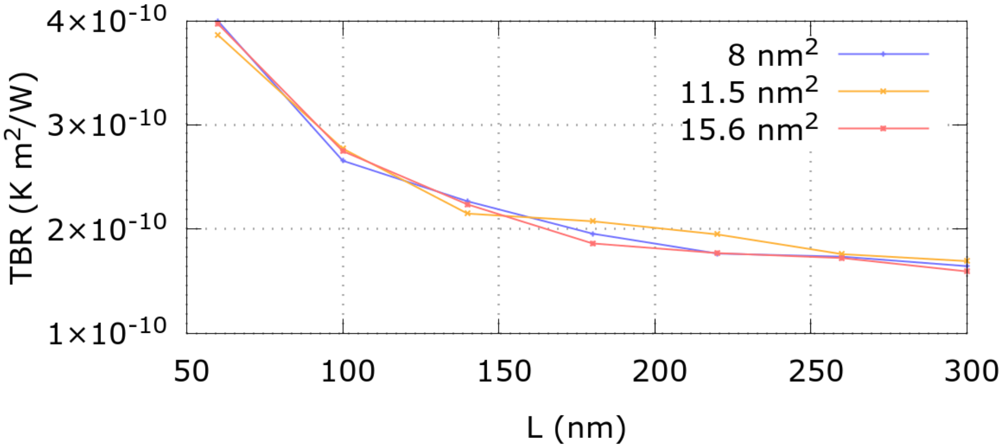

(b) constant ∇T

Figure 2.10: The TBR dependence on the cell geometry with (a) constant ΔT and (b) constant ∇T. The different lines correspond to different cross-sectional areas.

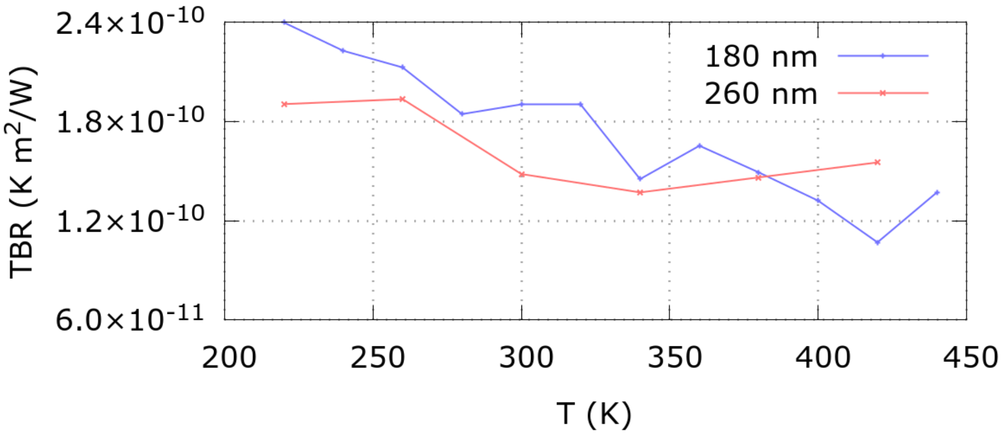

Figure 2.11: TBR dependence on temperature for the 180 nm × 8 nm^2 (blue) and 260 nm × 8 nm^2 (red).

2.7.6 Temperature dependence

Next, we use the 8 nm^2 x 180 nm geometry that provided consistent TBR results and run 12 simulations with average temperatures evenly ranging from 220 to 440 K, maintaining a thermal bias of $\Delta T = 100$ K between the ends of the cell. As the system's temperature increases, two main effects are observed. First, according to Bose–Einstein statistics—which we assume under local thermodynamic equilibrium and which dictate the phonon state populations—there will be more energy carriers on both sides of the heterojunction. However, the imbalance of these carriers, rather than their sheer number, primarily affects the TBR. Therefore, an increase in phonon population alone should not influence the TBR. More significantly, higher temperatures increase the system's anharmonicity, which broadens the phonon lines and reduces the difference between the phonon spectra of the two materials at the heterojunction. This effect is illustrated in Figure 2.11 where the TBR decreases with increasing interface temperature. When fitting this decrease to a power law of the form T^{-n}, we find $n \approx 1$. We also calculated the TBR in larger computational cells with $L = 260$ nm, obtaining results of similar magnitude. It is important to note that our results at lower temperatures should be interpreted qualitatively. This limitation arises from the classical molecular dynamics approach employed, which neglects quantum mechanical effects and assumes phonon populations follow Maxwell–Boltzmann statistics instead of Bose–Einstein statistics. Consequently, this approximation is more accurate at higher temperatures, where classical behavior dominates [40].

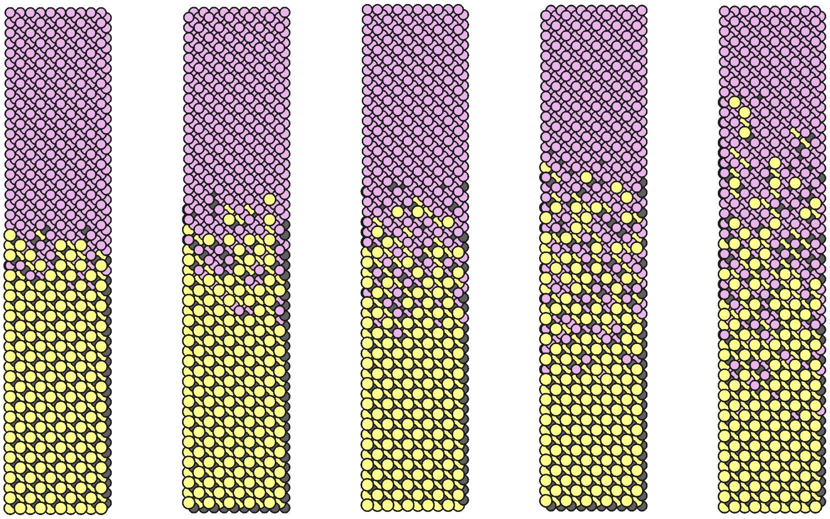

Figure 2.12: 180 nm × 8 nm^2 GaAs/Ge junction when chemical mixing is present–focus on the interface region. We display the linear case, with $L_{mix} =$ 2, 4, 5, 7.5 and 10 nm.

2.7.7 Chemical mixing

Atomically flat interfaces represent an idealized limit, whereas real-world interfaces typically exhibit a range of non-ideal characteristics. Among the most significant of these are chemical intermixing and interface roughness. Chemical intermixing pertains to interfaces where the chemical composition transitions gradually rather than abruptly, unlike in atomically flat interfaces. This gradual change creates a region where the chemical species are intermixed, forming an alloy with a varying composition, as depicted in Figure 2.12. Interface roughness, on the other hand, refers to interfaces that are chemically abrupt but not physically flat, as shown in Figure 2.17. Consequently, we also consider these more realistic morphologies in our study. For the case of chemical intermixing, we begin by assuming a linear variation in composition within a mixing region defined as $[0, L_{\text{mix}}]$. Thus, for $z < 0$, we have GaAs, and for $z > L_{\text{mix}}$, we have Ge. Within the mixing region, the GaAs content is given by $1 - z/L_{\text{mix}}$. Additionally, we enhance the linear decay of the GaAs composition into Ge with an exponential factor. In this scenario, the GaAs content in the mixing region is $(1 - z/L_{\text{mix}})e^{-az/L_{\text{mix}}}$, where $a = 2\ln(3/2), 2\ln(5/2)$ are arbitrary but reasonable non-negative con-

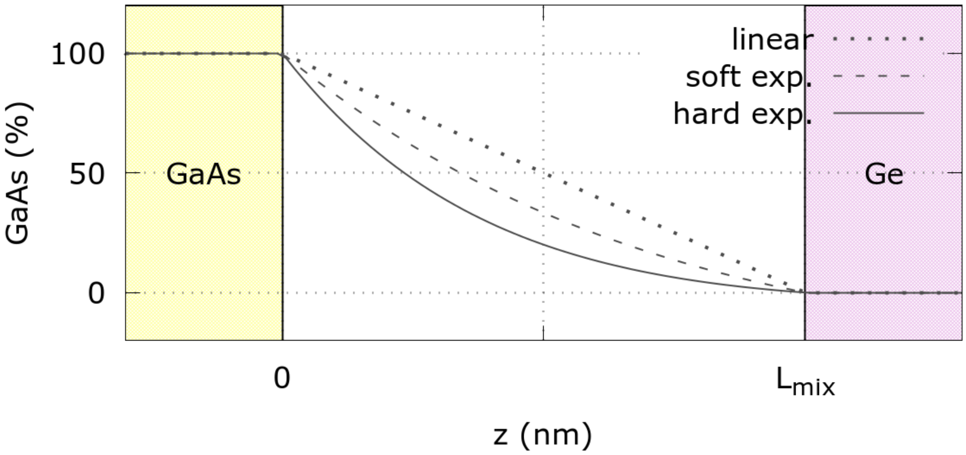

Figure 2.13: GaAs concentration along the z axis for the three case studies: linear, soft, and hard exponential respectively.

stant values for regulating the decay. This situation is schematically depicted in Figure 2.13. We investigate the impact of chemical mixing on the thermal boundary resistance (TBR) by varying L_{mix} from 1 to 10 nm. Due to the stochastic nature of the alloy generation process, which involves randomly selecting the chemical species of atoms based on a target probability, we verified that different random seeds did not affect our conclusions. Our findings, illustrated in Figure 2.14, show a linear dependence of the TBR on L_{mix} regardless of the composition varying linearly or not. This behavior can be understood by considering the typical dependence of the thermal conductivity, κ, of alloys on their composition. For instance, in $\mathrm{Si}_{1-x}\mathrm{Ge}_x$, κ exhibits sharp variations for x close to 0 and 1, but remains fairly constant for intermediate compositions. Consequently, we can approximate the thermal conductivity of the mixing region as constant, resulting in the overall thermal resistance scaling linearly with L_{mix}. A similar dependence is observed when the decay is exponentially enhanced, although the specific results are not particularly influenced by the chosen damping factor a.

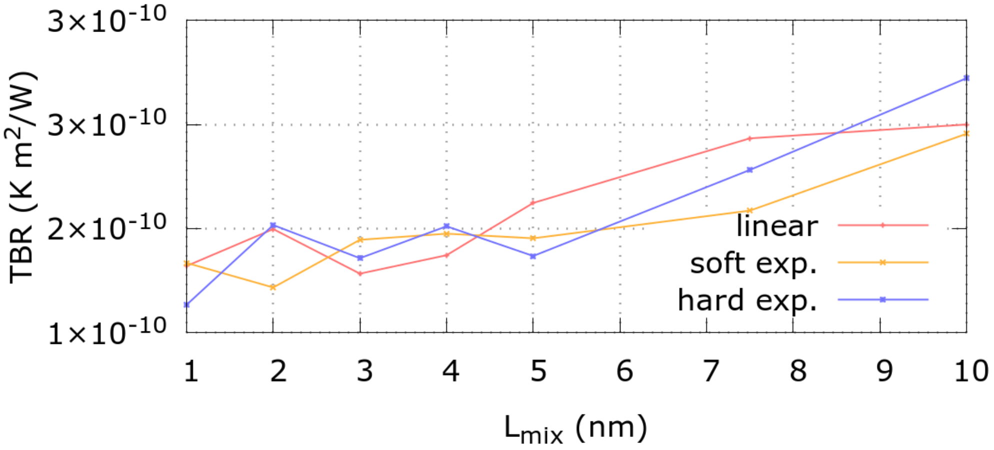

Figure 2.14: TBR dependence on L_{mix} for the 180 nm × 8 nm^2 geometry and different mixing styles.

Constant mixing

We also consider the specific case where the interface between GaAs and Ge exhibits a well-defined mixing region of 5 nm in length, and within this region the concentration of Ge atoms remains constant relative to GaAs, creating a uniform chemical composition. The results are shown in Figure 2.15, and indicate a maximum value for the TBR at equal concentrations, in alignment with previous reports [41].

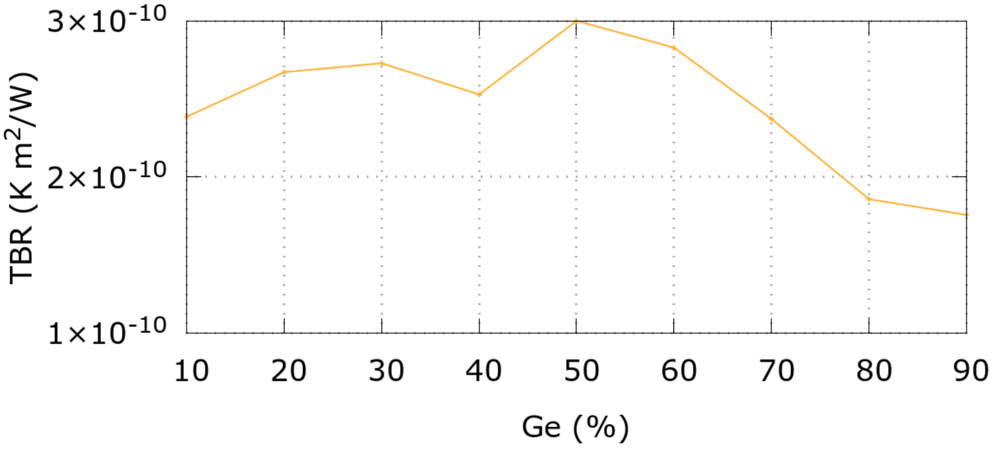

Figure 2.15: TBR values VS Ge concentration for the constant mixing case, with $L_{mix} = 5$ nm. The maximum value of the TBR is obtained for equal GaAs and Ge concentration.

2.7.8 Surface roughness

We also examined the influence of interface roughness on TBR. Interfaces with higher roughness usually exhibit increased TBR due to enhanced phonon scattering at the interface. This is corroborated by previous studies that highlight the significant role of interface quality on thermal transport in nanostructures [42]. Interface roughness creates additional scattering sites, disrupting coherent phonon transport and increasing thermal resistance [43]. To simulate this effect, we produce random surfaces with correlation lengths of 1.2 nm and amplitude ranges of 2, 4, and 6 nm, also employing two different seeds in this scenario. One of the random surfaces used for separating GaAs and Ge, and a cartoon of the junction exemplifying surface roughness, are provided by Figures 2.16 2.17. The relationship of the TBR is depicted in Figure 2.18. Our results suggest that, at this level, surface roughness has a minimal impact on the TBR, with variations being so slight that different seeds yield slightly varied trends. Although a positive correlation between the root mean square (RMS) of the interface roughness and an increase in TBR has been observed [44], it tends to emerge for roughness RMS values larger than those considered here, i.e., RMS ≥ 1 nm (note that the selection

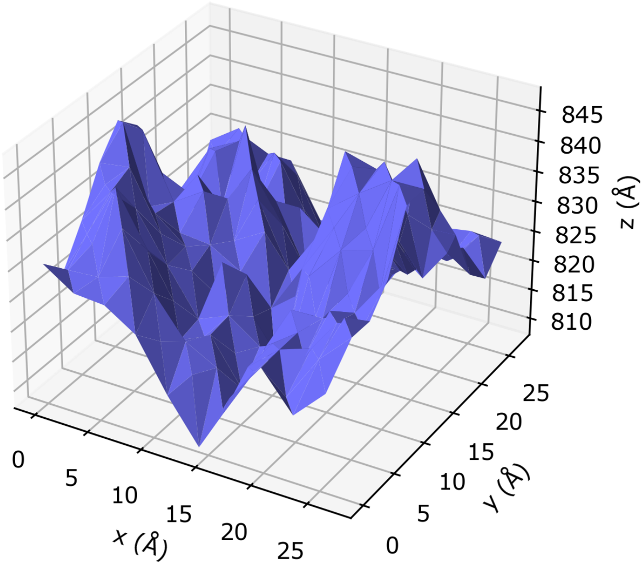

Figure 2.16: Random surface used to separate GaAs and Ge, with 4 nm min-to-max amplitude and 0.8 nm RMS.

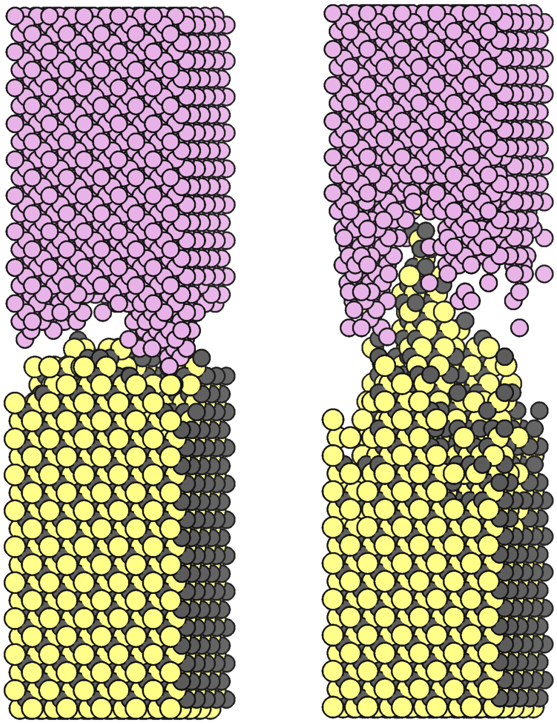

Figure 2.17: GaAs/Ge junction with surface roughness and min-to-max amplitudes of 2 nm and 6 nm. The RMS equal 0.4 and 1.2 nm respectively. We applied a vertical displacement to Ge atoms for better visualization purposes.

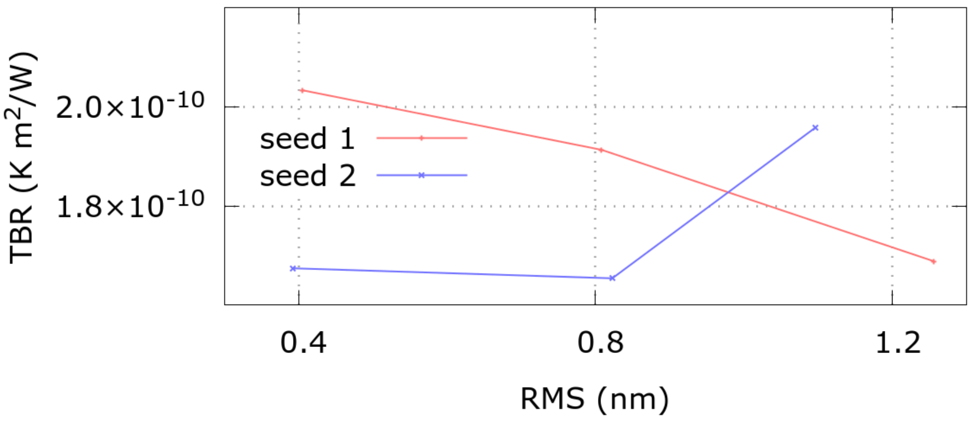

Figure 2.18: Caption

of an appropriate RMS is practically restricted by the computational cell cross-section).

2.7.9 Thermal rectification

Let's now explore the concept of thermal rectification. Given that the system is not uniform along the transport direction, reversing the thermal gradient will alter the thermal conductance [45, 46]. A plot of the steady-state temperature profile for the 60×8 nm^2 junction in the forward and reverse bias setup is provided by Figure 2.19 In a bimaterial setup, such as the one we're examining, thermal rectification arises from two primary factors. Firstly, the distinct temperature dependence of thermal conductivity in the materials on either side of the junction leads to different overall thermal resistances under forward and reverse bias [47]; secondly, the interface temperature, T_i, will generally differ between forward and reverse bias [48] and so will the TBR, due to its temperature-dependent behavior. The former factor is intrinsic to the materials on either side of the junction, like the thermal conductivity of GaAs and Ge here, while the latter effect is typically significant only at the nanoscale and becomes negligible compared to the overall thermal resistance when the TBR's relative impact diminishes [25, 26]. Our results for thermal rectification, γ, as a function of cell length, L, are shown in Figure 2.20. We

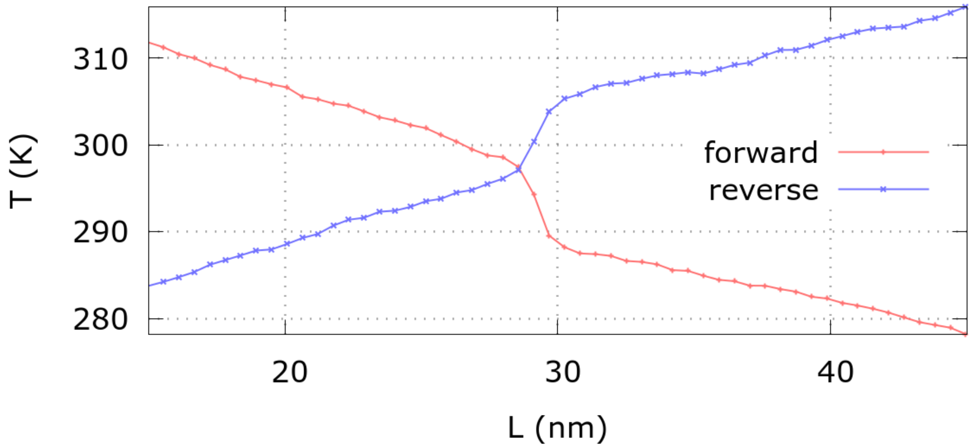

Figure 2.19: Steady-state temperature profile for the 60 × 8 nm^2 geometry in the forward (red) and reverse bias (blue) respectively–focus on the interface region.

define the forward bias as the condition where heat flows from GaAs to Ge, with thermal rectification given by

$$\gamma = \frac{G_{\mathrm{for}} - G_{\mathrm{rev}}}{G_{\mathrm{rev}}} \tag{2.36}$$

where G_{for} and G_{rev} are the thermal conductances under forward and reverse biases, respectively. For each cell length L, we calculate the thermal conductance for a fixed ΔT, adjusting $|\Delta T|$ as L increases to maintain a consistent thermal gradient of 1.7 K/nm across all cell sizes. Initially, rectification is negative, switches sign around $L \approx 150$ nm, and subsequently increases 2.20a. This behavior is attributed to a balance between the two aforementioned effects: at smaller L, the temperature dependence of the TBR dominates the rectification, but as L grows, the TBR's influence diminishes and becomes a small part of the total thermal resistance. Once TBR's effect is negligible, the rectification solely depends on the temperature dependence of the materials' thermal conductivities, resulting in phonons flowing preferentially from GaAs to Ge. However, we do not observe an asymptotic situation, as γ increases for all cell sizes examined. To estimate TBR-free rectification values, we use standard methods to extrapolate thermal conductivities for infinitely large

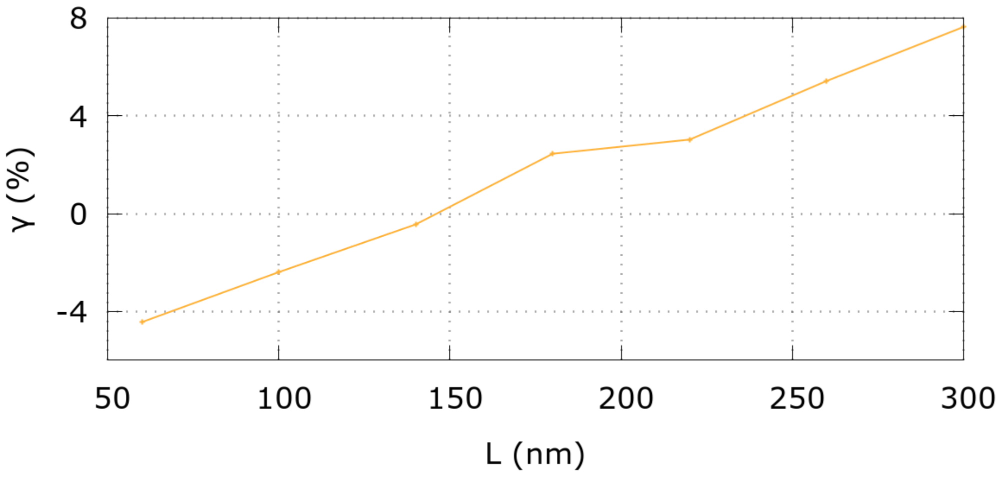

(a) γ

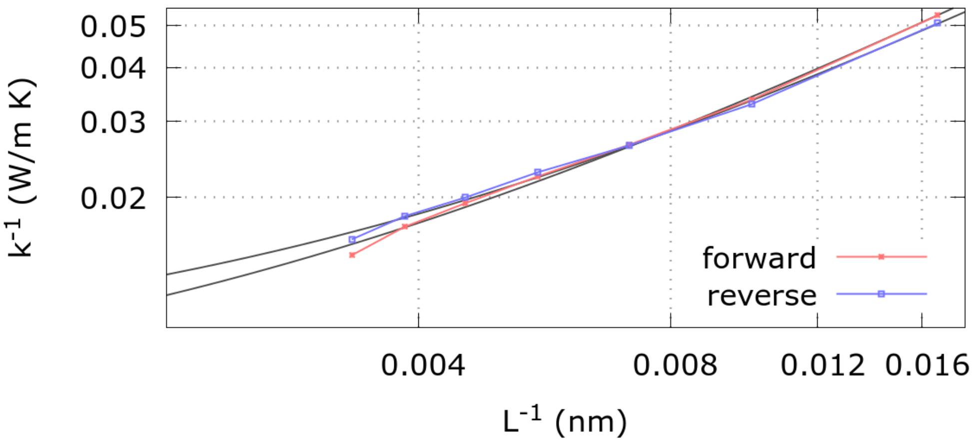

(b) κ^{-1}

Figure 2.20: (a) Rectification coefficient and (b) $\kappa_{for/rev}$ dependence on the junction length L, in red and blue respectively. The results of the linear fit are shown in grey. In (b) log scale has been used for better visualization purposes.

cells [49, 50], plotting $1/L$ vs $1/\kappa$ in the two cases, and performing a linear fit to each one. The intercept of each line provides us with the reciprocal κ in the infinite length limit, from which the rectification coefficient can then be computed. This yields an effective thermal conductivity for the GaAs/Ge system under forward and reverse biases for the infinitely long system (see Figure 2.20b), resulting in a rectification value of $\gamma_\infty = 0.3$.

2.7.10 A note on uncertainty estimation

Uncertainty in computed conductivities and TBRs originates largely from the finite duration and size of NEMD runs, which constrain phonon sampling and give rise to statistical fluctuations in the heat flux and temperature discontinuity at the interface. While a 0.7 fs timestep remains safely below one-tenth of typical phonon vibration periods—thereby limiting systematic integration error—some residual numerical drift can still bias the TBR. The analysis of the steady state, together with the convergence study with respect to the cross-section ensure periodic boundaries and simulation time do not introduce excessive noise on the heat flux or phonon self-interactions across images, which would smooth temperature gradients and lead to underestimating TBR and rectification. As well, the convergence study with respect to the cell length ensures we achieved a reasonable compromise between simulation cost and confidence with the results. Extending the simulation to 7 ns (10 million steps) also reduces the standard error of mean heat flux and temperature drop, but even multi-nanosecond runs sample only a finite subset of mode lifetimes, leaving some latent uncertainty in the TBR. In our case, the preferred system size exhibits a relative uncertainty of about 5.5% for both the constant ΔT and ∇T configurations, which provides us with a qualitative order of magnitude of the uncertainty in the rest of the analysis.

Rectification factors further compound these errors—being ratios of forward and reverse measurements-so that in our case it becomes reasonable expecting uncorrelated uncertainties to amplify the relative error on rectification up to about 10-15%. Further convergence testing—longer system dimensions, simulation time, and varying integration parameters—as well as employing multiple independent runs, would be essential to bound both statistical and systematic uncertainties, ensuring that reported TBR and rectification values faithfully represent interfacial transport of bulk systems, truly unaffected by any simulation artifacts. Nonetheless, this approach would not circumvent the empirical nature of the Tersoff potential and the mixed parameters, making data-driven machine-learned potential a necessary element in order to achieve reasonable predictive power from the simulations.

2.8 Conclusion of Chapter 2

In conclusion, our investigation into the thermal transport properties of the GaAs/Ge heterojunction using NEMD has provided valuable insights. We have determined that the TBR for atomically flat interfaces aligns with values found in similar systems. However, it is crucial to account for the non-negligible size effect when estimating TBR, necessitating computational cells of at least 180 nm to achieve reliable results. Our findings also confirm that the TBR decreases with increasing interface temperature, and the rate of this decrease is slower than what semiclassical phenomenological models predict. This deviation highlights the complexity of thermal transport at the nanoscale, necessitating advanced modeling techniques to capture these nuances accurately. We further examined the impact of various morphological imperfections, such as graded and rough junctions, on the TBR, revealing that these imperfections significantly influence thermal transport, and must be considered in the design of thermally efficient devices. Notably, we have demonstrated that by controlling the length of the GaAs/Ge system, it is possible to modulate thermal rectification and even reverse its direction. This phenomenon is attributed to the interplay between the temperature dependence of the TBR and the thermal conductivity of the constituent materials. At experimentally relevant sizes, the influence of the temperature dependence of the TBR diminishes, resulting in a predicted thermal rectification of approximately 30%. Future research should focus on comparing these results with those obtained using machine-learned potentials. Such comparisons could enhance the accuracy of predictions regarding thermal rectification and potentially pave the way for innovative applications in thermal management and phonon-based logic. The insights gained from this study underscore the importance of considering both size effects and interface morphology in the thermal design of semiconductor heterojunctions. The numerical results are provided in Tables 5.2 − 5.7.

Chapter 3

Multiple-Interface Thermal Transport

The study of phonon transport across multiple semiconductor interfaces, particularly in superlattices, is crucial for advancing our understanding of thermal conductivity in nanostructured materials. Superlattices, composed of alternating layers of different semiconductors, have garnered significant interest due to their potential in thermoelectric applications and thermal management technologies. This chapter delves into the mechanisms governing phonon transport across multiple interfaces within superlattices, with a specific focus on Si/Ge superlattices. Phonon transport in superlattices is fundamentally influenced by the periodic arrangement of layers and the properties of the interfaces. In Si/Ge superlattices, the mismatch in acoustic properties between Silicon and Ge creates a complex landscape for phonon scattering. Layer thickness and periodicity play pivotal roles in determining the thermal conductivity of these structures. Studies have shown that reducing the layer thickness can enhance interface scattering, thereby reducing thermal conductivity and also potentially increasing the thermoelectric efficiency of the material [51, 52]. A key challenge in this field is the accurate modeling of phonon transport across these interfaces. Theoretical approaches, such as the phonon Boltzmann Transport Equation (BTE) and MD simulations, have been employed to predict thermal conductivity. However, discrepancies between experimental measurements and theoretical predictions persist, highlighting the need for more refined models that incorporate phonon-phonon interactions at all orders [53].

Recent advancements have focused on incorporating first-principle calculations to derive material-specific phonon properties, thereby enhancing the predictive power of these models [54, 55]. In Si/Ge superlattices, phonon transport exhibits both coherent and incoherent characteristics depending on both periodicity and temperature. Coherent transport is typically observed in structures with smooth interfaces and small periods, where phonons can maintain phase coherence across multiple layers. In contrast, incoherent transport dominates in structures with larger periods, where phonon scattering at each interface disrupts coherence [56, 57]. Understanding the transition between these regimes is essential for designing superlattices with tailored thermal properties. This chapter aims to provide a comprehensive overview of the current understanding of phonon transport across multiple interfaces, where the case study is provided by the Si/Ge superlattices. Through this discussion, we seek to elucidate the factors that influence phonon transport and highlight areas where further research is needed.

3.1 Normal Modes, Phonons, and Sound

To tackle superlattices, we need to take into account some further concepts which are fundamental when dealing with phonons and phonon transport, the first of them being that of normal mode. In physics, normal modes refer to the natural vibration patterns of a system around some stable equilibrium configuration. At the harmonic level–i.e. if the Hamiltonian is quadratic– these elementary degrees of freedom do not interact with each other. Each normal mode is characterized by the specific frequency at which that mode oscillates. These modes are particularly important in understanding the behavior of complex systems such as crystalline solids. When a system is perturbed, it can vibrate in a combination of its normal modes, each contributing to the overall motion according to its frequency and amplitude. Phonons are the quantized versions of these vibrational modes in a crystal lattice. They are quasiparticles that represent the collective excitation of atoms vibrating in a periodic array, and provide the quantum mechanical description of vibrational motion in solids. The various physical properties of materials, such as thermal conductivity and electrical conductivity, is influenced by how vibrations propagate through the crystal lattice.

The relation between normal modes and phonons becomes evident when considering a crystal as a periodic arrangement of atoms connected by springs (bonding forces). This simplified picture proved extremely successful in elucidating the dynamical principles behind the complex behaviour that we witness in crystalline solids.

3.1.1 Monoatomic linear chain

The simplest possible situation is provided by the finite monoatomic linear chain of spring and masses with PBC and quadratic interactions. In this case, the primitive cell of the lattice contains only one atom, and every atom interacts only with its first neighbors. The very high degree of symmetry of this system, joint to the lack of local degrees of freedom inside of the primitive cell, forces the solution to the equation of motion to take a relatively simple form. Once we exploit the symmetry, the equation of motion become those of a simple harmonic oscillator indeed, with a n-dependent oscillation frequency $\omega(n)$. n provides the modulation of the atomic displacements from their equilibrium positions as we move along the chain at a fixed instant of time for the specific normal mode concerned, and it is an integer number not exceeding the total number of atoms N, as long as we don't take the continuum limit. The spectrum of the linear chain is given by:

$$\omega(n) = \omega_0 \sqrt{2\ [1 - \cos(2\pi n/N)]} = 2\ \omega_0\ |\sin(\pi n/N)| \tag{3.1}$$

and the dynamics of the corresponding normal modes is:

$$A_n(t) = u_n \cos(\omega_n t) + v_n \sin(\omega_n t) \tag{3.2}$$

with u_n and v_n regulating the oscillation amplitude. When time elapses, the shape of each normal mode, or relative displacements of the atoms with respect to each other, is preserved exactly, while the overall amplitude evolves according to Equation 3.2. Setting $\nu_n = 2\pi n/N$, the expression of the corresponding atomic positions for the two normal modes labelled with n becomes:

$$\begin{aligned} x^+{}_j(t) &= A^+{}_n(t)\ \cos(\nu_n j) \\ x^-{}_j(t) &= A^-{}_n(t)\ \sin(\nu_n j) \end{aligned} \tag{3.3}$$

Since the equations of motion are linear, we can take the superposition of them, and the resulting dynamics will still be a solution of the equations of motion. This is particularly important for two reasons. One has to do with phonon movement, and the other with phonon localization.

The first one becomes clear considering the superposition of two normal modes corresponding to the same value of n. We now suppress the n label for a lighter notation. If we set $u^+ = v^- = A$ and $u^- = v^+ = 0$, and consider the superposition of the two modes, we get the following expression for the displacement of the j^{th} atom:

$$x_j(t) = A\ [\cos(\nu j)\cos(\omega t) + \sin(\nu j)\sin(\omega t)] \tag{3.4}$$

which, using standard trigonometric identities, becomes:

$$x_j(t) = A\ \cos(\nu j - \omega t) = A\ \cos[\nu(j - ct)] \tag{3.5}$$

with $c = \omega/\nu$. We thus come to the conclusion that the superposition we are considering yields a travelling wave, consisting of a spatial modulation of the amplitude A indexed by j–which we can identify as the position along the chain–and shifting in time according to the value of c, in turn defining the wave velocity.

Besides movement, a key future for phonons is localization. Since the normal modes represent collective excitations of the system, they are completely delocalized along the whole chain. A visual representation of the first few normal modes for the monoatomic linear chain, when both ends are kept fixed, is provided in Figure 3.1a.

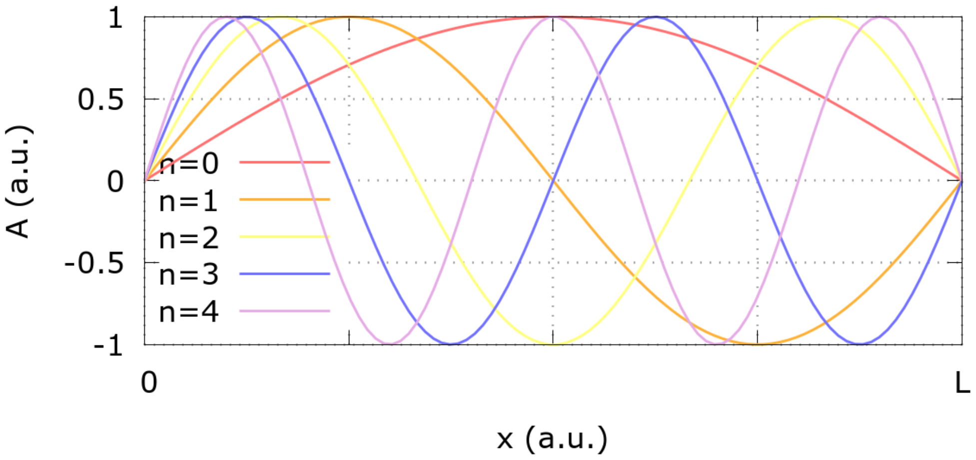

(a) normal modes

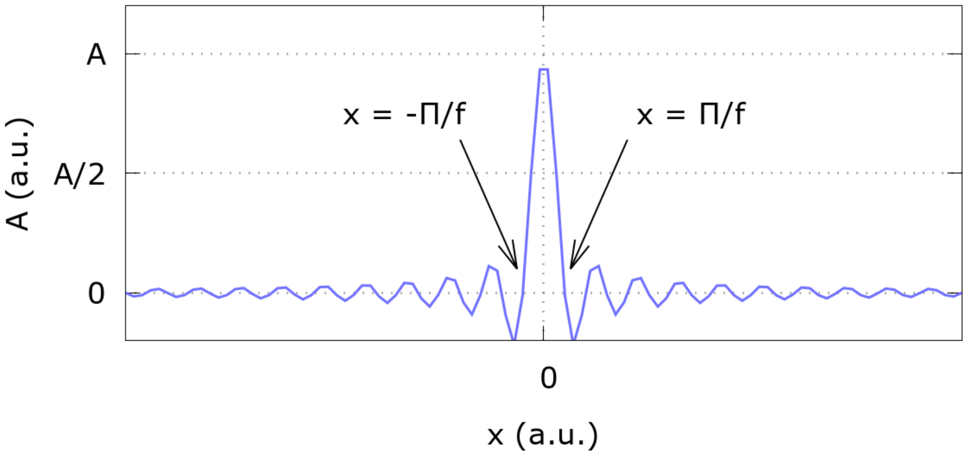

(b) wavepacket

Figure 3.1: (a) First five normal modes of an elastic string fixed at both ends, with normalized amplitudes. The mode number is linked to the number of nodes–i.e. the stable points of the vibrating string. (b) Localized wavepacket resulting from an even superposition of normal modes within a frequency window of witdh $2f$. The amplitude is significatively different from zero only within a range $2\pi/f$, marked by the two black arrows.

Superposition also allows the formation of localized waves, that travel and evolve according to the very same equations of motion. These localized waves result from the superposition of a large number of plane waves within a relatively narrow frequency window, say $[-f, f]$–from which the name 'wave packet'. If we take a bunch of normal modes, all interferring constructively at some fixed point p, and superpose them, the waves will exhibit destructive interference as soon as we move away from p. So, the resulting amplitude will be qualitatively different from zero only within a length $2\pi/f$. This is better illustrated by considering the continuum case, where we have set $x(p) = 0$ for convenience:

$$\frac{1}{2f}\int_{[-f,f]} dk \; A\cos{(kx)} = A\,\frac{\sin{(fx)}}{fx} \tag{3.6}$$

A visual representation of this wavepacket is provided by Figure 3.1b.

Before proceeding to the multi-atomic case, it is noteworthy to consider the low-n sector of the normal modes. Using the approximation $\sin{(x)} \approx x$ whenever $x \to 0$, we get the following dispersion relation from Equation 3.1, for $n/N \to 0$:

$$\omega(n) \approx \omega_0\,\frac{2\pi|n|}{N} \tag{3.7}$$

so, we come to the conclusion that the ratio between $\omega(n)$ and $|n|$ is constant for low values of n/N, resulting in all low-n normal modes travelling with the same velocity, as described in Equation 3.5. For this reason, wavepackets and other waveforms resulting from the superposition of low-n modes shift rigidly, i.e., maintaining their shape exactly, as the system evolves in time. This is a crucial feature, as these nondispersive waves usually contribute the most to thermal transport, even in complex materials, as we will see next.

One last comment has to do with the continuum limit of the theory discussed above, meaning that we allow the lattice spacing to go to zero and the number of atoms in the chain to become infinite. Since we are interested in a string with well-defined global length L, elastic constant k_{macro}, and mass M, we need to regularize the values of the lattice spacing a, atomic masses, and interactions in such a way the macroscopic quantities characterizing the string remain fixed. This is achieved setting:

$$\begin{aligned} m(N) &= M/N \\ a(N) &= L/N \\ k_{el}(N) &= k_{macro} \times N \end{aligned} \tag{3.8}$$

which, plugged into Equation 3.7–and recalling that $\omega_0 = \sqrt{k_{el}/m}$–gives:

$$\omega(n) \approx \sqrt{N^2 \, \frac{k_{macro}}{M}} \, \frac{2\pi|n|}{N} = 2\pi|n|\sqrt{\frac{k_{macro}}{M}} \tag{3.9}$$

showing that the dependency on N cancels out as expected. Since N goes to infinity, the approximation of Equation 3.7 becomes an exact identity, and the linear dispersion relation holds for all modes. Still, it is rather convenient to express everything in terms of intensive variables, as we may want to allow the length of the string to reach infinity, maintaining a well-defined mass density $\rho = M/L$ and bulk modulus $b = k_{macro} \times L$. We get the following.

$$\omega(n) = \frac{2\pi|n|}{L}\sqrt{\frac{b}{\rho}} \tag{3.10}$$

in which the wavelength of the mode $\lambda_n = L/|n|$ and the sound velocity $c = \sqrt{b/\rho}$ appear explicitly. It is customary to label the value $2\pi/\lambda_n$ by k_n, which is called the "wave-vector" of the corresponding mode. Altogether, the index j gets multiplied by the lattice parameter a and becomes a continuous variable, usually denoted by x, representing the position along the string, whereas the displacement of the j-th atom $x_j(t)$ becomes a function of both the position along the string and time, and is usually denoted by $\varphi(x,t)$. The resulting equation of motion for this scalar field is the massless wave equation, namely:

$$\left({\partial_{ct}}^2 - {\partial_x}^2\right) \varphi(x,t) = 0 \tag{3.11}$$

Of course, when $L \to \infty$, k becomes a continuous variable, also, allowing us to suppress the discrete index n and put the dispersion relation in its final form:

$$\omega(k) = c|k| \tag{3.12}$$

The massless wave equation, and the corresponding dispersion relation, force the result into being a function of the variable $x \pm ct$ alone, and not separately depending on x and t. This makes the evolution of the resulting wave rather simple, as the function shape is conserved as time elapses, the only change in the system being the rigid shift of the wave envelope towards the travel direction. For this reason, these special solutions are known as nondispersive waves. Since we are interested in transport properties, and the energy is stored in the elastic deformation of the material, it is clear that non-dispersive waves, and especially non-dispersive wavepackets, are utterly important, as they allow a thoroughly efficient means of transporting energy along a given direction. Since the normal modes associated to the massless wave equation are also responsible for the audible sound of everyday life, they take the name of acoustic modes.

3.1.2 Multi-atomic linear chain

When the primitive cell of the crystal lattice does no longer contain one atom only, the dynamics of the entire system enriches considerably. This is due to translation symmetry applying to the full primitive cell and its local set of degrees of freedom–corresponding to the different vibration patterns of the cell alone. So, every independent primitive-cell vibration pattern gets endowed with a full set of possible k values as well, in turn describing the modulation of the amplitude of that specific normal mode, as we move to other cells. Each one of this modes will still be characterized by its specific vibration frequency, but the relation between the temporal and spatial frequency will, in general, be very different from the monoatomic lattice case. This fact has serious consequences on the way these modes propagate, because the velocity of each normal mode will, in general, be different from that of the other modes. For this reason, if we start from a given initial shape of our multi-atomic chain and let time flow, the shape will not be preserved, and the energy stored into the elastic deformation will usually spread to more and more extended areas of the chain, inhibiting transport properties to a great extent. These modes, in turn, have non-zero energy–and frequency–at zero k. For this reason, they can't be excited by arbitrary small amounts of energy in a continuous fashion, and as such, when they decay by emitting energy in the form of photons, reason why they go under the name of optical modes. Along with the optical modes, which correspond to non-trivial vibration patterns of the primitive cell, modulated across the material, there are always the acoustic modes–three in total, for a $3-\mathrm{D}$ lattice, in which the whole primitive cell simply undergoes shear or compression, but the relative positions of the atoms inside of it remain unchanged. The phonon spectrum for the diatomic linear chain, showing both acoustic and optical modes, is provided in Figure 3.2. Note that the optical branch is nearly flat when the two atomic masses differ considerably from each other, making the corresponding modes non-propagating almost at all. This further strengthens the evidence that acoustic modes account for most of the thermal conductivity of a given material. The analytic expression for both branches of the diatomic spectrum, when there is only one elastic constant, is given in Equation 3.13:

$$\omega_{\pm}{}^2(n) \ = \ \omega_0{}^2 \left(1 \pm \sqrt{1 - \frac{2r}{1+r}\sin^2\left(\pi n/N\right)}\right) \tag{3.13}$$

where ${\omega_0}^2 = k_{el}(\frac{1}{m} + \frac{1}{M})$, $r = 2mM/(m^2 + M^2)$, and m and M are the two atomic masses. A step-by-step derivation of the result goes beyond the scope of the present thesis [58].

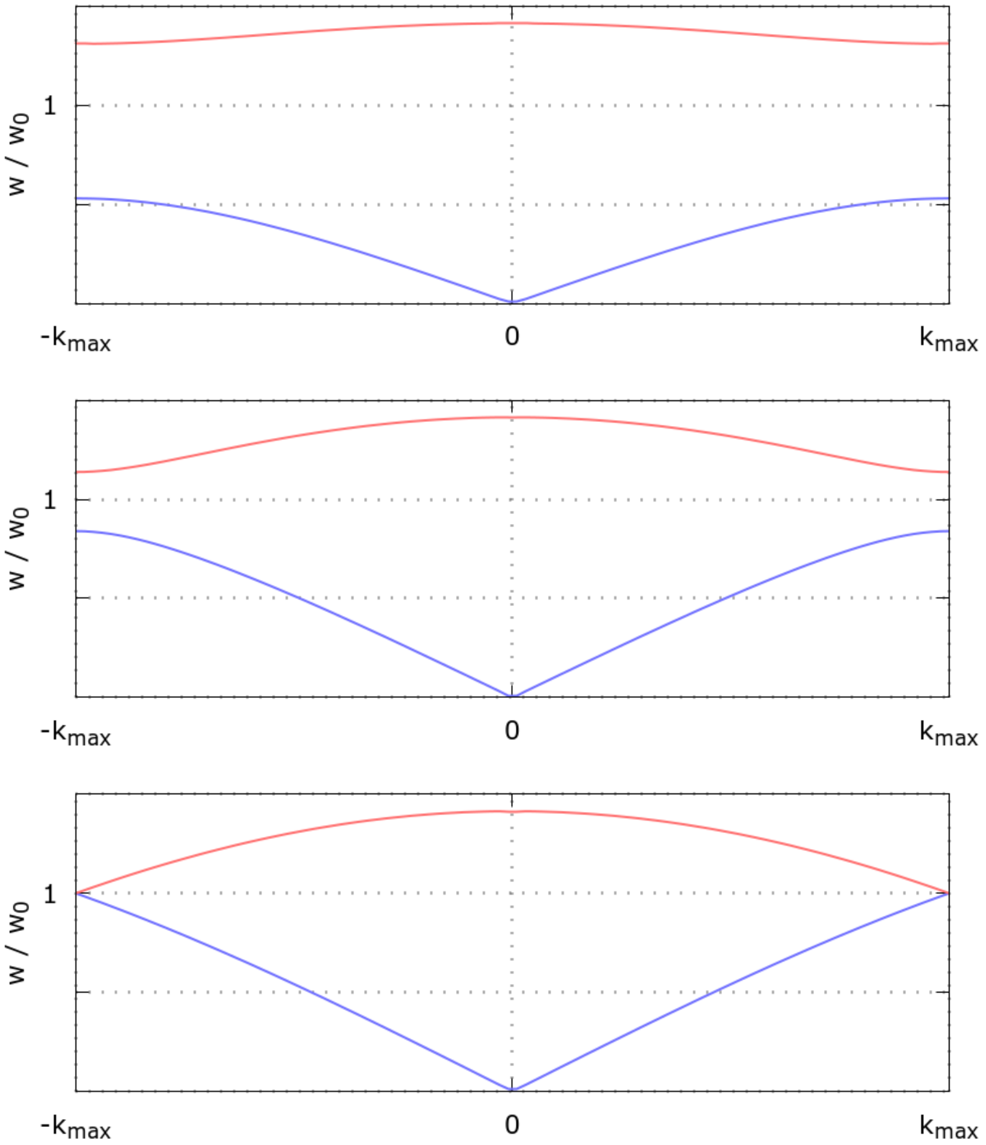

Figure 3.2: The diatomic lattice spectrum, exhibiting both acoustic and optical modes–depicted in blue and red respectively–for r equal to 0.32, 0.84, and 1 (top-down). In the last case we get back to the monoatomic lattice, and band-folding takes place. This corresponds to the acoustic branch folding on itself, as the Brillouin zone of the resulting lattice would be two times bigger, but we are forcing it not to exceed k_{max}.

3.1.3 Superlattices

Having probed into both the monoatomic and multiatomic linear chain properties, and having elucidated the remarkable differences between acoustic and optical modes, we can turn to the analysis of the superlattice case. To better tackle the question, we will start by the simplest possible non-trivial superlattice, namely a linear superlattice containing two atomic species only, an even number of which lodges inside the two halves of the primitive superlattice cell respectively. This situation in schematically depicted in Figure 3.3.

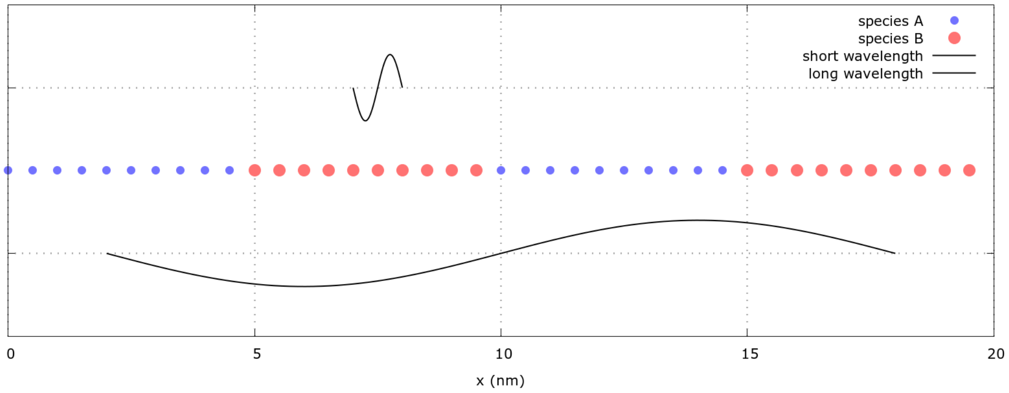

Figure 3.3: Diatomic superlattice of materials A and B, with short and long wavelength snippets plotted for comparison. The superlattice period is 10 nm.

For convenience, we consider a superlattice containing a large number of atoms inside the primitive cell, in such a way the superlattice period becomes much greater than the interaction length. When this happens, inside each half of the primitive cell the material and its properties become indistinguishable from those of the corresponding constituent materials. That is, when the superlattice period is long enough, in comparison to the period of the lattices of the two underlying materials, we can consider excitations localized inside a region much smaller than the primitive cell of the superlattice itself, and the behavior of these excitations will be exactly the same we would have in the corresponding constituent material alone, as long as we are far away from the half-cell boundaries. Plus, it will experience both transmission and reflection each time it hits the interface with the other material. For this reason, when we consider short-wavelength phonons inside the superlattice, their dynamics can be rationalized thinking of them as facing a linear array of interfaces, delimiting the transitions between the consecutive layers of the two materials. These short-wavelength phonons thus get highly scattered, in turn contributing very little to coherent transport processes. However, when the characteristic wavelength of the excitation we are considering approaches the same order of magnitude of the superlattice period, the situations changes considerably. Long wavelength excitations comprise many superlattice periods at once, in turn making them experience a single metamaterial with its own properties, rather than a linear array alternating between materials A and B. This averaging effect of the properties of the constituent materials into those of a single metamaterial becomes more and more efficient as the wavelength increases. For this reason, it is reasonable expecting long-wavelength excitations to better propagate and transport heat through the superlattice in comparison to short-wavelength ones–keeping in mind that long VS short depends on the ratio with the superlattice period.

3.1.4 Effects of Temperature

As we have discussed in Chapter 2.3.2, temperature regulates the phonon population of each normal mode according to the Bose-Einstein statistics. Since different normal modes correspond to different values of the corresponding zero-point energies, the phonon population of the various modes, each one with its characteristic frequency and wavelength, will, in general, be very different from each other. This effect, combined with the previous considerations on the propagation properties of short and long wavelength phonons through the superlattice, makes clear that the thermal conductivity of the material will be, in general, a nontrivial function of temperature. Different wavelengths propagate differently inside the superlattice indeed, and the number of phonons in each mode determines how many phonons from that normal mode and wavelength are contributing to thermal transport. This is further clarified considering the following example. If the temperature approaches the absolute zero, the population of almost every normal mode is zero as well, and the thermal conductivity results from the contribution of a few numbers of modes at most–typically, the modes with the longest wavelengths, which are the better propagating ones inside the superlattice. As temperature gradually increases, more and more modes get be populated, and start contributing to thermal transport, so the thermal conductivity will gradually increase as well. Nevertheless, when the temperature increases further, optical modes will start to be populated as well, but, because they are poorly propagating and increasing temperature also enhances the interactions and phonon scattering, the thermal conductivity will start to decrease. MD simulations use the classical equation of motions for the atoms, and for this reason they do not provide a working description at low temperatures, where quantum effects become dominant. For this reason, typical MD simulations are not capable of capturing the initial increase in the thermal conductivity as the temperature moves away from the absolute zero. Nevertheless, they work pretty well at high temperature, where the Bose-Einstein statistics functions like the Maxwell-Boltzmann one. For this reason, it is possible to appreciate the decay in thermal conductivity whenever temperature increases. Along with the variation of temperature, we can ask ourselves what happens when we keep the temperature fixed and let the superlattice period vary instead. According to the analysis we carried out so far, it should be clear that tuning this degree of freedom can provide great modification in the behavior of the physical system and its thermal transport properties. In this istance, the situation is particularly interesting, since we can fully probe into it with the MD simulations. This matter is discussed in detail in the next section, as we move to the computational characterization of the Si/Ge superlattice.

3.2 The Si/Ge superlattice

Silicon (Si) is the second most abundant element in the Earth's crust, primarily found in forms such as sand, quartz, and various minerals. It plays a crucial role in the field of electronics as the most widely used material for semiconductors. The key reason for its dominance is its optimal balance of electrical conductivity and the ability to be doped with impurities to modify its properties for specific applications. Silicon's band gap is approximately 1.1 eV, making it suitable for devices operating at room temperature, as this band gap allows controlled conduction when energy is applied. Furthermore, Silicon widespread availability and low cost contribute to its use in mass production, while its mechanical stability and high-temperature resistance enhance its durability in electronic devices. Common applications of Silicon include integrated circuits (ICs) for processors, memory chips, transistors, and photovoltaic cells used in solar panels, making it the foundational element of modern electronics and energy conversion technologies.

Germanium, although less abundant than Silicon, was historically the first material used in semiconductor technology. Extracted from zinc ores and coal deposits, Germanium is more costly but offers certain advantages in electronic applications. Its electron mobility is higher than that of Silicon, which enables faster switching in electronic circuits, an important property for high-performance devices. Germanium has a smaller band gap of 0.66 eV, making it more sensitive to temperature fluctuations but valuable in low-voltage and high-frequency environments. It also plays a significant role in optoelectronics, particularly in infrared detectors and fiber optic systems, due to its transparency to infrared light. In modern semiconductor technology, Si/Ge alloys are frequently used for enhancing performance in high-speed transistors and RF circuits, indicating Germanium's continued relevance in specialized areas of electronics and communication technologies. So, while effective as standalone semiconductor materials, they can be combined into alloys, and the fusion of these elements takes advantage of both Silicon's stability and cost-effectiveness, and Germanium's superior electron mobility and optoelectronic properties. This synergy has led to the development of advanced semiconductor blends like Si/Ge superlattices as well, which exploit the matching geometric characteristics of each element to achieve highly ordered structures which remain stable way above RT. Such highly-ordered nanostructures gained particular audit in the last decade. A cartoon representing the SiGe superlattice is provided in Figure 3.4.

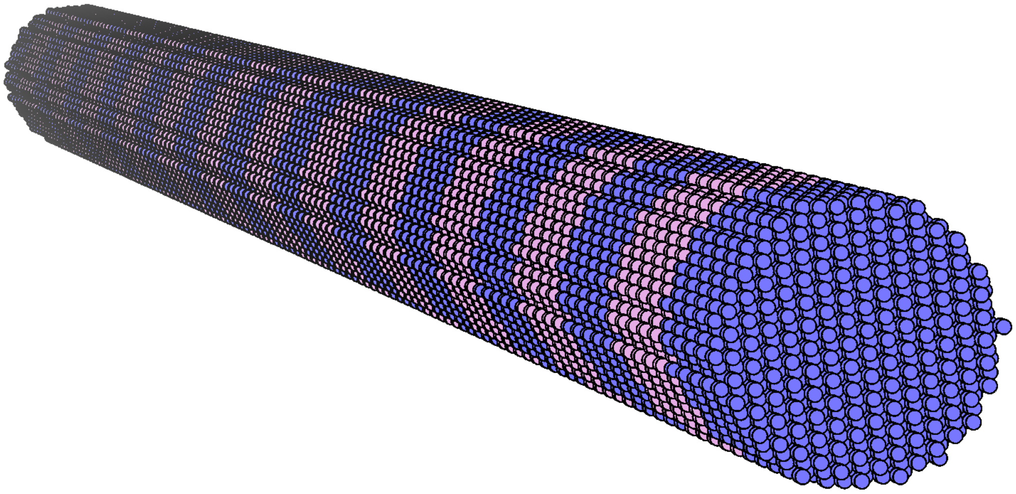

Figure 3.4: SiGe [111] superlattice nanowire, showcasing a period of 9.6 nm and 20 nm^2 hexagonal cross section. Silicon atoms are depicted in blue, while Germanium atoms have been colored according to the palette of Chapter 2.

These superlattices are critical in pushing the boundaries of high-speed electronics and optoelectronics, where traditional materials face severe limitations [59]. Plus, they represent a groundbreaking advancement in semiconductor technology, involving the periodic stacking of ultra-thin layers of Silicon and Germanium. This layer-by-layer arrangement creates a unique structure with enhanced electronic and optical properties that neither element alone can achieve [60]. In a superlattice, the alternating layers of Silicon and Germanium form heterojunctions, which alter the electronic band structure and enable better control over carrier mobility, thermal conductivity, and electron confinement [61]. One of the key advantages of Si/Ge superlattices is their ability to tailor the band gap. By adjusting the composition and thickness of the Silicon and Ge layers, researchers can engineer the band gap to optimize the material for specific applications. This tunability makes SiGe superlattices highly desirable for high-performance transistors, high-frequency devices, and infrared photodetectors. These properties also make them ideal for use in heterojunction bipolar transistors (HBTs), where enhanced electron mobility and high current densities are crucial for fast switching and improved power efficiency [61]. Moreover, the strain engineering introduced by SiGe superlattices offers further benefits. As Ge has a larger atomic radius than Silicon, growing layers of Ge on Silicon creates a strain within the lattice structure [59]. This strain alters the electronic properties of the material, leading to enhanced carrier mobility and improved device performance, particularly in high-speed and low-power applications. Strained SiGe superlattices are particularly relevant in complementary metal-oxide-semiconductor (CMOS) technology, where they enable faster operation while minimizing power consumption [60]. In addition to their electronic applications, SiGe superlattices are also important in thermoelectric materials. The layered structure can significantly reduce thermal conductivity while maintaining high electrical conductivity, enhancing the thermoelectric efficiency of devices, which in turn reflects in the matter of this study. This has implications for power generation and energy harvesting applications, where SiGe superlattices can be used to convert waste heat into electrical energy with improved efficiency [61]. In the following sections, we investigate the thermal transport properties of SiGe superlattices with atomically flat and also chemically imperfect interfaces, focusing on both bulk superlattices and superlattice nanowires. Using NEMD simulations and almaBTE software, we study phonon transport along different crystal directions, exploring the dependence of thermal conductivity on the superlattice period and the average temperature of the system. Moreover, we will take the chance to touch on the theoretical aspects of the BTE, which best accounts for the present understanding and description of transport phenomena at the particle level, also stressing the relation to Fourier's Law, and outlining some useful approximations, like the Relaxation Time Approximation (RTA), that we use in our study.

3.2.1 Set-up of the simulations

We employ two techniques to evaluate thermal transport in SiGe superlattices: NEMD and the BTE, implemented by the almaBTE code. For NEMD simulations, the LAMMPS code is again used to model superlattices with alternating layers of Silicon and Ge, maintaining atomically flat interfaces. The whole NEMD methodology–simulation time and timestep, thermostatting technique, achieving the NESS, averagings, estimates of the thermal conductivity, and so on–is identical to the GaAs/Ge heterojunction one, the only difference being the hexagonal cross section build for the nanowire. This is simply obtained by eliminating all the atoms lying outside a cylinder having the desired diameter after the unit-cell stacking routine. The transformation of the blank lattice nanowire into a superlattice nanowire hides some subtleties instead, that we discuss in detail later on in this chapter.

The systems studied include bulk superlattices and nanowire superlattices, with transport directions along the [001] and [111] crystallographic axes. The periodic boundary conditions are applied in directions perpendicular to the transport axis for the bulk cases, whereas open boundary conditions are used along the transport direction.

In both bulk and nanowire configurations, the interaction between Silicon and Ge is modeled using the Tersoff potential included in the LAMMPS distribution. The initial structures are relaxed at constant volume, and atom velocities are initialized according to the Maxwell-Boltzmann distribution at 300 K. A temperature bias of 100 K imposed at the ends of the system creates a steady-state heat flux within about one nanosecond, and we continue to simulate up to about 7 ns, thus allowing us to extract phonon transport properties by averaging data belonging to the steady-state window.

To complement the NEMD results, we use almaBTE software, which computes thermal conductivity using inputs derived solely from first-principles calculations based on DFT [62]. AlmaBTE allows us to compute the thermal conductivity along the preferred axis ensuring that no empirical fitting parameters are used, but in practice it is limited to bulk superlattices only, as it relies on force constants that must be computed through DFT if we want to circumvent the usage of effective interatomic potentials from MD, which are often available for bulk systems only. This approach provides a robust prediction of thermal conductivity as a function of the superlattice period and temperature for bulk geometries.

3.2.2 Si/Ge superlattice nanowire

To generate the superlattice structure for the NEMD simulations, we start from a blank lattice of a ZB nanowire extending along the z-axis, with assigned 0.554 nm period, 5 nm diameter and 120 nm length. The z-axis corresponds to the [001] or [111] crystallographic directions. The chemical species are then assigned according to the z-coordinate modulo the target superlattice period, here denoted as Λ. Specifically, Silicon atoms are placed in the first half of each superlattice cell, and Germanium atoms occupy the second half. We named this approach “Tailoring” the SL, as it effectively mimics the alternating layers of Si and Ge, establishing a periodic structure along the nanowire. A close inspection at the procedure just described, reveals that it can be used to give rise to three nonequivalent superlattice classes without changing the crystallographic orientation, showcasing remarkably different transport properties. While there is only one possible interfacial configuration for the [001] case, two distinct [111] atomically flat interfacial configurations can be created between these materials indeed. In the first configuration, the Si and Ge atoms at the interface are perfectly aligned. In this configuration, each Si atom chiefly bounds to one Ge atom only. In the second configuration, the atoms are staggered, leading to the actual interaction of every Si atom with three Ge atoms at once. This difference in atomic arrangement gives rise to much stronger coupling, compared to the aligned case, resulting in two distinct types of interfacial TBRs for the two interfacial configurations. The schematics of the two interfaces is depicted in Figure 3.5a

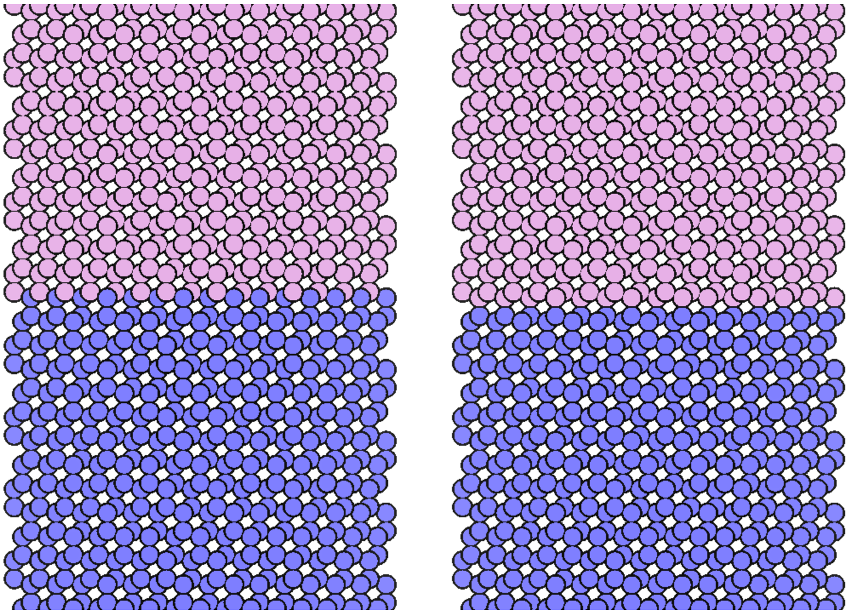

(a) interface structure

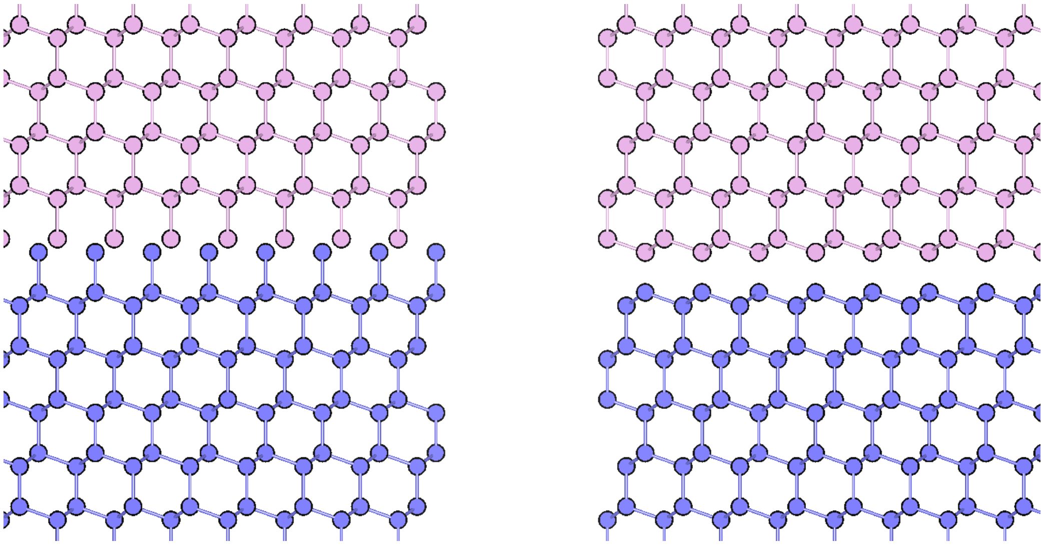

(b) zoom on the interface region

Figure 3.5: Comparison between tight and loose interfaces, left and right respectively. In (b) the reader can appreciate the difference between the chemical bonds connecting Si and Ge at the interface in the two cases.

To take these differences into account, we studied two batches of Si/Ge superlattice nanowires totalling 12 simulations, each batch corresponding to one of the interfacial configurations where the SL period ranges evenly from 1.9 to 11.5 nm. 2 more simulations were also performed to compute the standalone TBR for both interface types, and provided us with a crucial cross-check for interpreting the dependence of κ on the SL period in the two cases. Our results in Figure 3.5b show that the staggered interfaces exhibit a significantly lower TBR, enhancing thermal conductivity compared to the aligned interfaces. The numerical values of the TBR for both configurations are provided in Table 5.8. Our findings also corroborate previous studies that emphasize the critical role of the interface structure in determining the transport properties of superlattices [63–65].

One more "imperfect superlattice" class is obtained when the period Λ, chosen for tailoring the SL structure, is not an exact multiple of the underlying blank lattice parameter, and a subtle but significant periodicity break occurs. Although the structure visually resembles a true superlattice, the atomic arrangement no longer exhibits perfect translational symmetry indeed. This minor distortion profoundly affects the transport properties of the system, particularly phonon transport [66]. To tackle into this nonideality, we performed 12 different simulations, for values of the period used to tailor the chemical structure on the geometrical one ranging evenly from 1 to 12 nm.

In true superlattices, as we have seen, phonon coherence—arising from the constructive interference of phonon wavepackets—plays a critical role in thermal transport. However, in systems where periodicity is broken, even subtly, phonon coherence is suppressed. As a result, the transport behavior resembles that of random or amorphous systems characterized by diffusive phonon transport rather than coherent transport. These findings, matching our simulations, suggest that precise control over the periodicity of the superlattice is crucial for harnessing its full potential in thermal applications, seemingly in contrast with experimental results, although we cannot perform simulations of real-size systems yet.

Nevertheless, thermal transport in semiconductor superlattice nanowires exhibits unique characteristics driven by phonon coherence effects, which can be appreciated within our current computational capabilities. In accordance with the previous analysis, at small superlattice periods phonons maintain coherence, traveling in well-defined wave modes across the material, which contributes to enhanced thermal conductivity. As the superlattice period increases, phonon coherence gradually diminishes, leading to a shift from coherent to diffusive thermal transport. This transition is particularly evident in the temperature profile, where a “ladder” structure appears, indicative of the transition from coherent-to-incoherent transport regimes. Such a transition is attributed to the increased phonon scattering at interfaces and the relaxation of phonon wave phases, which effectively localizes phonon propagation, facilitating the diffusive regime [67]. This behavior matches our simulations, as we display in Figure 3.6 where a batch of temperature profiles along the nanowire for increasing superlattice periods for the [111]-tight configuration is provided, where the reader can appreciate the coherent-to-incoherent transition.

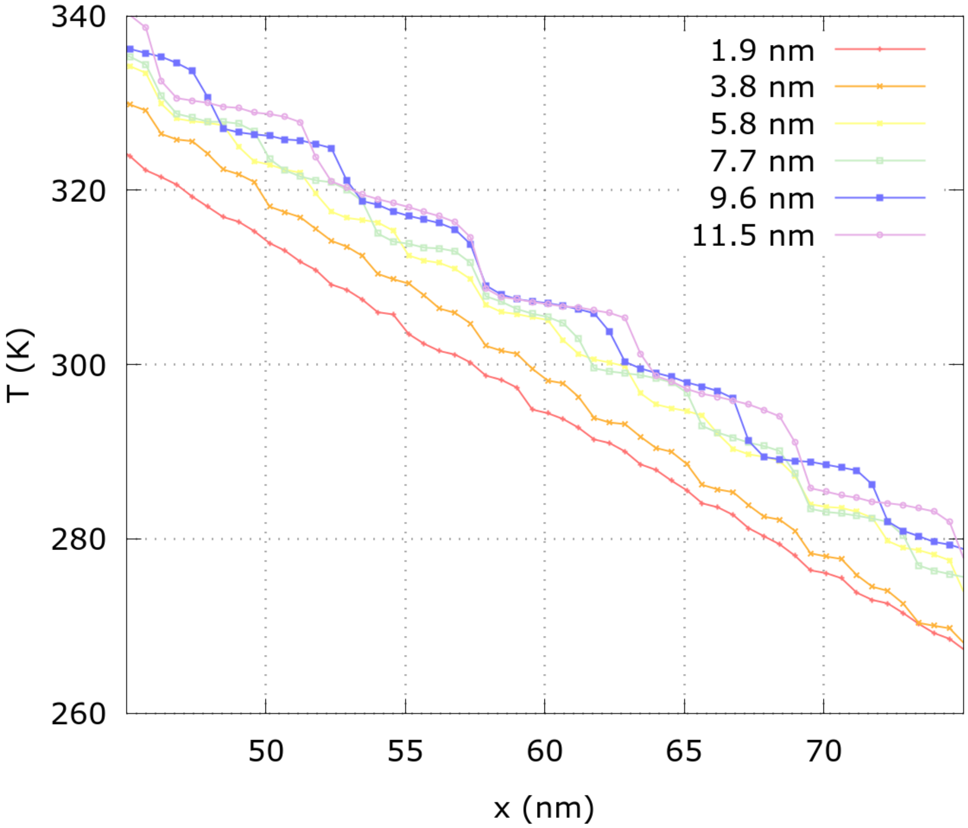

Figure 3.6: temperature profile of the [111] superlattice nanowire for different values of the superlattice period

In nanostructured materials, this transition from coherent to incoherent phonon transport provides an essential mechanism for tailoring thermal conductivity for thermoelectric applications. Control over the superlattice period is thus a significant design factor, allowing optimization of phonon mean free paths and thermal transport properties for improved efficiency [68, 69]. The emergence of a ladder structure from our simulations represents a valid indicator that our setup proved capable of capturing the relevant underlying Physics, at least in a descriptive fashion, while question around the predictive power and the range of applicability of the methods involved remains broadly open. To complement the analysis, we also studied the dependence of κ on the SL period for the [100] transport direction totaling 8 more simulations, with a slightly denser sampling at short periods, where the coherent-to-incoherent transition is expected to take place.

The results of our analysis show good agreement with both theory and experiments. We find κ to be a non-trivial function of the SL period and temperature, which exhibits a minimum at around 4 nm for both orientations, and then increases, showing the linear dependence on the interface density, a recurrent countermark that the diffusive regime has been reached. Plus, κ in the tight interface configuration develops values about 20 % higher than the loose interface ones, reflecting the different values of the TBR resulting from our previous simulations. Contrary to them, the free period configuration does not show any minimum, as the lack of translational symmetry completely alters the phonon picture, impeding any coherence to arise.

These findings are schematically depicted in Figure 3.7b. The [100] transport direction results are provided in Figure 3.8. The numerical data are available in Tables 5.9, 5.10, and 5.11.

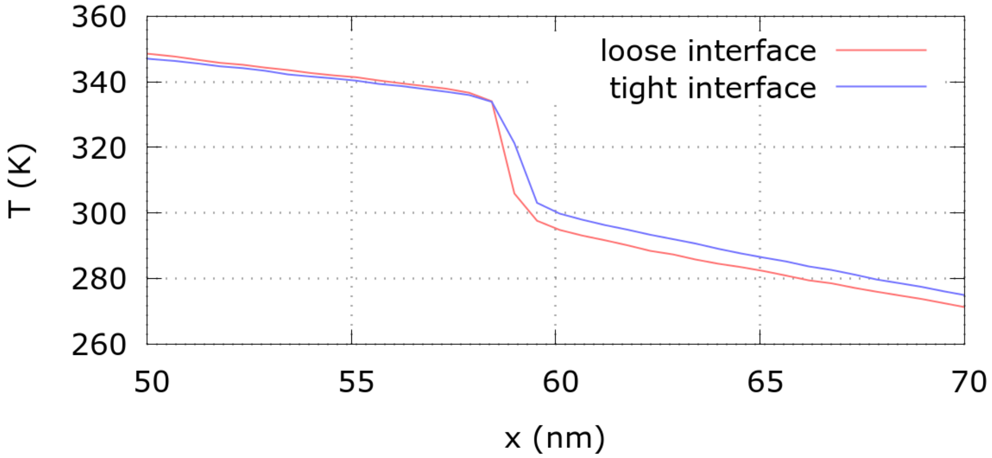

(a) temperature profiles

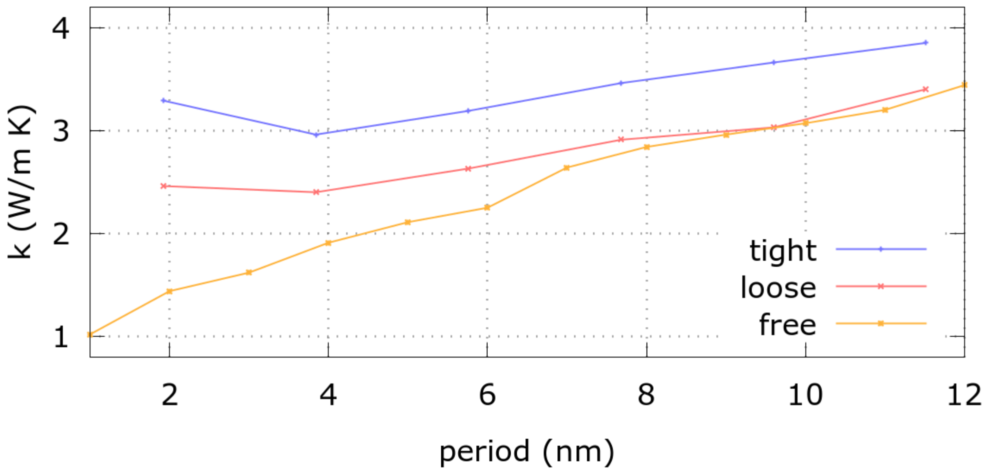

(b) κ

Figure 3.7: (a) temperature profiles of the [111] loose and tight interfaces - focus on the interface region, where the reader can appreciate the greater temperature drop for the loose interface and (b) thermal conductivity as a function of the superlattice period for the tight, loose, and free interfaces

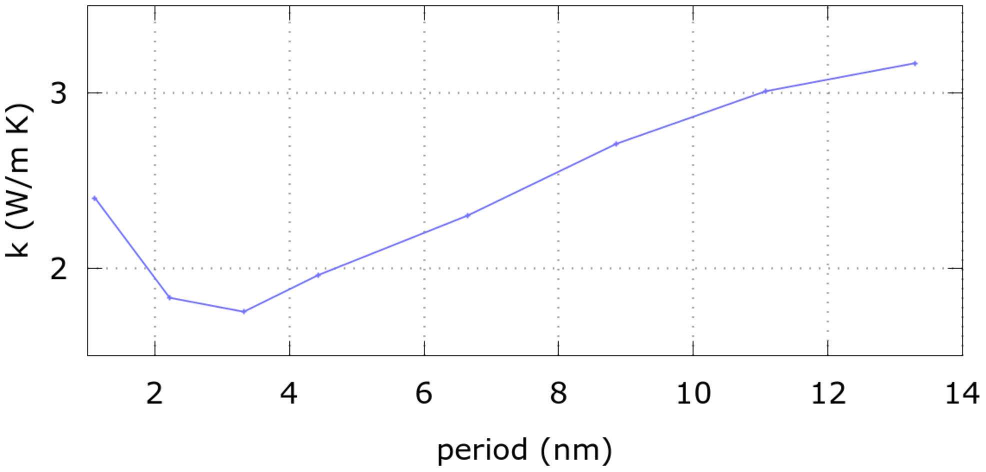

Figure 3.8: thermal conductivity of the [100] superlattice nanowire as a function of the superlattice period

3.2.3 Si/Ge bulk superlattice

We now continue our study by presenting the analysis of the bulk superlattice case. Bulk superlattices exhibit distinct characteristics compared to superlattice nanowires, that affect phonon behavior and thermal conductivity. This chiefly happens because superlattice nanowires are reduced-dimensional structures, and boundary scattering is more pronounced due to their near to 1-D geometry, leading to altered phonon dispersion relations.

The key difference between these two structures lies in the influence of boundary scattering. In superlattice nanowires, the near to 1-D geometry leads to significant contributions from boundary scattering, which play a critical role in the phonon thermal transport. The presence of boundary scattering in SLNWs results in reduced thermal conductivity compared to bulk SLs, as confirmed by our simulations. So, while both bulk superlattices and superlattice nanowires exhibit unique phonon modes and scattering mechanisms, boundary scattering in nanowires is particularly important for determining the actual thermal transport properties at the nanoscale.

To tackle bulk SL, we employed both LAMMPS and almaBTE. The second software relies on the Boltzmann Transport Equation and allows using DFT-only input quantities. DFT is going to be discussed at length in the next chapter, where it is used extensively to deal with electro-optical properties of the nanostructured semiconductor materials we are dealing with. For this reason, here we limit ourselves to a minor introduction. In short, Density Functional Theory (DFT) is a modeling method derived with first-principles QM, used to investigate the electronic structure of many-body systems. It is based on the assumption that the properties of a system can be determined by the electron density–which is often the case, and has become a standard tool in computational materials science for its ability to accurately predict a wide range of material properties, including electronic, optical, and thermodynamic properties, with a relatively low computational cost compared to other quantum mechanical methods. In the context of phonon thermal transport, DFT provides the necessary information about the material's electronic structure and the resulting ionic pseudopotentials, which are then crucial for calculating the interatomic interactions and phonon dispersion relations.

AlmaBTE (Ab Initio Phonon Boltzmann Transport Equation) is a computational framework designed to calculate thermal conductivity using input quantities derived from DFT. AlmaBTE solves the phonon Boltzmann transport equation by integrating the phonon scattering processes, such as phonon-phonon and phonon-boundary scattering, which are essential for predicting thermal transport properties at the nanoscale.

Boltzmann Transport Equation

The Boltzmann Transport Equation (BTE) is a central tool in understanding thermal transport at the nanoscale. Its grasp is way stronger than Fourier's Law, which can be regarded as an effective, mesoscopic model, and it describes the evolution of the distribution function of phonons (in our case) under the influence of by various scattering processes, such as phonon-phonon interactions, impurity scattering, and boundary scattering. In the context of thermal conductivity, the BTE provides a framework for modeling transport under non-equilibrium conditions, allowing for the prediction of thermal conductivity in a broad class of materials [70, 71].

The starting point for deriving the BTE for phonons is the classical Boltzmann equation, which describes the time evolution of the distribution function $f(\mathbf{r}, \mathbf{v}, t)$ of phonons in phase space, where $\mathbf{r}$ is the position, $\mathbf{v}$ is the phonon velocity, and t is time. We will not provide any derivation of this equation, but it is worth mentioning that the classical BTE follows from the quantum BTE, which in turn can be derived exactly from relativistic Quantum Field Theory, so it should never be regarded as an “effective” theory, but rather as a fundamental one [72]. The BTE for phonons can be written as:

$$\frac{\partial f(\mathbf{r},\mathbf{v},t)}{\partial t} + \mathbf{v}\cdot\nabla f(\mathbf{r},\mathbf{v},t) = \left(\frac{\partial f}{\partial t}\right)_{\text{scat}} \tag{3.14}$$

where the left-hand side describes the free-streaming of phonons, and the right-hand side represents the scattering term, which accounts for the changes in the phonon distribution due to scattering events. The scattering term is given by:

$$\left(\frac{\partial f}{\partial t}\right)_{\text{scat}} = \int\int\int \left(\frac{\partial f}{\partial t}\right)_{\text{scat}} (\mathbf{v},\mathbf{v}',\mathbf{k},\mathbf{k}')d\mathbf{k}'d\mathbf{v}'d\Omega \tag{3.15}$$

where the integration is over the final and initial wavevectors $\mathbf{k}$ and $\mathbf{k}'$, and the final and initial velocities $\mathbf{v}$ and $\mathbf{v}'$. The scattering term can be derived using various scattering mechanisms, such as three-phonon scattering (phonon-phonon interactions) or boundary scattering in nanostructured materials. To proceed with solving the BTE, one typically makes the assumption of a steady-state condition, where the time derivative of the distribution function is zero. This simplification leads to the steady-state BTE:

$$\mathbf{v}\cdot\nabla f(\mathbf{r},\mathbf{v}) = \left(\frac{\partial f}{\partial t}\right)_{\text{scat}}. \tag{3.16}$$

This equation is central to determining the phonon distribution in a system. Once the distribution function is known, it can be used to calculate the heat flux $\mathbf{Q}$, which is related to the thermal conductivity κ through Fourier’s Law. The thermal conductivity κ is obtained by solving the BTE and calculating the phonon relaxation times τ, which depend on the scattering rates for different types of scattering events. The solution to the BTE requires knowledge of the scattering mechanisms present in the material. These include three-phonon processes (Umklapp and normal scattering), being the dominant mechanisms that contribute to the scattering of phonons at high temperatures, the increased surface-to-volume ratio leading to significant contributions from boundary scattering in nanostructured materials, which can reduce the effective thermal conductivity [73], and the presence of impurities and defects in a material, further complicating phonon transport and serving as scattering centers that limit the MFP [74].

In modern computational tools such as AlmaBTE, the BTE is solved using first-principles calculations, where input quantities like interatomic force constants and phonon dispersion relations are obtained from Density Functional Theory (DFT). AlmaBTE computes the scattering rates and solves the BTE to predict the thermal conductivity by integrating over all possible phonon scattering processes. This approach enables the prediction of thermal conductivity in both bulk and nanostructured materials, providing insights into how different scattering mechanisms influence the heat transport at the nanoscale [75]. So, by leveraging DFT-calculated interatomic force constants and phonon dispersion, AlmaBTE provides detailed insights into the phonon scattering mechanisms that govern thermal conductivity in materials. This approach has proven effective in studying a wide variety of materials, from bulk semiconductors to nanostructured systems.

RTA vs full BTE

In contrast, the Relaxation Time Approximation (RTA) simplifies the full BTE by assuming that the phonon distribution function relaxes to an equilibrium distribution function over a characteristic relaxation time τ. This approximation reduces the scattering term to a simple linear function of the deviation from equilibrium, making the equation much easier to solve. The RTA for phonon transport can be expressed as:

$$\frac{\partial f(\mathbf{r},\mathbf{v})}{\partial t} + \mathbf{v} \cdot \nabla f(\mathbf{r},\mathbf{v}) = -\frac{f(\mathbf{r},\mathbf{v}) - f_{\text{eq}}(\mathbf{v})}{\tau(\mathbf{v})}, \tag{3.17}$$

where $f_{\text{eq}}(\mathbf{v})$ is the equilibrium distribution function, and $\tau(\mathbf{v})$ is the phonon relaxation time, which characterizes the rate at which the distribution function returns to equilibrium due to scattering processes. The RTA assumes that phonons relax to the equilibrium distribution on a timescale that is independent of the phonon distribution itself, simplifying the solution of the equation and making it computationally efficient. The primary motivation for choosing the RTA over the full BTE is computational efficiency. In many practical cases, such as calculating thermal conductivity or studying heat transport in nanostructures, the RTA provides an adequate approximation to the full BTE while significantly reducing the complexity of the problem. The RTA has been successfully applied in numerous studies to model phonon transport in both bulk materials and nanostructures, yielding results that are in good agreement with experimental measurements in many cases. Additionally, the RTA allows for straightforward incorporation of various scattering mechanisms, such as phonon-phonon interactions, impurity scattering, and boundary scattering, through the phonon relaxation time. In practice, the relaxation time τ can be calculated using first-principles methods or obtained from experimental data, making the RTA a highly flexible and efficient tool for modeling phonon transport. Despite its simplicity, the RTA has limitations, especially in situations where phonon scattering is highly non-local or where deviations from equilibrium are significant. In such cases, the full BTE may be necessary to capture the full range of scattering effects. However, for many practical applications, especially those involving steady-state heat conduction, the RTA provides a sufficiently accurate and computationally feasible approach. For this reasons, we used the RTA approximation in every subsequent calculation, the only exception being the repetition of the computation of the thermal conductivity of the [100] bulk superlattice at 100 K, where we wanted to further strengthen the confidence with RTA results, due to the lack of a clear minimum in the thermal conductivity as a function of the SL period.

One more comment before presenting the results concerns the k-points grid convergence. In Density Functional Theory (DFT) calculations, the k-point grid is a critical parameter that affects the accuracy and computational cost of the calculations, and will be discussed in detail with DFT in the next chapter. Anyway, since our Si/Ge study involves DFT quantities, we performed a k-points grid convergence study before computing any other dependency, so we anticipate here that the k-point grid represents a discretization of the Brillouin zone, where the electronic wavefunctions are sampled.

DFT-BTE results

To probe into this aspect, we performed a batch of 40 simulations using the almaBTE software within the RTA approximation, computing κ for the 1.9 nm bulk SL along the [111] direction. Each sub-batch comprises 4 simulations perfomed at the same temperature, which correspond to the 10, 14, 20, and 24 k-points grid respectively, for a total of 10 data series, where temperature ranges evenly from 100 K to 1000 K. The results exhibit uniform convergence at 24 points for all temperatures, fixing the resolution for the subsequent simulations at this specific value. The results of this convergence study are provided in Figure 3.9 and Table 5.12. After this, we moved to the dependency of κ on the SL period, performing 60 simulations divided into groups of 6 simulations, each corresponding to a specific temperature, analogous to what we did in the convergence study. The results of our analysis are provided in Figure 3.10 and Table 5.13. Interestingly enough, the minimum they exhibit is located at about 9.5 nm, which is more than twice the value we found for the nanowires. Then we studied the dependence of κ on the SL period for the [100] direction at 100, 300 and 500 K, obtaining similar results. The batch at 100 K showed some differences though, so we repeated it with greater accuracy solving the full BTE, but the results still did not align with the other batches either, suggesting there may be some more physical processes going on at low temperture in this case. The results of this last analysis are provided in Figure 3.11 and Table 5.14.

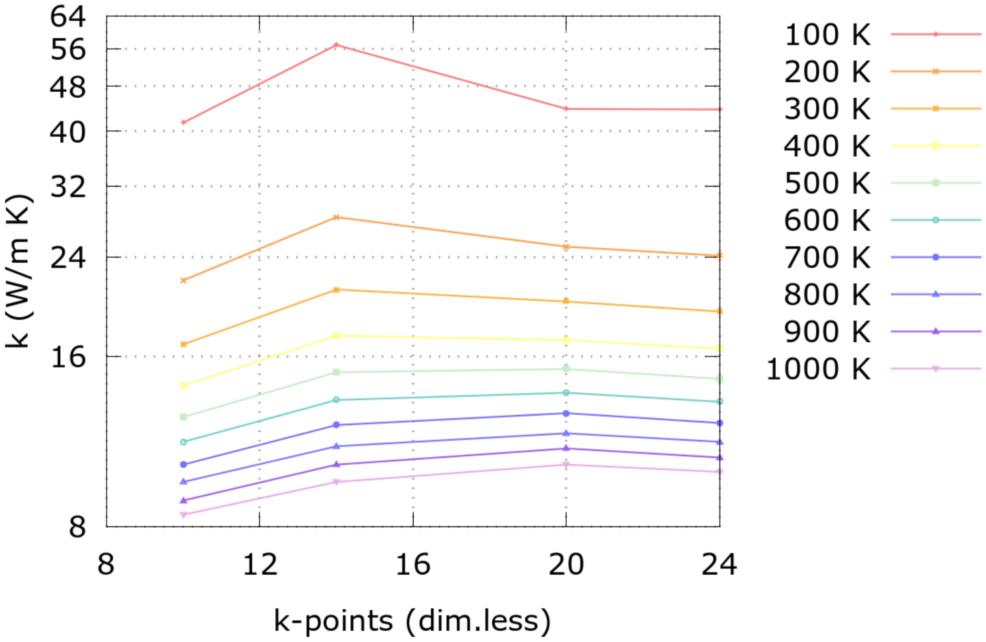

Figure 3.9: thermal conductivity of the [111] bulk superlattice as a function of the k-points grid number at different temperatures, computed with almaBTE

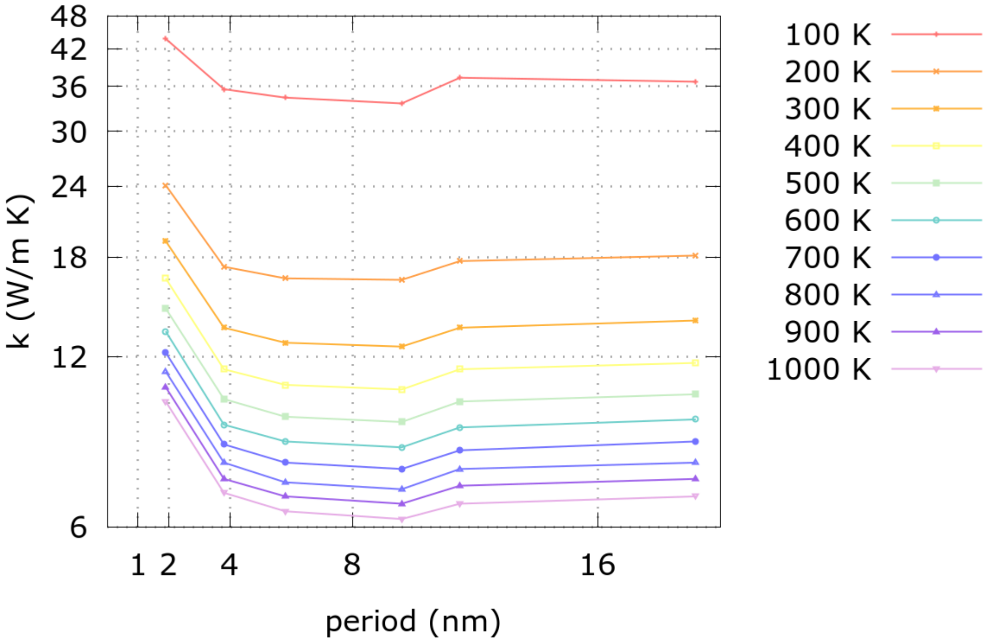

Figure 3.10: thermal conductivity of the [111] bulk superlattice as a function of the superlattice period at different temperatures, computed with almaBTE

As we have largely examined in Chapter 2, real interfaces exhibit a plethora of nonidealities, which heavily affect the thermal transport properties of nanostructured materials. For this reason, almaBTE includes a built-in feature that allows to tackle chemically mixed interfaces, when it comes to simulating superlattices, offering the possibility to regulate the amount of mixing in each layer. So, we introduced a gradual transition from Si to Ge between consecutive layers, using concentration variations of about 25 % and computed κ for the two crystal directions at 100, 300, and 500 K as a function of the SL period, plus one batch at 900 K for the [111] direction. In both cases, we observe a significant reduction of κ compared to their flat interface twin–as largely expected, together with a remarkably sharper minimum at

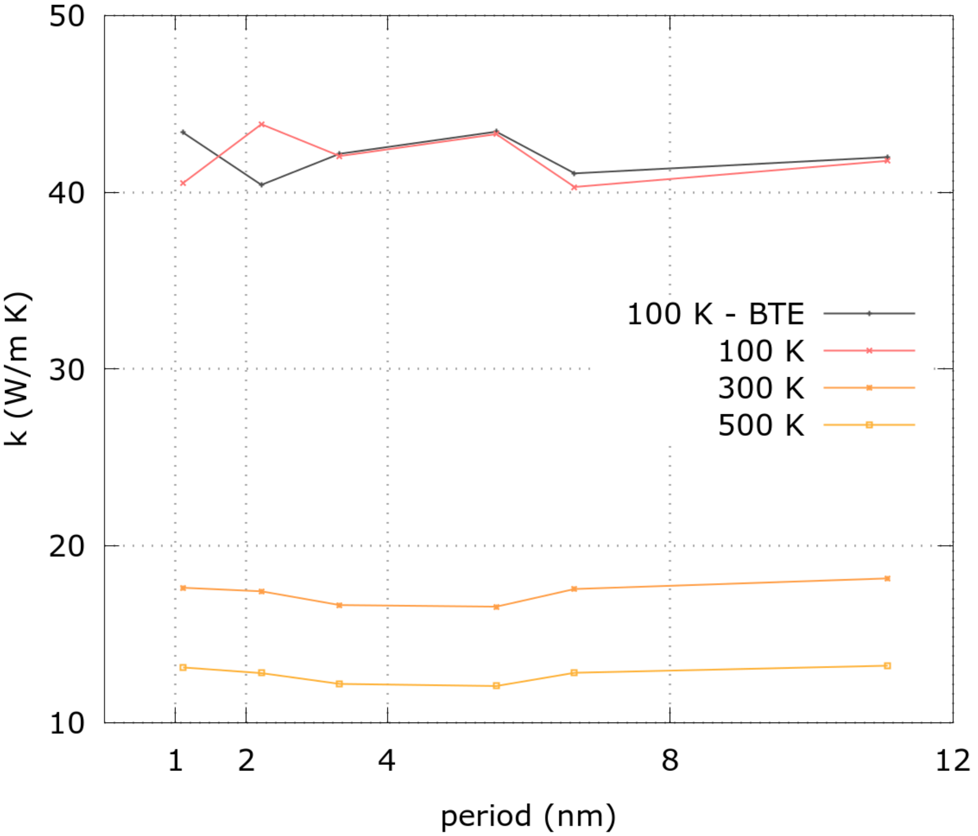

Figure 3.11: thermal conductivity of the [100] bulk superlattice as a function of the superlattice period at different temperatures, computed with almaBTE

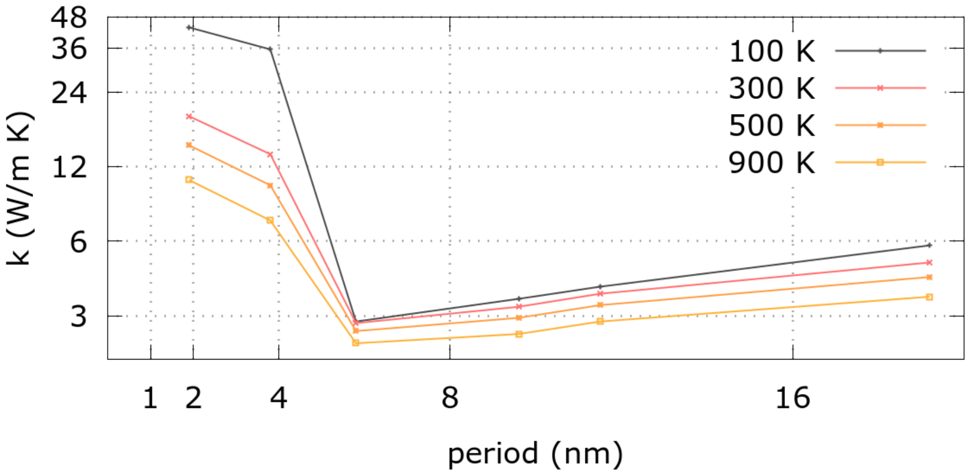

Figure 3.12: thermal conductivity of the [111] bulk superlattice with rough interfaces, as a function of the superlattice period at different temperatures, computed with almaBTE

around 6 nm, about 40 % smaller than the flat interface case. Last, κ increases rather seamlessly with the reciprocal interface density, signaling the presence of a more marked diffusive regime, in contrast to the flat interface scenario. The visual representation of our results are provided in Figure 3.12 and 3.13, corresponding to Tables 5.15 and 5.16 respectively.

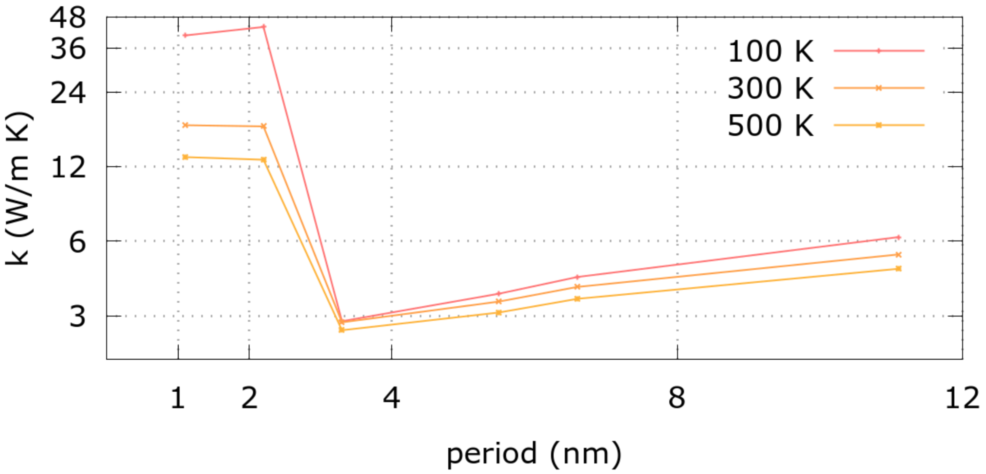

Figure 3.13: thermal conductivity of the [100] bulk superlattice with rough interfaces, as a function of the superlattice period at different temperatures, computed with almaBTE

NEMD results

To conclude the analysis of the Si/Ge bulk superlattice, we also used MD to perform 3 more simulation batches comprising 17 simulations each. In this case, contrary to almaBTE simulations, we can only simulate finite systems along the transport direction, and we chose to simulate the 120 nm x 8 nm2, 120 nm x 15 nm2, 180 nm x 8 nm2 geometries. The results align well with previous findings, and the qualitative trend is but the expected for every batch. We notice a rigid shift in the conductivity as a function of the SL period when the superlattice is extended from 120 to 180 nm–an indicator that we're not describing the properties of the infinitely system yet at 120 nm. Plus, we observe a rather fuzzy behavior around the minima for every geometry. We attributed it to the competition between two effects: on one side, longer periods imply lower interface densities, which in turn should make κ rise; on the other hand, since the total number of normal modes is $3N$–with N being the total number of atoms in the simulation, making the period longer would also increase the total number of optical modes against the number of acoustic modes, as the number of possible k-vector values diminishes dramatically, and this in turn implies lesser and lesser phonons are contributing to thermal transport. Moreover, the lack of such fluctuations in nanowires suggests that surface modes are likely accounting for most of the SLNW thermal conductivity. The results of this last analysis are provided in Figure 3.14 and Table 5.17.

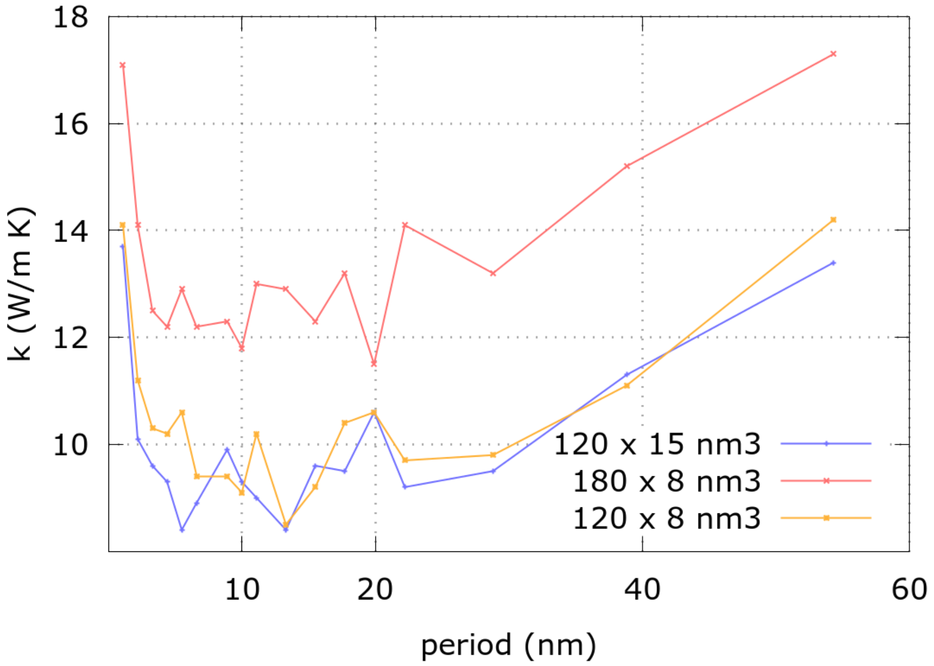

Figure 3.14: thermal conductivity of the [100] bulk superlattice as a function of the superlattice period at 300K, computed for different cell geometries using LAMMPS

3.3 Conclusions of Chapter 3

This study presented a comprehensive analysis of phonon transport in Si-Ge superlattices with atomically flat and chemically mixed interfaces, using both molecular dynamics and DFT-based approaches. Our results show that the superlattice period, transport direction, and system temperature play critical roles in determining the thermal conductivity. The combination of NEMD and almaBTE allows us to accurately probe into thermal transport properties, providing insights into the optimization of Si-Ge superlattices for thermoelectric applications. The thermal conductivity of SiGe superlattices is, in general, a strong function of the superlattice period and temperature. As the superlattice period increases from its minimum possible value, a significant reduction in thermal conductivity arises, particularly in the nanowire configurations, and then a subsequent increase, when the diffusive regime globally applies, and the total thermal resistance scales linearly with the interface density. This behavior is consistent with the increased phonon scattering at the interfaces in superlattices with longer periods, where boundary scattering leads to a reduction in the phonon MFP, and then the transition to the diffusive regime, where an increasingly lower number of interfaces is faced by the phonons that travel from end to end.

Transport along the [001] and [111] crystal directions reveals distinct anisotropic behavior. The thermal conductivity yields similar values along the [001] direction compared to the [111] direction, signaling little differences in phonon group velocities and scattering rates in these directions. The simulations conducted using almaBTE confirm these trends, providing quantitative predictions of thermal conductivity for both crystallographic orientations. The temperature dependence of the thermal conductivity in SiGe bulk superlattices also decreases as the system temperature increases, in line with the expected behavior of semiconductor materials, where increased phonon-phonon scattering at higher temperatures dominates the transport process. These results are of help for understanding the thermal management of SiGe-based thermoelectric devices, where minimizing thermal conductivity while maintaining reasonable electrical properties is key to enhancing performance.

Chapter 4

Raman Spectroscopy of Superlattices

The study of thermal transport across semiconductor interfaces has far-reaching implications in electronics and optoelectronics. Superlattices, with their precisely engineered periodic structures, provide an ideal platform for tuning phonon and electronic properties, enabling novel thermal and optoelectronic applications. This chapter focuses on the Raman spectroscopy of two distinct semiconductor superlattices: the GaAs/GaP superlattice and the InAs twinning superlattice. GaAs/GaP superlattices exhibit intriguing optical and thermal properties due to their ability to confine phonons and modulate their thermal conductivity, making them prime candidates for thermoelectric and photonic devices. InAs-based twinning superlattices, on the other hand, leverage structural modulations to control electronic and phononic interactions, enabling the fine-tuning of thermal transport properties. Raman spectral analysis provides insight into the vibrational modes of these systems, offering a pathway to understand and optimize their performance. In this chapter, we analyze experimental and theoretical Raman spectra to investigate the phononic and electronic characteristics of these superlattices. The findings are contextualized with recent advances in superlattice design and their implications for controlling phonon transport at the nanoscale. Key references include works on Raman analysis of GaAs/GaP structures and phonon transport in twinning superlattices, emphasizing their utility in next-generation thermal and optoelectronic systems [76–79].

4.1 Introduction to Raman Spectroscopy

The story of Raman spectroscopy begins in 1928, when Sir Chandrasekhara Venkata Raman first observed the phenomenon that would later bear his name [80]. Working with simple equipment - merely a telescope and some polarizers - he discovered that when light interacts with matter, a tiny fraction of the scattered photons emerges with altered energy. This groundbreaking discovery, which earned him the 1930 Nobel Prize in Physics, opened new windows into the world of molecular vibrations and material properties.

At its heart, Raman spectroscopy tells us the tale of light's intimate dance with matter. When a photon encounters a molecule, their interaction usually results in elastic scattering, known as Rayleigh scattering, where the photon maintains its original energy. However, roughly one in ten million photons undergoes a more interesting fate. These rare events, which we now call Raman scattering, involve an energy exchange between the photon and the molecule's vibrational states. This exchange manifests in two ways, as explained by Long in his comprehensive treatise [81]. In Stokes scattering, the incident photon shares some of its energy with the molecule, exciting it to a higher vibrational state. The scattered photon emerges with slightly less energy, carrying a unique spectral signature of the molecular vibration. Conversely, in Anti-Stokes scattering, an already excited molecule transfers its excess energy to the scattered photon, which departs with increased energy. The journey from observation to application has been remarkable. Modern Raman spectroscopy, as described by Weber and Merlin [82], employs sophisticated instrumentation to capture these subtle spectral changes. A typical experimental setup reads like a symphony of optical components working in concert: a monochromatic laser source provides the initial photons, which interact with the sample before being collected, analyzed, and detected with considerable precision. In the realm of nanoscale thermal transport, Raman spectroscopy has proven particularly illuminating. The technique's ability to probe phonon dynamics, as detailed by Balandin [83], provides direct insight into thermal energy carriers at the molecular level. The temperature dependence of Raman spectra, expressed through the relation $\omega(T) = \omega_0 + \chi T$, enables precise thermal mapping with sub-micron resolution. Recent years have witnessed remarkable advances in the field.

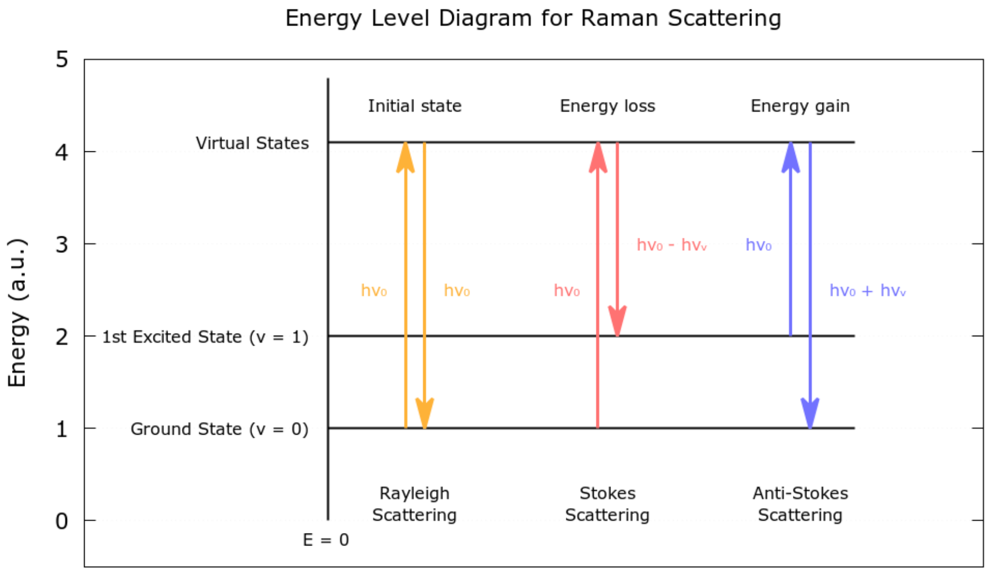

Figure 4.1: Energy level diagram illustrating the delicate dance between photons and molecules during Raman scattering. The diagram shows the three possible outcomes: Rayleigh scattering, where energy remains unchanged, and the two types of Raman scattering - Stokes and Anti-Stokes.

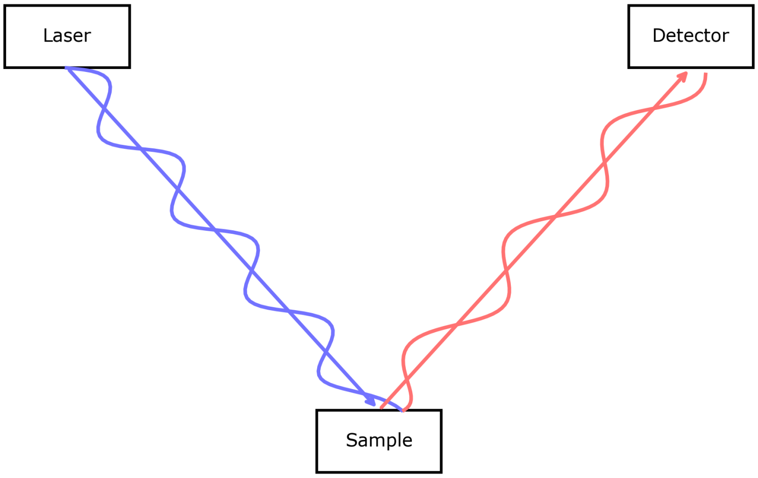

Figure 4.2: Schematic diagram of a typical Raman spectroscopy setup (Stokes). The sample absorbs some energy, thus heating itself up during the process.

Time-resolved measurements, as pioneered by Zewail [84], have extended Raman spectroscopy into the ultrafast regime, allowing us to observe thermal processes on previously inaccessible timescales. Surface-enhanced techniques, building on the work of Fleischmann [85], have pushed detection limits to new extremes, while tip-enhanced methods have broken through the diffraction barrier to achieve nanoscale spatial resolution. As we continue to explore the frontiers of nanoscale thermal transport, Raman spectroscopy stands as a testament to how a single discovery can revolutionize our understanding of the material world. From its humble beginnings in Raman's laboratory to today's sophisticated implementations, it remains an indispensable tool in our scientific arsenal, helping us unravel the complex interplay between light, matter, and thermal energy at the nanoscale.

4.2 Density Functional Theory

In this section, we delve further into laying the groundwork for our computational journey. Density Functional Theory (DFT) stands as a powerful and widely adopted theoretical framework in condensed matter physics and quantum chemistry. Developed to address complex many-body quantum systems, DFT provides a practical approach for studying electronic structure and properties of materials. The central concept revolves around the electron density, a key variable that encapsulates the behavior of interacting electrons. Unlike traditional quantum mechanical methods that involve solving the Schrödinger equation for each electron, DFT simplifies the problem by focusing on the electron density as the primary variable of interest. This reduction significantly enhances computational efficiency while retaining accuracy. At its core, DFT employs the Hohenberg-Kohn theorems to establish a one-to-one correspondence between the ground-state electron density and the external potential. The Kohn-Sham equations further refine the approach, introducing fictitious non-interacting electrons in an effective potential to represent the complex many-electron system. This transformation enables the application of well-established techniques from single-particle quantum mechanics, making computations more tractable. DFT has proven invaluable in elucidating the electronic structure of diverse materials, ranging from simple atoms to intricate molecules and solid-state systems, fostering breakthroughs in materials science, chemistry, and physics research.

The three most fundamental equations in DFT are associated with the Kohn-Sham equations and the total energy functional.

$$\hat{H}_{\mathrm{KS}}[\rho]\psi_i(\mathbf{r}) = \varepsilon_i \psi_i(\mathbf{r}) \tag{4.1}$$

The Kohn-Sham equation describes a set of single-electron equations, where $\hat{H}_{\mathrm{KS}}[\rho]$ is the Kohn-Sham Hamiltonian, $\psi_i(\mathbf{r})$ are the Kohn-Sham orbitals, ε_i are the corresponding orbital energies, and ρ is the electron density.

$$\rho(\mathbf{r}) = \sum_i^N |\psi_i(\mathbf{r})|^2 \tag{4.2}$$

The Kohn-Sham density equation defines the electron density (ρ) as the sum of the squared magnitudes of the Kohn-Sham orbitals ($|\psi_i(\mathbf{r})|^2$) for all occupied orbitals (i).

$$E_{\mathrm{total}}[\rho] = T[\rho] + U[\rho] + V_{\mathrm{ext}}[\rho] + E_{\mathrm{xc}}[\rho] \tag{4.3}$$

The total energy functional comprises the kinetic energy ($T[\rho]$), electron-electron interaction energy ($U[\rho]$), external potential energy ($V_{\mathrm{ext}}[\rho]$), and the exchange-correlation energy ($E_{\mathrm{xc}}[\rho]$). The minimization of this functional with respect to the electron density yields the ground-state properties of the system. ABINIT, a powerful open-source software package for quantum mechanical calculations, implements the core equations of DFT to predict electronic structures of materials. The Kohn-Sham equation is solved iteratively using a combination of numerical methods. The Kohn-Sham density equation calculates the electron density from the occupied Kohn-Sham orbitals. ABINIT employs a plane-wave basis set to represent wavefunctions and discretizes the Brillouin zone for numerical efficiency. The total energy functional $E_{\mathrm{total}}[\rho]$ is then minimized through self-consistent iterations, yielding accurate predictions of material properties and behaviors. The ABINIT code is extensively documented in the literature [86, 87]. The reader can refer to these canonical references for a comprehensive understanding of the ABINIT software.

4.3 Perturbation Theory and Raman Spectra

While Density Functional Theory (DFT) provides an efficient means to obtain the ground-state properties of materials, many experimental observables rely on the system's response to external perturbations. Density Functional Perturbation Theory (DFPT) extends the DFT framework to systematically treat small perturbations, allowing for the direct calculation of response functions and related properties [88]. In DFPT the focus shifts to the linear response of the electronic density to a given perturbation, such as an external electric field or atomic displacements. By computing the second derivatives of the total energy with respect to these perturbations, one can obtain crucial quantities like phonon frequencies, dielectric constants, and electron-phonon coupling coefficients. This variational approach not only avoids the computational expense of finite-difference methods but also ensures a higher degree of numerical accuracy.

A particularly important application of DFPT is in the computation of Raman spectra. Raman scattering involves the inelastic scattering of light by vibrational modes of a material, and its intensity is determined by the derivative of the polarizability tensor with respect to the vibrational coordinates. DFPT facilitates the computation of these derivatives by perturbing the electronic density and evaluating the corresponding response of the polarizability. The calculated phonon eigenmodes, together with the Raman tensors, enable the simulation of Raman spectra that can be directly compared with experimental measurements [89]. In practice, implementations of DFPT within DFT codes (such as ABINIT) allow us to compute not only the vibrational properties but also other lattice dynamical phenomena such as infrared absorption and thermal conductivity. This integration makes DFPT a powerful tool for exploring both fundamental material properties and technologically relevant phenomena, thereby bridging the gap between theoretical predictions and experimental observations.

4.4 *k*-points grid and energy cutoff

In DFT, the total energy and other derived properties are computed by integrating over the Brillouin zone. This integration is performed numerically, with a chosen set of k-points determining the resolution of the sampling. The grid is typically represented by a set of discrete points, $\mathbf{k}$, that span the entire Brillouin zone. As the number of k-points increases, the resolution of the grid improves, leading to more accurate results. However, a higher k-point density also increases the computational cost, making it essential to balance accuracy and efficiency. The plane-wave energy cutoff, denoted as E_{cut}, defines the maximum kinetic energy of the plane waves included in the basis set expansion. A higher energy cutoff includes more plane waves, potentially improving the accuracy of the calculation, but at the cost of increased computational resources. The convergence of properties with respect to E_{cut} is particularly important for systems containing elements with localized electronic states or when studying properties that depend sensitively on the details of the electronic structure, such as phonon frequencies and Raman intensities. The choice of k-points directly influences the precision of computed properties, such as electronic energy, charge density, and phonon properties. Similarly, the plane-wave energy cutoff is a crucial parameter that determines the completeness of the basis set used to represent the electronic wavefunctions. In this section, we discuss the importance of both k-point grid and energy cutoff convergence and their impact on DFT calculations, particularly for thermal transport studies. To achieve convergence in DFT calculations, both the k-point grid must be sufficiently fine and the energy cutoff sufficiently high to ensure that the results do not change significantly with further refinement of either parameter. The convergence behavior can be assessed by systematically increasing the number of k-points and energy cutoff independently, observing the change in calculated properties, such as the total energy, electronic structure, and phonon dispersions. Typically, a convergence threshold of $1 \times 10^{-3}\,\mathrm{eV}$ in energy is used for assessing the accuracy of the calculations.

For systems with high symmetry, such as cubic crystals, the k-point grid can often be chosen to reflect the symmetry of the system, thereby reducing the number of points required for convergence. For more complex or low-symmetry systems, a denser k-point grid may be necessary to achieve convergence. Additionally, the choice of grid shape (e.g., Monkhorst-Pack grid [90]) and the use of special k-points, such as those along high-symmetry directions, can significantly impact the accuracy and efficiency of the calculations. The energy cutoff requirements can vary significantly between different elements and pseudopotentials. For instance, first-row elements and systems with d or f electrons typically require higher energy cutoffs compared to other elements. In the case of GaP and GaAs wurtzites, the presence of semicore states in Ga and the different electronic characteristics of P and As necessitate careful convergence testing of both k-points and energy cutoff to ensure reliable results. In the context of phonon calculations and thermal transport studies, convergence of both parameters is particularly important because the phonon dispersion relations, which are essential for modeling thermal conductivity, depend on the accurate sampling of the electronic states and the completeness of the basis set. Inaccurate k-point grids or insufficient energy cutoffs can lead to incorrect phonon frequencies and scattering rates, ultimately affecting the predicted thermal conductivity and optical spectra. In practical applications, a dense k-point grid and appropriate energy cutoff are often required for accurate calculations, especially when dealing with complex nanostructures or materials with low symmetry.

4.5 GaP and GaAs Wurtzites

Determining the optimal computational parameters for accurate phonon calculations in wurtzite-structured III-V semiconductors is crucial for reliable Raman spectra predictions. The convergence analysis of GaP and GaAs wurtzites with respect to plane-wave energy cutoff and k-point sampling density forms the foundation for studying their vibrational properties and those of their derived superlattices. This systematic investigation ensures that subsequent calculations of phonon frequencies and Raman intensities are performed with parameters that balance computational efficiency with numerical accuracy. By establishing these convergence criteria, we can confidently proceed with the analysis of the lattice dynamics and spectroscopic properties of these technologically relevant semiconductor systems.

Both Wurtzite and Zincblende structures display tetrahedral coordination; however, they differ in several key aspects: Zincblende adopts a cubic structure (space group F-43m) and exhibits isotropic physical properties, while Wurtzite crystallizes in a hexagonal lattice (space group P6$_3$mc) that gives rise to anisotropic properties and a non-centrosymmetric character. Parallel to this, in Zincblende the stacking along the [111] axis follows an ABCABC pattern, whereas in Wurtzite it follows an ABAB sequence. For example, in ZnO the Wurtzite phase has lattice constants $a \approx 3.25\,\text{Å}$ and $c \approx 5.20\,\text{Å}$ (with $c/a \approx 1.60$, nearly the ideal value), while Zincblende ZnS typically has a lattice constant of about 5.42 Å [91]. These differences strongly affect the phonon dispersion relations and the Raman activity. For instance, the lower symmetry and intrinsic polarization in Wurtzite lead to additional Raman-active modes and anisotropic phonon group velocities [91]. Recent experimental advances have demonstrated that GaP and GaAs can be stabilized in the Wurtzite phase under non-equilibrium conditions. The inherent anisotropy and the possibility to control the interface quality make the axial GaP/GaAs superlattices (grown along the cubic [111] direction) an ideal platform for detailed Raman spectroscopic studies. Such superlattices allow one to probe the impact of periodic modulations on phonon modes and enable the engineering of phononic bandgaps—an essential step in designing metamaterials with tailored thermal and optoelectronic properties [92].

To understand the microscopic origins of the vibrational properties in these wurtzite phases and their interfaces, first-principles density functional theory (DFT) calculations were performed using the ABINIT code [93]. In our study, we carefully investigated the convergence of the total energy, electronic eigenvalues, and phonon frequencies with respect to both the plane-wave energy cutoff (Ecut) and the k-point sampling of the Brillouin zone. In particular, we set the energy cutoff to 40 Ha, securing high precision in the following steps, and computed the whole set of phonon frequencies–i.e. the normal modes–for both GaAs and GaP wurtzites, for 6 different values of the k-points number, ranging evenly from $6 \times 6 \times A$ to $16 \times 16 \times B$. Then we picked the grid yielding reasonably convergent values of the phonon frequencies at fair computational cost–uncertainties about 1%, compared to their values at the densest grid, and carried on another convergence study with respect to the energy cutoff, repeating the computation of the phonon frequencies varying the cutoff from 30 to 42 Ha.

Our convergence test indicate that an energy cutoff of 37 Ha and a Monkhorst-Pack grid of $8 \times 8 \times 5$ yield robust results, showcasing relative uncertainties below 1% in the general case, which can be then employed in the subsequent superlattice analysis. Such systematic convergence is essential for accurately predicting the Raman spectra and phonon transport properties across the superlattice interfaces. The results of the convergence study are plotted Figures 4.4a, 4.4b, 4.5a, and 4.5b. To aid in understanding the crystallographic arrangement, a snippet is also provided in Figure 4.3, for the primitive cell of a typical Wurtzite structure for a GaAs- or GaP-like compound. We provide the phonon frequencies of GaP and GaAs resulting from this study in Table 5.18.

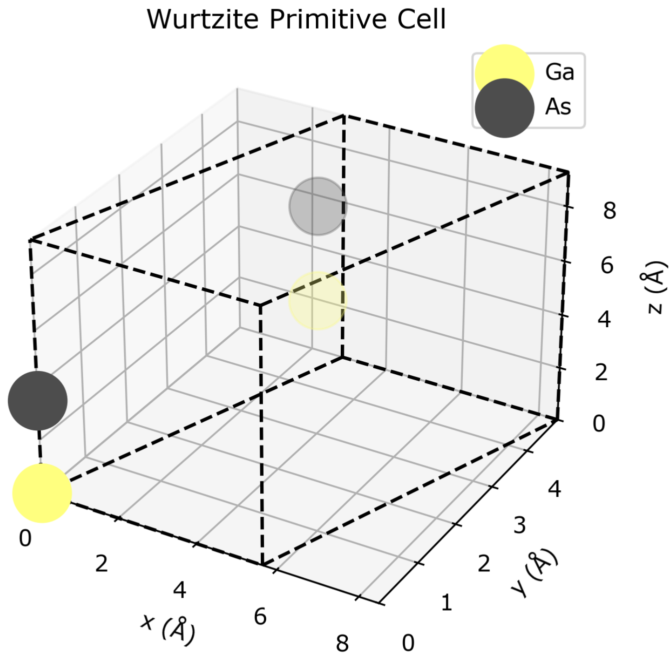

Figure 4.3: Schematic of the Wurtzite primitive cell for GaAs.

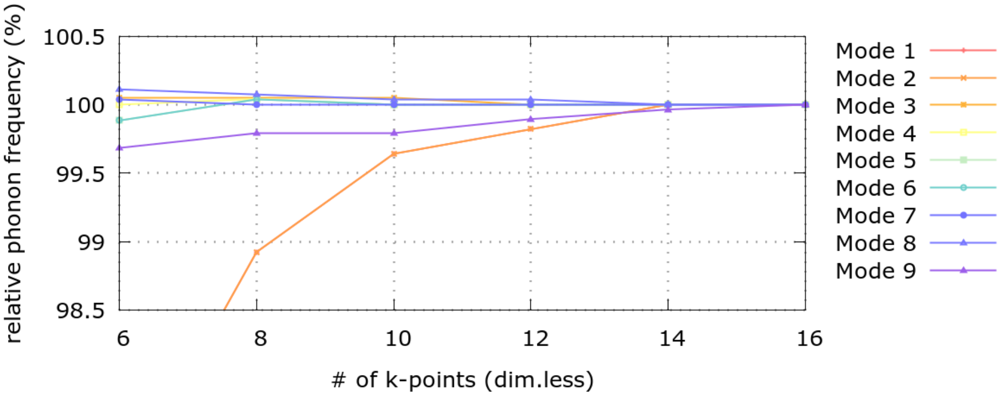

(a) GaAs

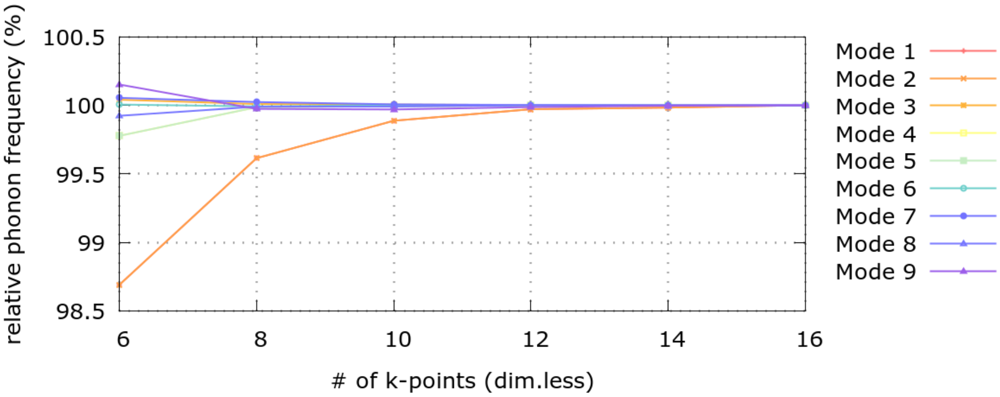

(b) GaP

Figure 4.4: Relative phonon frequencies dependance on the number of k-points, with respect to their values computed using the 16 × 16 × 10 grid

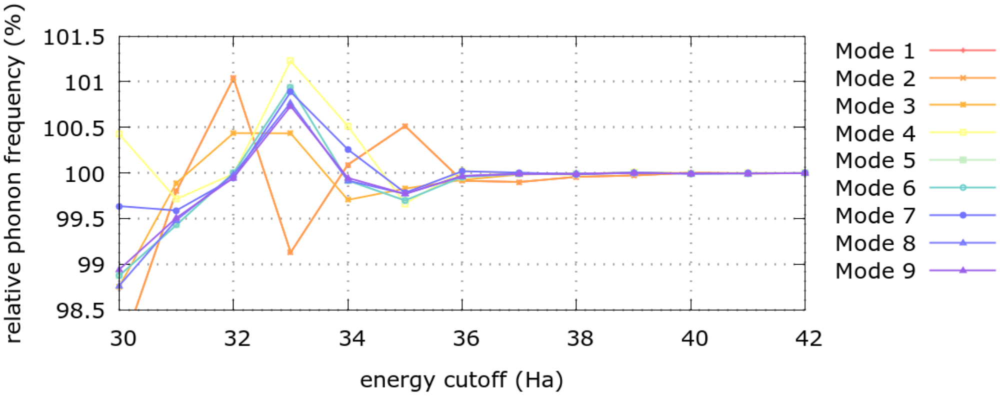

(a) GaAs

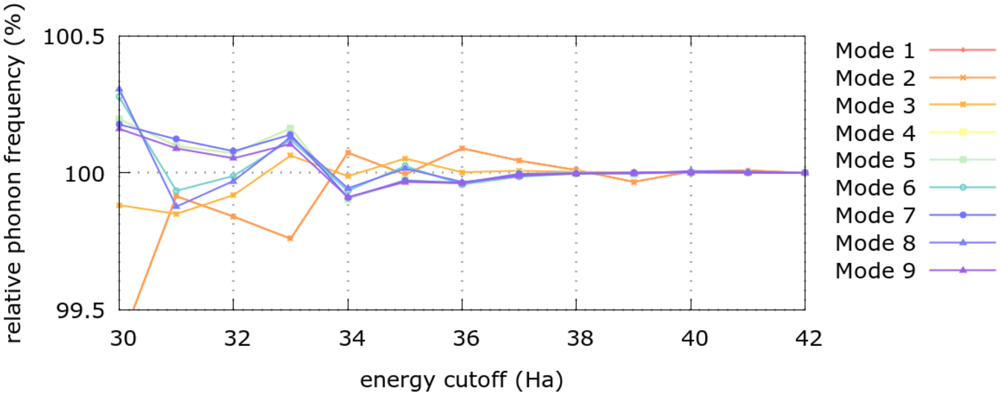

(b) GaP

Figure 4.5: Relative phonon frequencies dependance on the energy cutoff, with respect to their values computed at 42 Ha

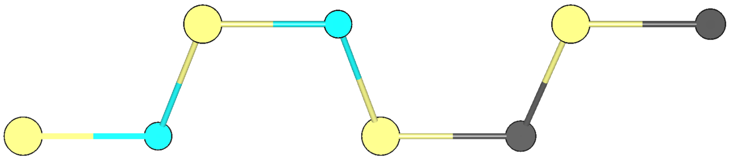

(a) 1.28 nm

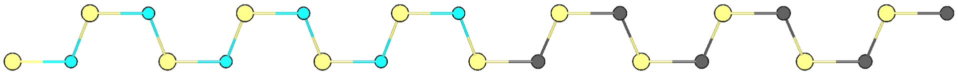

(b) 3.83 nm

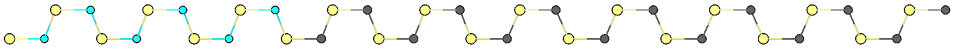

(c) 6.39 nm

Figure 4.6: GaP/GaAs SL primitive cell snippets for the shortest, mid, and largest simulated periods

4.6 The GaAs/GaP superlattices

The systems under investigation comprised superlattices (SLs) constructed by stacking unit cells of wurtzite GaAs and GaP along the [0001] crystal direction. SLs with periods of 1.28, 2.56, 3.83, 5.12, and 6.39 nm were considered. We provide a snippet of the SL primitive cell for three representative cases in Figures 4.6a, 4.6b, and 4.6c.

4.6.1 Computational Methodology

The Raman tensors were evaluated by computing the third derivative of the total energy, where two derivatives correspond to the perturbations induced by the electric field (associated with the incident and scattered light polarization vectors) and one derivative corresponds to the phonon displacement coordinate [86, 88]. All calculations were performed with the ABINIT software package. In our simulations, the local density approximation (LDA) was employed for the exchange-correlation energy functional and norm-conserving pseudopotentials were used to accurately represent the electron-ion interactions. The plane-wave basis set was truncated at a kinetic energy cutoff of 37 Ha, while a finer fast Fourier transform grid was maintained with an energy cutoff of 76 Ha. A stringent convergence criterion was imposed on the wave function residual norm, set to 10^{-22}, to ensure high numerical accuracy. For Brillouin zone integration, an $8 \times 8 \times N$ k-point grid was adopted, with the number of k-points along the [0001] axis decreasing from 3 to 1 as the period increased. Prior to the Raman spectra computation, all structures underwent full structural relaxation, optimizing both the atomic positions and the lattice parameters without imposing additional constraints. The simulations were performed on bulk systems, ensuring a consistent environment for the evaluation of the Raman response.

4.6.2 Results

The simulated Raman spectra exhibit detailed structure that reflects the influence of superlattice periodicity on phonon behavior. In all cases, the characteristic TO and LO phonon modes of the GaP-like and GaAs-like wurtzite segments remain the most prominent features, with their frequencies shifting by only 2–3 cm^{-1} and peak intensities varying by approximately 10–20% as the period increases. This behavior indicates that the alternating layer thickness produces a modest modification of the local bonding environment.

Concurrently, a series of weaker, lower-frequency modes emerges below the bulk TO frequencies (approximately 240–300 cm^{-1} for GaAs-like modes and 340–370 cm^{-1} for GaP-like modes). These additional peaks arise from Brillouin-zone folding associated with the enlargement of the unit cell. Their number increases from a few in the shortest-period superlattices to more than a dozen in the longest-period structures, while their individual intensities decrease, consistent with long-wavelength, collective vibrations.

The relative intensities of these folded modes also depend on the polarization configuration: certain branches exhibit greater Raman activity when both incident and scattered polarizations are aligned with the wire axis, whereas others are more active in the perpendicular configuration. This polarization dependence corresponds to differences in the atomic displacement patterns of the modes.

Overall, these results demonstrate that varying the superlattice period provides a systematic method for tuning both the frequencies and optical activities of an extended set of phonon modes in GaAs/GaP nanowires. The full set of Raman spectra for every polarization setup and SL period is provided in Figures 4.7a, 4.7b, 4.8a, 4.8b, and 4.9. The notation: "compound – inward polarization – outward polarization" is used. The frequency is expressed in cm^{-1}; the intensity is expressed in arbitrary units. The X and Y directions are equivalent due to crystal symmetry, while A-B and B–A configurations are equivalent due to time-reversal symmetry.

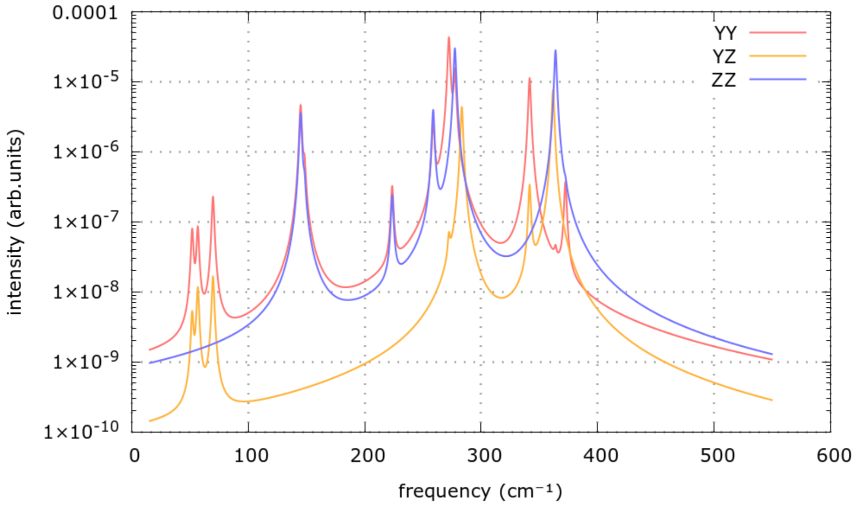

(a) 1.28 nm

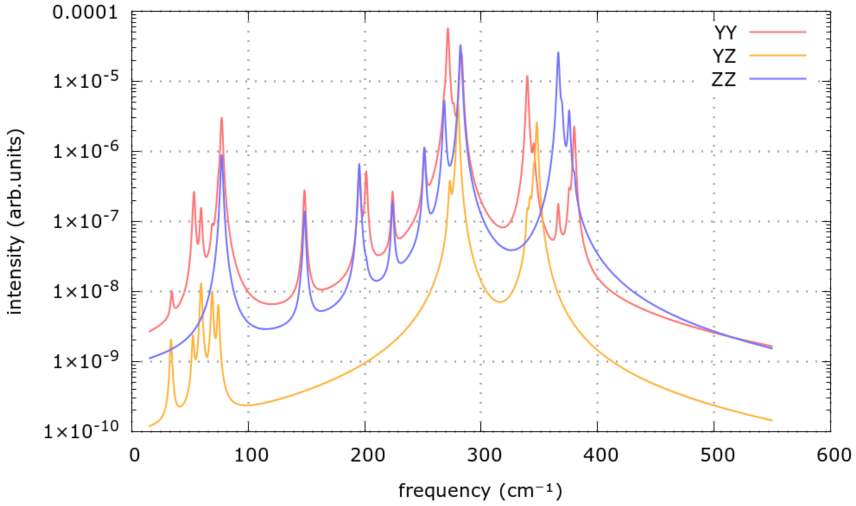

(b) 2.56 nm

Figure 4.7: Raman spectra of the GaP/GaAs SL for every nonequivalent polarization setup - log scale

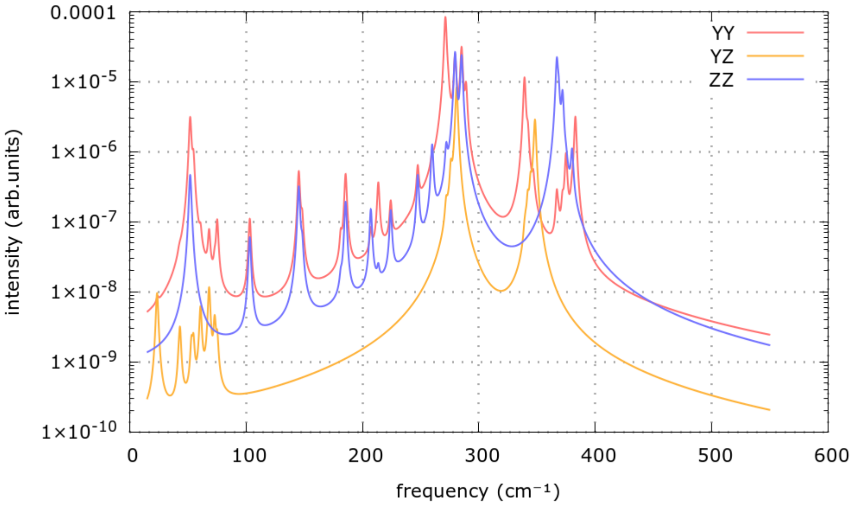

(a) 3.83 nm

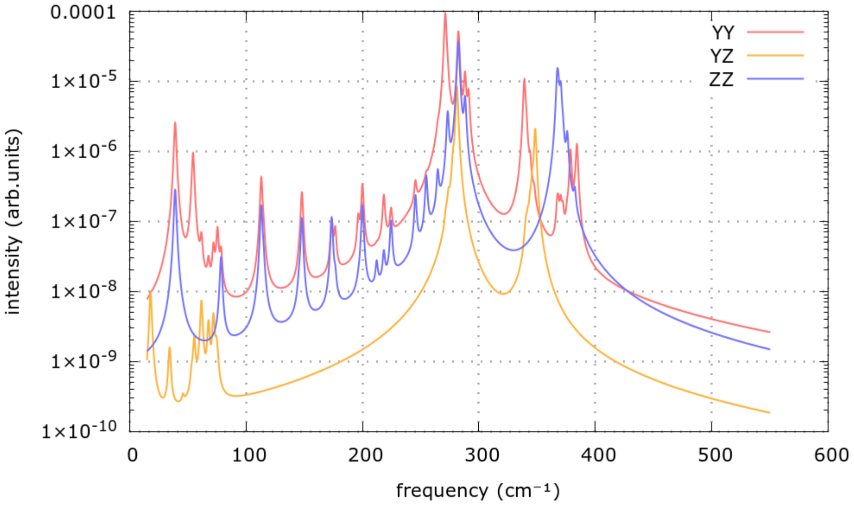

(b) 5.12 nm

Figure 4.8: Raman spectra of the GaP/GaAs SL for every nonequivalent polarization setup - log scale

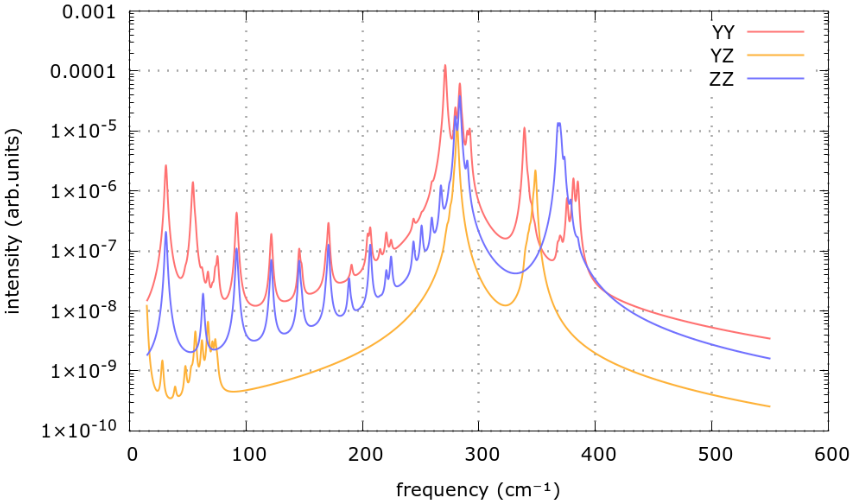

Figure 4.9: 6.39 nm

Figure 4.10: Raman spectrum of the GaP/GaAs SL for every nonequivalent polarization setup - log scale

4.7 Twinning Superlattices: The InAs Case Study

The preceding discussion has elucidated the Raman spectral characteristics and vibrational dynamics inherent to conventional GaAs/GaP superlattices, where alternating layers impart distinct electronic and structural properties. Building on these insights, we now turn our attention to an alternative structural paradigm—twinning superlattices (TSLs). In contrast to the layered architecture of traditional superlattices, TSLs exhibit periodic twin boundaries within a single crystalline phase, a modification that fundamentally alters the symmetry and response of the system. In particular, TSL can exist only in the form of NWs, because the twinning is obtained by a periodic rotation of the substratum during the crystal growth, which would induce a definite lattice mismatch yet for mesoscale systems, thus preventing the formation of the SL. In the subsequent sections, we focus on InAs twinning superlattices as a case study, investigating how the deliberate introduction of twin domains influences both the electronic band structure and the Raman response. This transition not only expands the scope of our investigation but also underscores the versatility of our computational approach in capturing the interplay between structure and spectroscopic properties. Twinning superlattices (TSLs) represent a fascinating class of nanostructured materials, characterized by the periodic arrangement of twin boundaries within a single crystalline phase. These twin boundaries, which separate domains of differing crystallographic orientation, lead to a modulation of the electronic potential and, consequently, to alterations in both the electronic and vibrational properties of the host material [94]. Such structural modulations are known to influence key material characteristics, including carrier mobility, band alignment, and phonon dispersion, thereby opening way for device optimization in optoelectronics and high-speed electronics. In the context of III-V semiconductors, InAs has emerged as a prototypical material for exploring the effects of twinning on physical properties. InAs-based TSLs are typically engineered via controlled epitaxial growth techniques—such as molecular beam epitaxy (MBE) or metal-organic chemical vapor deposition (MOCVD)—which allow for the deliberate incorporation of twin boundaries along preferred crystallographic directions [95]. The resulting periodic modulation in the crystal structure gives rise to unique band structures and vibrational spectra, distinguishing these systems from their conventional counterparts. Our case study focuses on the InAs TSL, wherein alternating twin domains are introduced in a periodic fashion along the [111] (or an equivalent) crystallographic direction. The computational framework is the same outlined in the previous sections—based on Density Functional Theory (DFT) and Density Functional Perturbation Theory (DFPT). After performing full structural relaxation to optimize both atomic positions and lattice parameters, our calculations reveal the impact of the periodic twin boundaries on the TSL spectra, which exhibits distinctive features attributable to the twin boundaries, thereby providing a comprehensive understanding of the interplay between structural modulation and physical observables. Specifically, we computed the Raman spectra of the InAs TSL with periods 2.09, 4.17, and 6.26 nm for all the non-equivalent values of incoming and outgoing polarizations. We provide a snippet of the corresponding primitive cells in Figures 4.11a, 4.11b, and 4.11c, and the results of our simulations in Figures 4.12a, 4.12b, and 4.13.

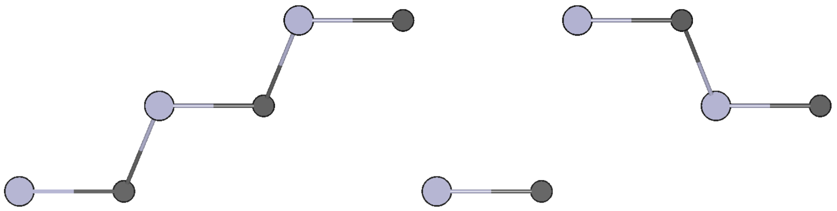

(a) 2.09 nm

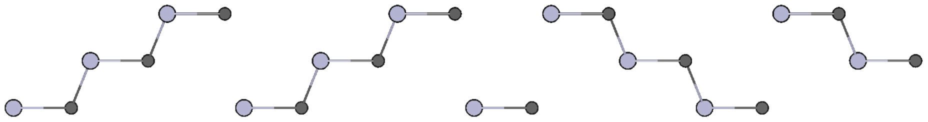

(b) 4.17 nm

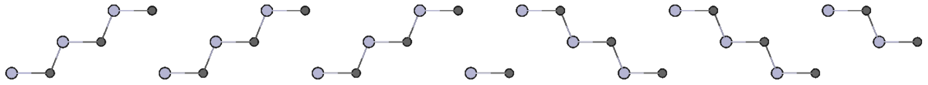

(c) 6.26 nm

Figure 4.11: InAs TSL primitive cells of the three superlattice periods considered

4.7.1 Results

The observation of numerous optical phonon branches superimposed on the intrinsic InAs transverse- and longitudinal-optical frequencies demonstrates that twinning defects profoundly reshape the vibrational landscape of the wire. In particular, the introduction of periodic 60° rotations breaks the original cubic symmetry and effectively creates a one-dimensional phononic superstructure. As a result, phonon dispersion curves—which in bulk or uniformly strained InAs would be continuous—become folded into a reduced Brillouin zone, giving rise to a dense set of quantized optical branches–Figures 4.12a, 4.12b, and 4.13.

When the twinning period is systematically increased, a clear attenuation of these low-frequency "folded" modes is seen: their Raman or infrared activity diminishes with spacing, while their spectral separation narrows. This trend contrasts sharply with conventional GaP/GaAs chemical superlattices, where sharp compositional interfaces yield strong phonon confinement and correspondingly intense folded modes at low energies. In the purely crystallographic case of a twinning superlattice (TSL), the atomic species remain homogeneous (all In and all As), and only the local stacking orientation varies. Consequently, the local force-constant environment is only weakly perturbed by each twin boundary, and the resulting optical modes carry only a fraction of the oscillator strength found in mixed-chemistry superlattices.

This moderate distortion manifests in two key ways. First, the intensities of the low-frequency TSL modes in twinned InAs are significantly smaller—often by an order of magnitude—than those in GaP/GaAs heterostructures with similar periodicities. Second, the frequency shifts of the "bulk-like" TO and LO modes are subtle (on the order of 1–2 cm^{-1}) even as period varies, confirming that the TSL planes act primarily as phase boundaries rather than as strong scattering centers. In chemical superlattices, by contrast, the abrupt change in bond type (and mass contrast) at each interface leads to much larger shifts and mode splittings.

Taken together, these findings highlight the dual nature of twinning superlattices: on one hand, they offer a new route to engineer phonon dispersions in a single-material system, allowing the creation of hexagonally symmetric phonon modes (e.g. E_2-type optical phonons) and a host of folded branches. On the other hand, the "soft" nature of the twin boundary perturbation means that the modification of primitive-cell normal modes remains modest compared to compositional heterostructures.

Overall, these insights underscore both the versatility of first-principles computational approaches for predicting complex phonon behavior and the promise of TSLs as a uniquely tunable, single-material avenue toward phononic engineering in electronics and optoelectronics.

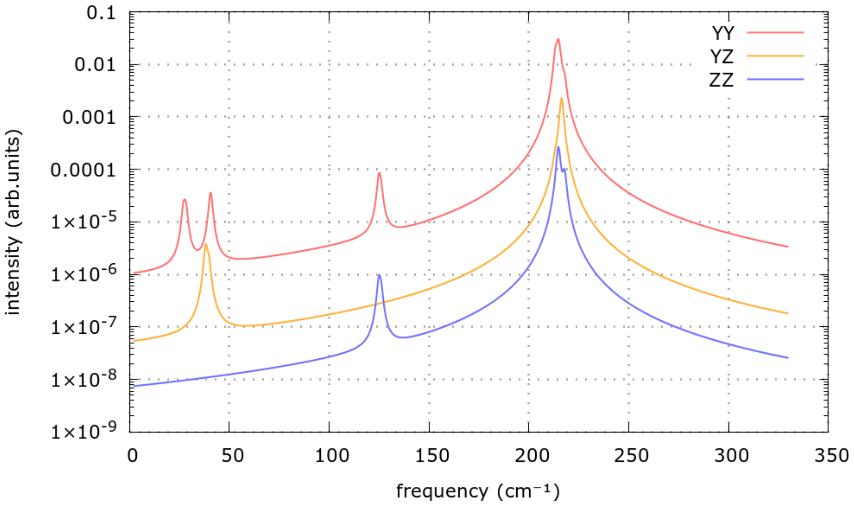

(a) 2.09 nm

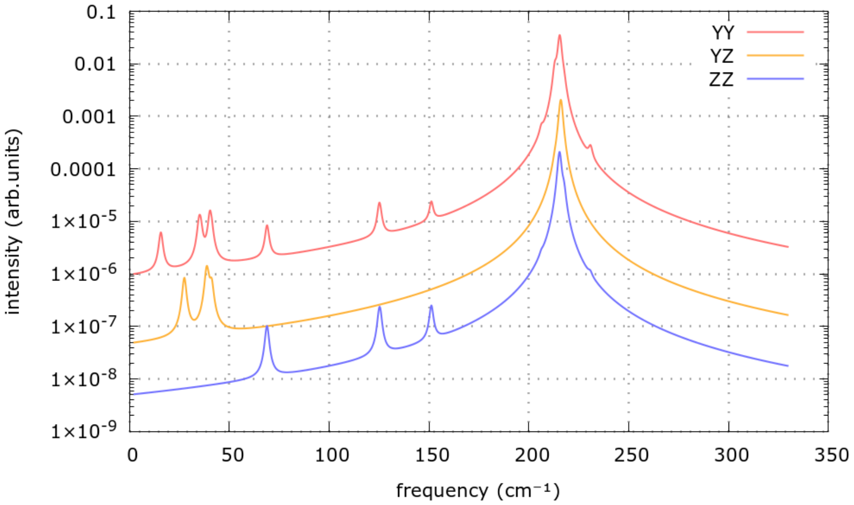

(b) 4.17 nm

Figure 4.12: Raman spectra of the InAs TSL for every nonequivalent polarization setup

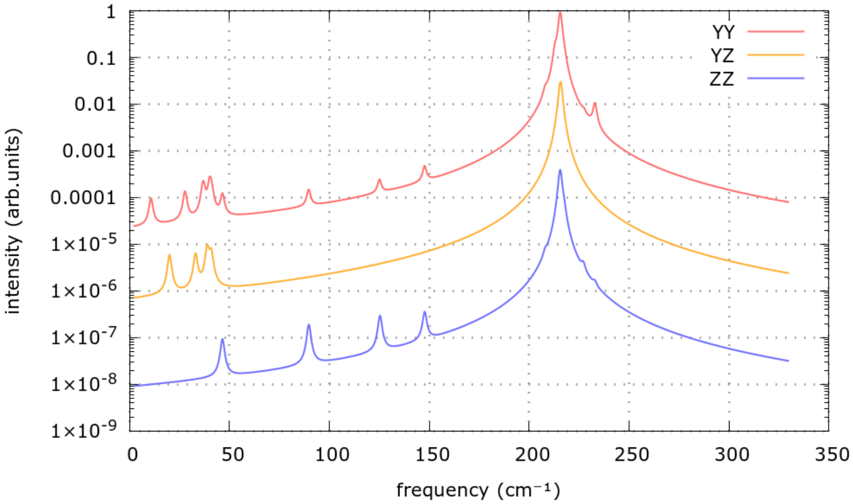

Figure 4.13: Raman spectrum of the 6.26 nm InAs TSL for every nonequivalent polarization setup

Chapter 5

Conclusion

This thesis has undertaken a systematic investigation into the complex realm of nanoscale phonon transport across semiconductor interfaces. By integrating advanced simulation techniques with first-principles calculations, the work addresses both the fundamental mechanisms governing thermal boundary resistance (TBR) and the practical implications for next-generation electronic and optoelectronic devices.

At the heart of this research lies the exploration of single-interface systems, exemplified by the GaAs/Ge heterojunction. Using nonequilibrium molecular dynamics (NEMD) simulations with a bond-order potential of the Tersoff type, Chapter 2 revealed that the thermal transport properties are exquisitely sensitive to the interface's atomic-scale features. Detailed analyses showed that even minor deviations from an ideal, atomically flat interface—such as chemical intermixing, graded compositions, or surface roughness—can lead to pronounced changes in phonon scattering and, consequently, the TBR. The work further demonstrated that the interplay between coherent and diffusive phonon transport is governed by both the physical dimensions of the system and the temperature-dependent anharmonicity of the lattice vibrations. In this regime, classical Fourier's law ceases to hold, and coherence effects become critical for an accurate description of heat flow.

Building on these insights, Chapter 3 extended the investigation to multiple-interface systems, including superlattice nanowires and bulk superlattice structures. By simulating Silicon/Germanium superlattices, the research uncovered that the cumulative effect of numerous interfaces can either enhance or impede overall thermal transport depending on their arrangement and periodicity. Notably, the phenomenon of thermal rectification emerged as a key finding; the directional dependence of heat flow was shown to be highly sensitive to both the interfacial composition and the geometrical parameters of the device. Under carefully engineered conditions, thermal rectification ratios approaching 30% were observed—an encouraging result for the design of thermal diodes and devices that require directional heat management. These results not only validate existing theoretical models of phonon scattering and interference but also provide practical design guidelines for tailoring thermal properties in complex semiconductor systems.

Chapter 4 brought an additional dimension to the thesis by delving into the electro-optical properties of GaAs/GaP superlattices and InAs twinning superlattices. Through the use of density functional theory (DFT) and density functional perturbation theory (DFPT), this section explored the vibrational spectra and Raman responses of these materials. The ab initio calculations yielded detailed phonon dispersion relations and allowed for a precise determination of the vibrational modes that contribute to heat transport. Importantly, the integrated study of thermal and optical properties underscored the possibility of designing multifunctional materials that not only manage heat efficiently but also exhibit desirable optical characteristics for applications in optoelectronics and photonics. This holistic approach reinforces the idea that thermal and electronic properties are deeply intertwined at the nanoscale, and that advancements in one area can drive innovations in the other. A recurring theme throughout the thesis is the critical importance of scale. As electronic devices shrink, classical descriptions of heat conduction give way to phenomena where quantum effects, interfacial disorder, and finite-size limitations become dominant. The results of this work emphasize that achieving reliable thermal management in nanoscale systems requires a nuanced understanding of these effects. In particular, the demonstrated sensitivity of TBR to interface morphology and temperature suggests that precise atomic-scale engineering is essential for optimizing device performance. Moreover, the integration of NEMD simulations with first-principles methods sets a new standard for modeling such systems, offering a robust framework that can be extended to more complex, multi-material architectures.

The methodologies developed here represent significant progress in computational materials science. By combining classical molecular dynamics with quantum mechanical calculations, this research bridges the gap between macroscopic thermal theories and the microscopic behavior of phonons. Future advancements, particularly those leveraging machine-learned interatomic potentials, promise to further enhance the predictive power of these simulations—especially in regimes where quantum effects play a pivotal role. Such improvements will be critical for the next generation of electronic and thermoelectric devices, where efficient heat dissipation is paramount.

Looking forward, several promising directions for future research emerge from the findings of this thesis. First, the exploration of alternative semiconductor material combinations could uncover systems with even more advantageous thermal management properties. Second, further refinement of interatomic potentials—possibly through the integration of machine learning techniques—could yield more accurate predictions, particularly at low temperatures where classical approximations begin to falter. Finally, experimental validation of these theoretical predictions will be essential. Collaborative efforts between computational researchers and experimentalists will help to translate these insights into practical device improvements.

In summary, the contributions of this thesis are multifaceted. It deepens our fundamental understanding of nanoscale phonon transport by elucidating the roles of interface morphology, temperature, and finite-size effects. It demonstrates that the control of TBR through careful design of semiconductor interfaces can lead to significant improvements in device performance, including the potential for directional heat management. And it lays a robust computational foundation for future studies, highlighting the promise of advanced simulation techniques in unraveling the complex physics of thermal transport. Through these achievements, this work paves the way for innovative approaches to thermal management in modern electronics, ultimately contributing to the development of more efficient, reliable, and multifunctional semiconductor technologies.

Published Papers

- GaAs/GaP Superlattice Nanowires for Tailoring Phononic Properties at the Nanoscale: Implications for Thermal Engineering
  Authors: K. Sivan, Aswathi and Abad, Begoña and Albrigi, Tommaso and Arif, Omer and Trautvetter, Johannes and Ruiz Caridad, Alicia and Arya, Chaitanya and Zannier, Valentina and Sorba, Lucia and Rurali, Riccardo and Zardo, Ilaria.
  ACS *Applied Nano Materials* - Vol. 6, Num. 19, Pagg. 18602-18613 - Year 2023 - doi: 10.1021/acsanm.3c04245

- Phonon transport across GaAs/Ge heterojunctions by nonequilibrium molecular dynamics
  Authors: Albrigi, Tommaso and Rurali, Riccardo.
  ACS *Applied Physics Letters* - Vol. 124, Num. 10, Pagg. 102203 - Year 2024 - doi: 10.1063/5.0191692

Numerical Tables

Table 5.1: Parameters for GaAs, Ge, and GaAs-Ge, obtained applying Tersoff recipe for mixing Tersoff parameters for Ge with Norlund parameters for GaAs.

	GaAs	**Ge**	**Mixed**
A (eV)	2.543×10^3	1.769×10^3	2.156×10^3
B (eV)	3.1446×10^2	4.1923×10^2	3.6308×10^2
λ (Å^{-1})	2.8280	2.4451	2.6366
μ (Å^{-1})	1.7230	1.7047	1.7139
β	3.57192×10^{-1}	9.0166×10^{-7}	–
n	6.31741	7.5627×10^{-1}	–
c	1.226302	1.0643×10^5	–
d	7.90396×10^{-1}	1.5652×10^1	–
h	-5.18489×10^{-1}	-4.3884×10^{-1}	–
R (Å)	3.4	2.8	3.08
S (Å)	3.6	3.1	3.34

Table 5.2: TBR values for the atomically flat GaAs/Ge junction with constant ΔT for different values of the cross section. Values are expressed in K m^2/W.

L (nm)	**8 nm^2**	**11.5 nm^2**	**15.6 nm^2**
60	4.01E-10	3.88E-10	3.98E-10
100	2.21E-10	2.60E-10	2.77E-10
140	2.12E-10	2.26E-10	2.47E-10
180	1.69E-10	1.87E-10	1.82E-10
220	1.92E-10	1.72E-10	1.49E-10
260	1.36E-10	1.79E-10	1.49E-10
300	1.87E-10	1.48E-10	1.18E-10

Table 5.3: TBR values for the atomically flat GaAs/Ge junction with constant ∇T for different values of the cross section. Values are expressed in K m^2/W.

L (nm)	**8 nm^2**	**11.5 nm^2**	**15.6 nm^2**
60	4.01E-10	3.88E-10	3.98E-10
100	2.66E-10	2.78E-10	2.76E-10
140	2.27E-10	2.16E-10	2.24E-10
180	1.96E-10	2.08E-10	1.87E-10
220	1.77E-10	1.96E-10	1.78E-10
260	1.74E-10	1.77E-10	1.73E-10
300	1.65E-10	1.70E-10	1.60E-10

Table 5.4: TBR values for the 180 nm × 8 nm^2 and 260 × 8 nm^2 atomically flat GaAs/Ge junction, for different values of the average temperature. Values are expressed in K m^2/W.

T (K)	**180 nm**	**260 nm**
220	2.38E-10	1.89E-10
240	2.21E-10	-
260	2.11E-10	1.92E-10
280	1.83E-10	-
300	1.89E-10	1.47E-10
320	1.89E-10	-
340	1.44E-10	1.36E-10
360	1.64E-10	-
380	1.48E-10	1.45E-10
400	1.31E-10	-
420	1.06E-10	1.54E-10
440	1.36E-10	-

Table 5.5: TBR values for the 180 nm × 8 nm^2 GaAs/Ge junction with chemical mixing, for different mixing styles. Values are expressed in K m^2/W.

L_{mix} (nm)	**linear**	**soft exp.**	**hard exp.**
1	1.79E-10	1.81E-10	1.54E-10
2	2.03E-10	1.65E-10	2.06E-10
3	1.74E-10	1.96E-10	1.84E-10
4	1.86E-10	2.00E-10	2.05E-10
5	2.20E-10	1.97E-10	1.85E-10
7.5	2.62E-10	2.15E-10	2.41E-10
10	2.71E-10	2.65E-10	3.01E-10

Table 5.6: TBR values for the 180 nm × 8 nm^2 GaAs/Ge junction with surface roughness, for different seeds and RMS. Values are expressed in K m^2/W.

RMS (nm)	**TBR**	**RMS (nm)**	**TBR**
0.40	2.03E-10	0.39	1.67E-10
0.81	1.91E-10	0.82	1.65E-10
1.26	1.69E-10	1.10	1.96E-10

Table 5.7: Values of κ for the atomically flat, 8 nm^2 GaAs/Ge junction in the forward and reverse bias configurations. Values are expressed in W/m K.

L (nm)	**forward**	**reverse**
60	18.9	19.7
100	29.7	30.4
140	37.7	37.9
180	44.7	43.6
220	51.5	50.0
260	58.5	55.3
300	67.8	62.6

Table 5.8: Values of the TBR for the Si/Ge nanowire heterojunction, with 120 nm length and 5 nm diameter, for both the tight and loose interfacial configurations. Values are expressed in K m^2/W.

coupling	**TBR**
tight	1.68E-09
loose	2.02E-09

Table 5.9: Values of κ for the Si/Ge superlattice nanowire, with 120 nm length and 5 nm diameter, for both the tight and loose interfacial configurations. Values are expressed in W/m K.

SL period (nm)	**tight**	**loose**
1.9	3.3	2.5
3.8	3.0	2.4
5.8	3.2	2.6
7.7	3.5	2.9
9.6	3.7	3.0
11.5	3.9	3.4

Table 5.10: Values of κ for the Si/Ge superlattice nanowire, with 120 nm length and 5 nm diameter, for the free interfacial configuration. Values are expressed in W/m K.

SL period (nm)	**free**
1	1.0
2	1.4
3	1.6
4	1.9
5	2.1
6	2.3
7	2.6
8	2.8
9	3.0
10	3.1
11	3.2
12	3.4

Table 5.11: Values of κ for the [100] Si/Ge superlattice nanowire, with 120 nm length and 5 nm diameter. Values are expressed in W/m K.

SL period (nm)	**free**
1.1	2.4
2.2	1.8
3.3	1.8
4.4	2.0
6.6	2.3
8.9	2.7
11.1	3.0
13.3	3.2

Table 5.12: Values of κ for the [111] Si/Ge bulk superlattice as a function of the k-points grid number, computed at different temperatures with almaBTE. Values are expressed in K and W/m K.

kpts (#)	**100**	**200**	**300**	**400**	**500**	**600**	**700**	**800**	**900**	**1000**
10	41.4	21.8	16.8	14.2	12.5	11.3	10.3	9.6	8.9	8.4
14	56.8	28.2	21.0	17.4	15.0	13.4	12.1	11.1	10.3	9.6
20	43.8	25.0	20.0	17.1	15.2	13.8	12.7	11.7	11.0	10.3
24	43.7	24.1	19.2	16.5	14.6	13.3	12.2	11.3	10.6	10.0

Table 5.13: Values of κ for the [111] Si/Ge bulk superlattice as a function of the superlattice period p, computed at different temperatures with almaBTE. Values are expressed in K and W/m K.

p (nm)	**100**	**200**	**300**	**400**	**500**	**600**	**700**	**800**	**900**	**1000**
1.9	43.7	24.1	19.2	16.5	14.6	13.3	12.2	11.3	10.6	10.0
3.8	35.6	17.3	13.5	11.4	10.1	9.1	8.4	7.8	7.3	6.9
5.8	34.4	16.5	12.7	10.7	9.4	8.5	7.8	7.2	6.8	6.4
9.6	33.6	16.4	12.5	10.5	9.2	8.3	7.6	7.0	6.6	6.2
11.5	37.3	17.7	13.5	11.4	10.0	9.0	8.2	7.6	7.1	6.6
19.2	36.7	18.1	13.9	11.7	10.3	9.3	8.5	7.8	7.3	6.8

Table 5.14: Values of κ for the [100] Si/Ge bulk superlattice with sharp interfaces, as a function of the superlattice period, computed at different temperatures with almaBTE within the RTA, plus one batch computed solving the full BTE at 100 K. Values are expressed in K and W/m K.

period (nm)	**100 (BTE)**	**100**	**300**	**500**
1.1	43.4	40.5	17.6	13.1
2.2	40.4	43.9	17.4	12.8
3.3	42.2	42.1	16.6	12.2
5.5	43.4	43.3	16.6	12.1
6.6	41.1	40.3	17.6	12.8
11.1	42.0	41.8	18.2	13.2

Table 5.15: Values of κ for the [111] Si/Ge bulk superlattice with rough interfaces, as a function of the superlattice period, computed at different temperatures with almaBTE. Values are expressed in K and W/m K.

period (nm)	**100**	**300**	**500**	**900**
1.9	43.7	19.2	14.6	10.6
3.8	35.6	13.5	10.1	7.3
5.8	2.9	2.8	2.6	2.3
9.6	3.5	3.3	3.0	2.5
11.5	3.9	3.7	3.3	2.9
19.2	5.8	4.9	4.3	3.6

Table 5.16: Values of κ for the [100] Si/Ge bulk superlattice with rough interfaces, as a function of the superlattice period p, computed at different temperatures with almaBTE. Values are expressed in K and W/m K.

period (nm)	**100**	**300**	**500**
1.1	40.5	17.6	13.1
2.2	43.9	17.4	12.8
3.3	2.9	2.8	2.6
5.5	3.7	3.4	3.1
6.6	4.3	3.9	3.5
11.1	6.2	5.3	4.7

Table 5.17: Values of κ for the [100] Si/Ge bulk superlattice as a function of the superlattice period p, computed for different cell geometries using LAMMPS. Values are expressed in nm and W/m K.

period (nm)	**180 x 8 nm3**	**120 x 15 nm3**	**120 x 8 nm3**
1.1	13.7	17.1	14.1
2.2	10.1	14.1	11.2
3.3	9.6	12.5	10.3
4.4	9.3	12.2	10.2
5.5	8.4	12.9	10.6
6.6	8.9	12.2	9.4
8.9	9.9	12.3	9.4
10	9.3	11.8	9.1
11.1	9	13	10.2
13.3	8.4	12.9	8.5
15.5	9.6	12.3	9.2
17.7	9.5	13.2	10.4
19.9	10.6	11.5	10.6
22.2	9.2	14.1	9.7
28.8	9.5	13.2	9.8
38.8	11.3	15.2	11.1
54.3	13.4	17.3	14.2

Table 5.18: Phonon frequencies of GaAs and GaP wurtzites, computed at 37 Ha using a $8 \times 8 \times 5$ k-points grid. Values are expressed in cm^{-1}.

GaAs	**GaP**
55.2	75.7
55.2	75.7
206.5	232.4
238.4	356.8
258.8	356.8
258.8	362.7
267.5	366.0
269.9	374.1
284.5	393.7

Table 5.19: Phonon frequencies of GaAs/GaP SL with 1.28 nm period, for the YY, YZ, and ZZ setup respectively. Phonon modes with a Raman intensity more than 100 times smaller than that of the most intense mode were considered nondetectable. Values are expressed in cm^{-1} and a.u.

ν	**I**	ν	**I**	ν	**I**
145.1	1.44E-05	283.4	1.37E-05	145.1	1.12E-05
148.4	1.66E-06	341.6	1.00E-06	258.8	1.21E-05
258.8	7.97E-06	361.6	2.40E-05	277.5	9.40E-05
272.3	1.34E-04	-	-	363.8	8.84E-05
277.5	4.41E-05	-	-	-	-
341.6	3.53E-05	-	-	-	-

Table 5.20: Phonon frequencies of GaAs/GaP SL with 2.56 nm period, for the YY, YZ, and ZZ setup respectively. Values are expressed in cm^{-1} and a.u.

ν	**I**	ν	**I**	ν	**I**
77.4	9.34E-06	273.2	8.68E-07	77.4	2.74E-06
251.3	2.89E-06	280.1	1.51E-05	195.4	2.03E-06
268.3	5.56E-06	339.6	2.68E-07	251.3	3.37E-06
271.5	1.77E-04	341.8	3.66E-07	268.3	1.62E-05
276.5	5.74E-06	345.2	9.25E-07	282.3	9.81E-05
282.3	4.94E-05	347.8	7.95E-06	283.4	1.19E-05
283.4	5.25E-05	-	-	366.2	7.97E-05
339.6	3.72E-05	-	-	369.3	8.54E-06
345.2	2.83E-06	-	-	375.5	1.09E-05
379.9	7.04E-06	-	-	-	-

Table 5.21: Phonon frequencies of GaAs/GaP SL with 3.83 nm period, for the YY, YZ, and ZZ setup respectively. Values are expressed in cm^{-1} and a.u.

ν	**I**	ν	**I**	ν	**I**
52.2	9.50E-06	272.0	3.01E-07	52.2	1.45E-06
271.3	2.59E-04	276.0	1.40E-06	145.4	9.87E-07
272.0	2.62E-06	280.9	2.61E-05	247.5	1.31E-06
273.6	6.98E-06	342.0	4.77E-07	259.9	3.66E-06
279.6	7.03E-05	344.4	9.03E-07	272.0	2.47E-06
285.1	9.39E-05	346.6	4.13E-07	279.6	8.13E-05
289.0	2.37E-05	348.2	8.86E-06	285.1	7.30E-05
339.2	3.56E-05	-	-	366.9	6.33E-05
342.0	4.49E-06	-	-	368.4	1.80E-05
374.8	2.73E-06	-	-	371.8	1.99E-05
382.8	9.81E-06	-	-	380.0	2.67E-06

Table 5.22: Phonon frequencies of GaAs/GaP SL with 5.12 nm period, for the YY, YZ, and ZZ setup respectively. Values are expressed in cm^{-1} and a.u.

ν	**I**	ν	**I**	ν	**I**
39.3	8.06E-06	273.9	3.55E-07	254.9	1.19E-06
54.6	2.89E-06	277.8	1.25E-06	264.7	1.17E-06
271.2	2.89E-04	281.2	2.63E-05	273.2	1.02E-05
272.5	7.38E-06	343.9	2.96E-07	281.1	8.30E-06
273.2	7.40E-06	345.8	7.97E-07	282.5	1.12E-04
282.5	1.59E-04	348.4	6.40E-06	288.1	1.58E-05
288.1	3.57E-05	-	-	367.3	3.13E-05
291.1	1.78E-05	-	-	368.1	2.16E-05
339.0	3.22E-05	-	-	370.2	2.35E-05
340.6	4.58E-06	-	-	372.1	2.74E-06
378.7	3.08E-06	-	-	375.9	4.37E-06
384.1	3.78E-06	-	-	-	-

Table 5.23: Phonon frequencies of GaAs/GaP SL with 6.39 nm period, for the YY, YZ, and ZZ setup respectively. Values are expressed in cm^{-1} and a.u.

ν	**I**	ν	**I**	ν	**I**
31.5	8.35E-06	275.6	4.66E-07	267.4	3.08E-06
54.6	4.11E-06	278.9	1.68E-06	279.8	4.77E-05
271.1	3.82E-04	281.3	3.97E-05	283.6	1.16E-04
272.0	1.02E-05	346.6	1.10E-06	290.0	6.76E-06
279.8	5.96E-05	348.5	6.53E-06	367.3	1.08E-05
283.6	1.85E-04	-	-	367.9	2.48E-05
285.7	1.18E-05	-	-	369.5	2.93E-05
290.0	2.00E-05	-	-	370.6	8.87E-06
292.1	2.64E-05	-	-	373.4	7.54E-06
339.0	3.24E-05	-	-	378.8	1.21E-06
340.0	4.40E-06	-	-	-	-
381.1	4.60E-06	-	-	-	-
384.9	4.02E-06	-	-	-	-

Table 5.24: Phonon frequencies of InAs TSL with 2.09 nm period, for the YY, YZ, and ZZ setup respectively. Values are expressed in cm^{-1} and a.u.

ν	**I**	ν	**I**	ν	**I**
213.4	4.35E-02	213.3	1.56E-04	214.8	8.17E-04
214.8	7.64E-02	215.9	3.43E-04	217.8	2.32E-04
215.8	2.31E-03	216.5	6.80E-03	-	-
216.2	7.43E-03	-	-	-	-
217.8	1.00E-02	-	-	-	-

Table 5.25: Phonon frequencies of InAs TSL with 4.17 nm period, for the YY, YZ, and ZZ setup respectively. Values are expressed in cm^{-1} and a.u.

ν	**I**	ν	**I**	ν	**I**
213.1	1.93E-02	213.1	7.38E-05	215.4	6.46E-04
215.4	7.52E-02	215.4	1.32E-04	217.6	7.58E-05
215.5	6.46E-03	215.6	5.01E-04	-	-
215.7	2.09E-02	215.8	1.04E-03	-	-
215.8	2.66E-03	216.1	4.95E-03	-	-
216.0	4.41E-03	-	-	-	-
217.6	4.72E-03	-	-	-	-

Table 5.26: Phonon frequencies of InAs TSL with 6.26 nm period, for the YY, YZ, and ZZ setup respectively. Values are expressed in cm^{-1} and a.u.

ν	**I**	ν	**I**	ν	**I**
213.0	2.83E-01	213.0	7.02E-04	215.5	1.22E-03
215.4	7.48E-02	215.4	8.31E-04	217.4	7.02E-05
215.5	2.10E+00	215.4	8.84E-04	-	-
215.6	5.79E-01	215.5	2.33E-02	-	-
215.7	4.66E-02	215.6	2.77E-02	-	-
215.9	5.32E-02	215.8	8.87E-03	-	-
217.4	7.27E-02	215.9	3.55E-02	-	-

Notation & Acronyms

Scalar quantities are represented using plain text - e.g. a. Vector quantities are represented using bold text - e.g. $\mathbf{a}$, except for gradients, for which the nabla notation has been preferred, and polarization, which is represented by the (possibly complex) vector ε. Scalar quantities derived from vector quantities are usually represented with the same symbol without the bold font. For example, if $\mathbf{Q}$ represents the heat flux, $Q = \mathbf{n} \cdot \mathbf{Q}$ represents the corresponding flux perpendicular to a given surface with normal $\mathbf{n}$, while $\cdot$ represents the scalar product between the two vectors. The corresponding equilibrium, steady state, and average quantities are adorned with a bar over them - e.g. $\bar{Q}$. Every quantity is followed by the corresponding units in the SI.

Notations

T	Temperature (K)
ΔT	Temperature drop, temperature bias (K)
∇T	Temperature gradient (K/m)
$\mathbf{Q}$	Heat flux (W)
κ	Thermal conductivity (W/m K)
l	Length over which temperature gradient is measured (m)
$\frac{d}{dT}$	Total derivative with respect to T (K^{-1})
R_I	Thermal Boundary Resistance (K m^2/W)
h_I	Interfacial Thermal Conductance (W/m^2 K)
c	Sound velocity (m/s); Parameter in angle-dependent function
C	Specific heat (J/kg K)
G	Thermal conductance (W/K)
ρ	Mass density (kg/m^3)
Z	Acoustic impedance (kg/m^2 s)
ζ	Transmission coefficient
ε	Polarization vector

τ	Phonon lifetime (s)
λ	Phonon wavelength (m)
$\mathbf{k}$	Phonon wavevector (m^{-1})
ω	Phonon angular frequency (rad/s)
ϵ	Phonon energy (J)
ν	Phonon frequency (s^{-1})
$\omega(\mathbf{k})$	Phonon dispersion relation (rad/s)
$\frac{\partial \omega_{\mathbf{k}\varepsilon}}{\partial \mathbf{k}}$	Phonon group velocity (m/s)
k_B	Boltzmann constant (J/K)
E	Energy (J)
E_k	Kinetic energy (J)
V	Total volume (m^3)
$\hbar$	Reduced Planck constant (J s)
$n(\epsilon, T)$	Phonon distribution function
$\mathbf{n}$	Unit vector normal to the interface
ω_D	Debye frequency (rad/s)
I_ε	Integral of $\zeta(\theta, \varepsilon)$ over all incident angles
m_i	Mass of particle i (kg)
$\mathbf{r}_i$	Position vector of particle i (m)
$\mathbf{v}_i$	Velocity vector of particle i (m/s)
$\mathbf{F}_i$	Net force acting on particle i (N)
$U(\mathbf{r}_1, \mathbf{r}_2, ..., \mathbf{r}_N)$	Potential energy function (J)
r_{ij}	Distance between particles i and j (m)
$V(r_{ij})$	Pairwise potential energy between particles i and j (J)
$f_R(r_{ij})$	Repulsive interaction term (J)
$f_A(r_{ij})$	Attractive interaction term (J)
$f_C(r_{ij})$	Cutoff function
A_{ij}	Parameter for repulsive term (J)
B_{ij}	Parameter for attractive term (J)
σ_{ij}	Parameter related to repulsive term (m^{-1})
μ_{ij}	Parameter related to attractive term (m^{-1})
R_{ij}	Cutoff radius (m)
S_{ij}	Smooth cutoff radius (m)
b_{ij}	Bond order term
θ_{ijk}	Bond angle between bonds ij and ik (rad)
$g(\theta_{ijk})$	Angle-dependent function
d	Parameter in angle-dependent function

h	Parameter in angle-dependent function
χ_{ij}	Heteropolar bond strength parameter
α	Scaling factor for velocity
Λ	Phonon MFP (m)
γ	Thermal rectification coefficient

Acronyms

QM	Quantum Mechanics
TBR	Thermal Boundary Resistance (K m^2/W)
ITR	Interfacial Thermal Resistance (K m^2/W)
ITC	Interfacial Thermal Conductance (W/m^2 K)
MFP	Mean Free Path (m)
PBC	Periodic Boundary Conditions
FCC	Face Centered Cubic
AMM	Acoustic Mismatch Model
DMM	Diffuse Mismatch Model
MD	Molecular Dynamics
NEMD	Nonequilibrium Molecular Dynamics
NESS	Nonequilibrium Steady-State
RMS	Root Mean Square
BTE	Boltzmann Transport Equation
RTA	Relaxation Time Approximation
DFT	Density Functional Theory
LED	Light Emitting Diode
IC	Integrated Circuit
RF	Radio Frequency
RT	Room Temperature
HBT	Heterojunction Bipolar Transistor
CMOS	Complementary Metal-Oxide Semiconductor
ZB	Zincblende
WZ	Wurtzite

Acknowledgements

I acknowledge the support provided by ICMAB-CSIC throughout the course of my research on nanoscale thermal transport across semiconductor interfaces. I extend my thanks to my supervisor and PI, Riccardo Rurali, for his clear guidance and constructive feedback throughout the project. I also recognize the CESGA supercomputing facility and its staff for providing reliable computational resources and technical assistance that were essential to the computational aspects of this work.

My gratitude extends to the Universitat Autònoma de Barcelona (UAB) for their support, as well as to the NMHT conference network for offering a valuable platform for the exchange of ideas. I also appreciate the contributions of the broader thermal transport scientific community, whose collective efforts and discussions have enriched the context and impact of my research.

Bibliography

[1] David G. Cahill, Paul V. Braun, Gang Chen, David R. Clarke, Shanhui Fan, Kenneth E. Goodson, Pawel Keblinski, William P. King, Gerald D. Mahan, Arun Majumdar, Humphrey J. Maris, Simon R. Phillpot, Eric Pop, and Li Shi. Nanoscale thermal transport. ii. 2003–2012. *Applied Physics Reviews*, 1(1):011305, 01 2014. ISSN 1931-9401. doi: 10.1063/1.4832615.

[2] Joseph Fourier. *Théorie analytique de la chaleur*. Didot, 1822.

[3] Martin Maldovan. Sound and heat revolutions in phononics. *Nature*, 503(7475):209–217, 2013. doi: https://doi.org/10.1038/nature12608.

[4] A. Balandin Alexander and L. Nika Denis. Phononics in low-dimensional materials. *Materials Today*, 15(6):266–275, 2012. ISSN 1369-7021. doi: https://doi.org/10.1016/S1369-7021(12)70117-7.

[5] Maria N. Luckyanova, Jivtesh Garg, Keivan Esfarjani, Adam Jandl, Mayank T. Bulsara, Aaron J. Schmidt, Austin J. Minnich, Shuo Chen, Mildred S. Dresselhaus, Zhifeng Ren, Eugene A. Fitzgerald, and Gang Chen. Coherent phonon heat conduction in superlattices. *Science*, 338 (6109):936–939, 2012. doi: 10.1126/science.1225549.

[6] Simeon Denis Poisson. *Théorie mathématique de la chaleur*. Paris, Bachelier, 1835.

[7] Marian Smoluchowski. Über wärmeleitung in verdünnten gasen. *Annalen der Physik*, 299(1):101–130, 1898. doi: https://doi.org/10.1002/andp.18983000110.

[8] P. L. Kapitza. Heat transfer and superfluidity of helium ii. *Phys. Rev.*, 60:354–355, Aug 1941. doi: 10.1103/PhysRev.60.354.

[9] GERALD L. POLLACK. Kapitza resistance. *Rev. Mod. Phys.*, 41: 48–81, Jan 1969. doi: 10.1103/RevModPhys.41.48.

[10] E. T. Swartz and R. O. Pohl. Thermal boundary resistance. *Rev. Mod. Phys.*, 61:605–668, Jul 1989. doi: 10.1103/RevModPhys.61.605.

[11] Jie Chen, Xiangfan Xu, Jun Zhou, and Baowen Li. Interfacial thermal resistance: Past, present, and future. *Rev. Mod. Phys.*, 94:025002, Apr 2022. doi: 10.1103/RevModPhys.94.025002.

[12] I. M. Khalatnikov. Acoustic properties of solid surfaces and their interaction with phonons. *Journal of Physics USSR*, 8(1):13–24, 1952.

[13] G. L. Eesley. Observation of nonequilibrium electron heating in copper. *Phys. Rev. Lett.*, 51:2140–2143, Dec 1983. doi: 10.1103/PhysRevLett.51.2140.

[14] Wei Liu and Arun Majumdar. Nanoscale thermal transport: from fourier's law to phonon-interface conductance. *Nanoscale and Microscale Thermophysical Engineering*, 18(1):48–66, 2014.

[15] David G. Cahill, Henry E. Fischer, Tom Klitsner, E. T. Swartz, and R. O. Pohl. Thermal conductivity of thin films: Measurements and understanding. *Journal of Vacuum Science & Technology A*, 7(3):1259–1266, 05 1989. ISSN 0734-2101. doi: 10.1116/1.576265.

[16] Patrick E. Hopkins, Charles M. Reinke, Mehmet F. Su, Roy H. III Olsson, Eric A. Shaner, Zayd C. Leseman, Justin R. Serrano, Leslie M. Phinney, and Ihab El-Kady. Reduction in the thermal conductivity of single crystalline silicon by phononic crystal patterning. *Nano Letters*, 11(1):107–112, 2011. doi: 10.1021/nl102918q. PMID: 21105717.

[17] E. T. Swartz and R. O. Pohl. Thermal resistance at interfaces. *Applied Physics Letters*, 51(26):2200–2202, 12 1987. ISSN 0003-6951. doi: 10.1063/1.98939.

[18] Jian-Sheng Wang, Jian Wang, and Nan Zeng. Nonequilibrium green's function approach to mesoscopic thermal transport. *Phys. Rev. B*, 74: 033408, Jul 2006. doi: 10.1103/PhysRevB.74.033408.

[19] J. S. Blakemore. Semiconducting and other major properties of gallium arsenide. *Journal of Applied Physics*, 53(10):R123–R181, 10 1982. ISSN 0021-8979. doi: 10.1063/1.331665.

[20] R.L. Anderson. Experiments on ge-gaas heterojunctions. *Solid-State Electronics*, 5(5):341–351, 1962. ISSN 0038-1101. doi: https://doi.org/10.1016/0038-1101(62)90115-6.

[21] Rienk E. Algra, Moïra Hocevar, Marcel A. Verheijen, Ilaria Zardo, George G. W. Immink, Willem J. P. van Enckevort, Gerhard Abstreiter, Leo P. Kouwenhoven, Elias Vlieg, and Erik P. A. M. Bakkers. Crystal structure transfer in core/shell nanowires. *Nano Letters*, 11(4):1690–1694, 2011. doi: 10.1021/nl200208q. PMID: 21417242.

[22] Håkon Ikaros T. Hauge, Sonia Conesa-Boj, Marcel A. Verheijen, Sebastian Koelling, and Erik P. A. M. Bakkers. Single-crystalline hexagonal silicon–germanium. *Nano Letters*, 17(1):85–90, 2017. doi: 10.1021/acs.nanolett.6b03488. PMID: 28001429.

[23] E. M. T. Fadaly et al. Direct-bandgap emission from hexagonal ge and sige alloys. *Nature*, 580:205–209, 2020. doi: https://doi.org/10.1038/s41586-020-2150-y.

[24] Ashutosh Giri and Patrick E. Hopkins. A review of experimental and computational advances in thermal boundary conductance and nanoscale thermal transport across solid interfaces. *Advanced Functional Materials*, 30(8):1903857, 2020. doi: https://doi.org/10.1002/adfm.201903857.

[25] Riccardo Rurali, Luciano Colombo, Xavier Cartoixà, Øivind Wilhelmsen, Thuat T. Trinh, Dick Bedeaux, and Signe Kjelstrup. Heat transport through a solid–solid junction: the interface as an autonomous thermodynamic system. *Phys. Chem. Chem. Phys.*, 18:13741–13745, 2016. doi: 10.1039/C6CP01872F.

[26] Riccardo Rurali, Xavier Cartoixà, Dick Bedeaux, Signe Kjelstrup, and Luciano Colombo. The thermal boundary resistance at semiconductor interfaces: a critical appraisal of the onsager vs. kapitza formalisms. *Phys. Chem. Chem. Phys.*, 20:22623–22628, 2018. doi: 10.1039/C8CP02104J.

[27] Jesús Carrete, Miquel López-Suárez, Martí Raya-Moreno, Anton S. Bochkarev, Miquel Royo, Georg K. H. Madsen, Xavier Cartoixà, Natalio Mingo, and Riccardo Rurali. Phonon transport across crystal-phase interfaces and twin boundaries in semiconducting nanowires. *Nanoscale*, 11:16007–16016, 2019. doi: 10.1039/C9NR05274G.

[28] J. Tersoff. Modeling solid-state chemistry: Interatomic potentials for multicomponent systems. *Phys. Rev. B*, 39:5566–5568, Mar 1989. doi: 10.1103/PhysRevB.39.5566.

[29] Aidan P. Thompson, H. Metin Aktulga, Richard Berger, Dan S. Bolintineanu, W. Michael Brown, Paul S. Crozier, Pieter J. in 't Veld, Axel Kohlmeyer, Stan G. Moore, Trung Dac Nguyen, Ray Shan, Mark J. Stevens, Julien Tranchida, Christian Trott, and Steven J. Plimpton. Lammps - a flexible simulation tool for particle-based materials modeling at the atomic, meso, and continuum scales. *Computer Physics Communications*, 271:108171, 2022. ISSN 0010-4655. doi: https://doi.org/10.1016/j.cpc.2021.108171.

[30] K Nordlund, J Nord, J Frantz, and J Keinonen. Strain-induced kirkendall mixing at semiconductor interfaces. *Computational Materials Science*, 18(3):283–294, 2000. ISSN 0927-0256. doi: https://doi.org/10.1016/S0927-0256(00)00107-5.

[31] Spencer Wyant, Andrew Rohskopf, and Asegun Henry. Machine learned interatomic potentials for modeling interfacial heat transport in ge/gaas. *Computational Materials Science*, 200:110836, 2021. ISSN 0927-0256. doi: https://doi.org/10.1016/j.commatsci.2021.110836.

[32] Jiaxuan Xu, Yue Hu, Xiulin Ruan, Xinyu Wang, Tianli Feng, and Hua Bao. Nonequilibrium phonon transport induced by finite sizes: Effect of phonon-phonon coupling. *Phys. Rev. B*, 104:104310, Sep 2021. doi: 10.1103/PhysRevB.104.104310.

[33] *Modeling Nanoscale Thermal Transport via the Boltzmann Transport Equation*, volume Electronic and Photonic Packaging, Electrical Systems Design and Photonics, and Nanotechnology of *ASME International Mechanical Engineering Congress and Exposition*, 11 2004. doi: 10.1115/IMECE2004-62508.

[34] *Effect of Phonon Dispersion on Transport Properties of Single-Crystalline Dielectrics*, volume Electronic and Photonic Packaging, Electrical Systems Design and Photonics, and Nanotechnology of *ASME International Mechanical Engineering Congress and Exposition*, 11 2004. doi: 10.1115/IMECE2004-62244.

[35] Saad Bin Mansoor and Bekir Sami Yilbas. Phonon transport in silicon–silicon and silicon–diamond thin films: Consideration of thermal boundary resistance at interface. *Physica B-condensed Matter*, 406: 2186–2195, 2011.

[36] Roberto Grassi, Stefano Poli, Susanna Reggiani, Elena Gnani, Antonio Gnudi, and Giorgio Baccarani. Phonon-scattering effects in cnt-fets with different dimensions and dielectric materials. *Solid-State Electronics*, 52(9):1329–1335, 2008. ISSN 0038-1101. doi: https://doi.org/10.1016/j.sse.2008.04.010. Papers Selected from the 37th European Solid-State Device Research Conference - ESSDERC'07.

[37] A. Majumdar. Microscale heat conduction in dielectric thin films. *Journal of Heat Transfer*, 115(1):7–16, 02 1993. ISSN 0022-1481. doi: 10.1115/1.2910673.

[38] *Ballistic-Diffusive Approximation for Phonon Transport Accounting for Polarization and Dispersion*, volume Heat Transfer: Volume 1 of *Heat Transfer Summer Conference*, 07 2003. doi: 10.1115/HT2003-47491.

[39] Sreekant V. J. Narumanchi, Jayathi Y. Murthy, and Cristina H. Amon. Submicron heat transport model in silicon accounting for phonon dispersion and polarization. *Journal of Heat Transfer*, 126(6):946–955, 01 2005. ISSN 0022-1481. doi: 10.1115/1.1833367.

[40] *Ballistic-Diffusive Approximation for Phonon Transport Accounting for Polarization and Dispersion*, volume Heat Transfer: Volume 1 of *Heat Transfer Summer Conference*, 07 2003. doi: 10.1115/HT2003-47491.

[41] Reza Karimi Kelayeh, Ali Rajabpour, Ehsan Taheran, and Yaser Bahari. Optimization of interfacial mixing for thermal transport along si/ge heterostructures: A molecular dynamics study. *Applied Surface Science*, 626:157236, 2023. ISSN 0169-4332. doi: https://doi.org/10.1016/j.apsusc.2023.157236.

[42] David G. Cahill, Wayne K. Ford, Kenneth E. Goodson, Gerald D. Mahan, Arun Majumdar, Humphrey J. Maris, Roberto Merlin, and Simon R. Phillpot. Nanoscale thermal transport. *Journal of Applied Physics*, 93(2):793–818, 01 2003. ISSN 0021-8979. doi: 10.1063/1.1524305.

[43] B. Yang, J. L. Liu, K. L. Wang, and G. Chen. Simultaneous measurements of seebeck coefficient and thermal conductivity across superlattice. *Applied Physics Letters*, 80(10):1758–1760, 03 2002. ISSN 0003-6951. doi: 10.1063/1.1458693.

[44] Patrick E. Hopkins. Thermal transport across solid interfaces with nanoscale imperfections: Effects of roughness, disorder, dislocations, and bonding on thermal boundary conductance. *International Scholarly Research Notices*, 2013(1):682586, 2013. doi: https://doi.org/10.1155/2013/682586.

[45] M. Terraneo, M. Peyrard, and G. Casati. Controlling the energy flow in nonlinear lattices: A model for a thermal rectifier. *Phys. Rev. Lett.*, 88: 094302, Feb 2002. doi: 10.1103/PhysRevLett.88.094302.

[46] N.A. Roberts and D.G. Walker. A review of thermal rectification observations and models in solid materials. *International Journal of Thermal Sciences*, 50(5):648–662, 2011. ISSN 1290-0729. doi: https://doi.org/10.1016/j.ijthermalsci.2010.12.004.

[47] C. Dames. Solid-state thermal rectification with existing bulk materials. *Journal of Heat Transfer*, 131(6):061301, 03 2009. ISSN 0022-1481. doi: 10.1115/1.3089552.

[48] Miquel López-Suárez, Miquel Royo, and Riccardo Rurali. Interface-driven thermal rectification in nanoscale systems. *Phys. Rev. Mater.*, 2: 113001, Nov 2018. doi: 10.1103/PhysRevMaterials.2.113001.

[49] D. P. Sellan, E. S. Landry, J. E. Turney, A. J. H. McGaughey, and C. H. Amon. Size effects in molecular dynamics thermal conductivity predictions. *Phys. Rev. B*, 81:214305, Jun 2010. doi: 10.1103/PhysRevB.81.214305.

[50] Patrick K. Schelling, Simon R. Phillpot, and Pawel Keblinski. Comparison of atomic-level simulation methods for computing thermal conductivity. *Phys. Rev. B*, 65:144306, Apr 2002. doi: 10.1103/PhysRevB.65.144306.

[51] Scott Huxtable, David Cahill, Sergei Shenogin, Liping Xue, Paul Barone, Monica Usrey, Michael Strano, Giles Siddons, Moonsub Shim, and Pawel Keblinski. Interfacial heat flow in carbon nanotube suspensions. *Nature materials*, 2:731–4, 12 2003. doi: 10.1038/nmat996.

[52] G. Chen. Thermal conductivity and ballistic-phonon transport in the cross-plane direction of superlattices. *Phys. Rev. B*, 57:14958–14973, Jun 1998. doi: 10.1103/PhysRevB.57.14958.

[53] Ming-Shan Jeng, Ronggui Yang, David Song, and Gang Chen. Modeling the thermal conductivity and phonon transport in nanoparticle composites using monte carlo simulation. *Journal of Heat Transfer*, 130 (4):042410, 03 2008. ISSN 0022-1481. doi: 10.1115/1.2818765.

[54] Ming-Hui Lu. Heat transfer in nanostructured materials. *Nanomaterials*, 13(6), 2023. ISSN 2079-4991. doi: 10.3390/nano13061062. URL `https://www.mdpi.com/2079-4991/13/6/1062`.

[55] Sandip Mazumder and Arunava Majumdar. Monte carlo study of phonon transport in solid thin films including dispersion and polarization. *Journal of Heat Transfer*, 123(4):749–759, 01 2001. ISSN 0022-1481. doi: 10.1115/1.1377018.

[56] R. Venkatasubramanian, E. Siivola, T. Colpitts, and B. O'Quinn. Thin-film thermoelectric devices with high room-temperature figures of merit. *Nature*, 413:597–602, 2001. doi: https://doi.org/10.1038/35098012.

[57] Jie Zou and Alexander Balandin. Phonon heat conduction in a semiconductor nanowire. *Journal of Applied Physics*, 89(5):2932–2938, 03 2001. ISSN 0021-8979. doi: 10.1063/1.1345515.

[58] P. K. Misra. *Physics of Condensed Matter*, volume 1. Academic Press, 2011. ISBN 978-0-12-384954-0. doi: https://doi.org/10.1016/C2010-0-65289-8.

[59] Friedrich Schäffler. High-mobility si and ge structures. *Semiconductor Science and Technology*, 12(12): 1515, dec 1997. doi: 10.1088/0268-1242/12/12/001. URL `https://dx.doi.org/10.1088/0268-1242/12/12/001`.

[60] Dietmar Kissinger, Gerhard Kahmen, and Robert Weigel. Millimeter-wave and terahertz transceivers in sige bicmos technologies. *IEEE Transactions on Microwave Theory and Techniques*, 69(10):4541–4560, 2021. doi: 10.1109/TMTT.2021.3095235.

[61] John D. Cressler. *SiGe and Si Strained-Layer Epitaxy for Silicon Heterostructure Devices.* CRC Press, 2010. doi: https://doi.org/10.1201/9781420066869. Pages 110-115.

[62] Jesús Carrete, Bjorn Vermeersch, Ankita Katre, Ambroise van Roekeghem, Tao Wang, Georg K.H. Madsen, and Natalio Mingo. almabte : A solver of the space–time dependent boltzmann transport equation for phonons in structured materials. *Computer Physics Communications*, 220:351–362, 2017. ISSN 0010-4655. doi: https://doi.org/10.1016/j.cpc.2017.06.023.

[63] X. Mu, L. Wang, and X. et al. Yang. Ultra-low thermal conductivity in si/ge hierarchical superlattice nanowire. *Scientific Reports*, 5:16697, 2015. doi: https://doi.org/10.1038/srep16697.

[64] Ming Hu and Dimos Poulikakos. Si/ge superlattice nanowires with ultralow thermal conductivity. *Nano Letters*, 12(11):5487–5494, 2012. doi: 10.1021/nl301971k. PMID: 23106449.

[65] Pengfei Ji, Yuwen Zhang, and Mo Yang. Structural, dynamic, and vibrational properties during heat transfer in si/ge superlattices: A car-parrinello molecular dynamics study. *Journal of Applied Physics*, 114 (23):234905, 12 2013. ISSN 0021-8979. doi: 10.1063/1.4850935.

[66] A. J. Minnich, J. A. Johnson, A. J. Schmidt, K. Esfarjani, M. S. Dresselhaus, K. A. Nelson, and G. Chen. Thermal conductivity spectroscopy technique to measure phonon mean free paths. *Phys. Rev. Lett.*, 107: 095901, Aug 2011. doi: 10.1103/PhysRevLett.107.095901.

[67] Meng An, Dongsheng Chen, Weigang Ma, Shiqian Hu, and Xing Zhang. Directly visualizing the crossover from incoherent to coherent phonons in

two-dimensional periodic mos2/mose2 arrayed heterostructure. *International Journal of Heat and Mass Transfer*, 178:121630, 2021. ISSN 0017-9310. doi: https://doi.org/10.1016/j.ijheatmasstransfer.2021.121630.

[68] Christopher J. Vineis, Ali Shakouri, Arun Majumdar, and Mercouri G. Kanatzidis. Nanostructured thermoelectrics: Big efficiency gains from small features. *Advanced Materials*, 22(36):3970–3980, 2010. doi: https://doi.org/10.1002/adma.201000839.

[69] A. J. Minnich, G. Chen, S. Mansoor, and B. S. Yilbas. Quasiballistic heat transfer studied using the frequency-dependent boltzmann transport equation. *Phys. Rev. B*, 84:235207, Dec 2011. doi: 10.1103/PhysRevB.84.235207.

[70] Joseph Callaway. Model for lattice thermal conductivity at low temperatures. *Phys. Rev.*, 113:1046–1051, Feb 1959. doi: 10.1103/PhysRev.113.1046.

[71] J.M. Ziman. *Electrons and Phonons: The Theory of Transport Phenomena in Solids*. Oxford University Press, 02 2001. ISBN 9780198507796. doi: 10.1093/acprof:oso/9780198507796.001.0001.

[72] Marco Drewes, Sebastián Mendizabal, and Christoph Weniger. The boltzmann equation from quantum field theory. *Physics Letters B*, 718(3):1119–1124, 2013. ISSN 0370-2693. doi: https://doi.org/10.1016/j.physletb.2012.11.046.

[73] C M Bhandari and D M Rowe. Boundary scattering of phonons. *Journal of Physics C: Solid State Physics*, 11(9):1787, may 1978. doi: 10.1088/0022-3719/11/9/017.

[74] C. T. Walker and R. O. Pohl. Phonon scattering by point defects. *Phys. Rev.*, 131:1433–1442, Aug 1963. doi: 10.1103/PhysRev.131.1433.

[75] Yan Wang, Zexi Lu, and Xiulin Ruan. First principles calculation of lattice thermal conductivity of metals considering phonon-phonon and phonon-electron scattering. *Journal of Applied Physics*, 119(22):225109, 06 2016. ISSN 0021-8979. doi: 10.1063/1.4953366.

[76] Ara Ghukasyan and Ray LaPierre. Thermal transport in twinning superlattice and mixed-phase gaas nanowires. *Nanoscale*, 14:6480–6487, 2022. doi: 10.1039/D2NR00720G.

[77] G.T. Noe, H.J. Haugan, G.J. Brown, G.D. Sanders, C.J. Stanton, and J. Kono. Coherent phonon dynamics in short-period inas/gasb superlattices. *Superlattices and Microstructures*, 52(6):1071–1077, 2012. ISSN 0749-6036. doi: https://doi.org/10.1016/j.spmi.2012.08.010.

[78] S. Gennari, P.P. Lottici, F. Ricco, G. Attolini, and C. Pelosi. Raman scattering in gaas/gap strained heterostructures grown by movpe. *Solid State Communications*, 91(8):599–602, 1994. ISSN 0038-1098. doi: https://doi.org/10.1016/0038-1098(94)90554-1.

[79] Marta De Luca, Claudia Fasolato, Marcel A. Verheijen, Yizhen Ren, Milo Y. Swinkels, Sebastian Kölling, Erik P. A. M. Bakkers, Riccardo Rurali, Xavier Cartoixà, and Ilaria Zardo. Phonon engineering in twinning superlattice nanowires. *Nano Letters*, 19(7):4702–4711, 2019. doi: 10.1021/acs.nanolett.9b01775.

[80] C. V. Raman and K. S. Krishnan. A new type of secondary radiation. *Nature*, 121(3048):501–502, 1928.

[81] Derek A. Long. *The Raman Effect: A Unified Treatment of the Theory of Raman Scattering by Molecules*. John Wiley & Sons, Ltd, 2002. ISBN 9780471490289. doi: 10.1002/0470845767.

[82] Roberto Merlin Willes H. Weber. *Raman Scattering in Materials Science*, volume 42 of *Springer Series in Materials Science*. Springer, 2000. doi: https://doi.org/10.1007/978-3-662-04221-2.

[83] Alexander A. Balandin. Thermal properties of graphene and nanostructured carbon materials. *Nature Materials*, 10(8):569–581, 2011. doi: https://doi.org/10.1038/nmat3064.

[84] Ahmed H. Zewail. Femtochemistry: Atomic-scale dynamics of the chemical bond. *The Journal of Physical Chemistry A*, 104(24):5660–5694, 2000. doi: 10.1021/jp001460h.

[85] M. Fleischmann, P.J. Hendra, and A.J. McQuillan. Raman spectra of pyridine adsorbed at a silver electrode. *Chemical Physics Letters*, 26

(2):163–166, 1974. ISSN 0009-2614. doi: https://doi.org/10.1016/0009-2614(74)85388-1.

[86] X. Gonze, J.-M. Beuken, R. Caracas, F. Detraux, M. Fuchs, G.-M. Rignanese, L. Sindic, M. Verstraete, G. Zerah, F. Jollet, M. Torrent, A. Roy, M. Mikami, Ph. Ghosez, J.-Y. Raty, and D.C. Allan. First-principles computation of material properties: the abinit software project. *Computational Materials Science*, 25(3):478–492, 2002. ISSN 0927-0256. doi: https://doi.org/10.1016/S0927-0256(02)00325-7.

[87] P. Hohenberg and W. Kohn. Inhomogeneous electron gas. *Phys. Rev.*, 136:B864–B871, Nov 1964. doi: 10.1103/PhysRev.136.B864.

[88] Stefano Baroni, Stefano de Gironcoli, Andrea Dal Corso, and Paolo Giannozzi. Phonons and related crystal properties from density-functional perturbation theory. *Rev. Mod. Phys.*, 73:515–562, Jul 2001. doi: 10.1103/RevModPhys.73.515.

[89] Michele Lazzeri, S. Piscanec, Francesco Mauri, A. C. Ferrari, and J. Robertson. Phonon linewidths and electron-phonon coupling in graphite and nanotubes. *Phys. Rev. B*, 73:155426, Apr 2006. doi: 10.1103/PhysRevB.73.155426.

[90] Hendrik J. Monkhorst and James D. Pack. Special points for brillouin-zone integrations. *Phys. Rev. B*, 13:5188–5192, Jun 1976. doi: 10.1103/PhysRevB.13.5188.

[91] Martin Hjort, Sebastian Lehmann, Johan Knutsson, Alexei A. Zakharov, Yaojun A. Du, Sung Sakong, Rainer Timm, Gustav Nylund, Edvin Lundgren, Peter Kratzer, Kimberly A. Dick, and Anders Mikkelsen. Electronic and structural differences between wurtzite and zinc blende inas nanowire surfaces: Experiment and theory. *ACS Nano*, 8(12): 12346–12355, 2014. doi: 10.1021/nn504795v.

[92] Omer Arif, Valentina Zannier, Francesca Rossi, Diego De Matteis, Katharina Kress, Marta De Luca, Ilaria Zardo, and Lucia Sorba. Gaas/gap superlattice nanowires: growth, vibrational and optical properties. *Nanoscale*, 15:1145–1153, 2023. doi: 10.1039/D2NR02350D.

[93] X. Gonze, B. Amadon, P.-M. Anglade, J.-M. Beuken, F. Bottin, P. Boulanger, F. Bruneval, D. Caliste, R. Caracas, M. Côté, T. Deutsch,

L. Genovese, Ph. Ghosez, M. Giantomassi, S. Goedecker, D.R. Hamann, P. Hermet, F. Jollet, G. Jomard, S. Leroux, M. Mancini, S. Mazevet, M.J.T. Oliveira, G. Onida, Y. Pouillon, T. Rangel, G.-M. Rignanese, D. Sangalli, R. Shaltaf, M. Torrent, M.J. Verstraete, G. Zerah, and J.W. Zwanziger. Abinit: First-principles approach to material and nanosystem properties. *Computer Physics Communications*, 180(12):2582–2615, 2009. ISSN 0010-4655. doi: https://doi.org/10.1016/j.cpc.2009.07.007. 40 YEARS OF CPC: A celebratory issue focused on quality software for high performance, grid and novel computing architectures.

[94] Erin L. Wood and Frederic Sansoz. Growth and properties of coherent twinning superlattice nanowires. *Nanoscale*, 4:5268–5276, 2012. doi: 10.1039/C2NR31277H.

[95] Th Grap, T Rieger, Ch Blömers, Th Schäpers, D Grützmacher, and M I Lepsa. Self-catalyzed vls grown inas nanowires with twinning superlattices. *Nanotechnology*, 24(33):335601, jul 2013. doi: 10.1088/0957-4484/24/33/335601.